Chapter 1

Introduction

The perovskite structure is quite simple, yet deviations from this structure can give rise to many interesting electronic properties. One particularly extreme example is $La_{1-x}Ca_xMnO_3$, which, depending on x and the temperature T, has para-, ferro- and antiferromagnetic phases, metal and insulator phases, a charge-ordered phase, as well as exhibiting giant magnetoresistance, activated behavior (perhaps due to polaron conductivity), Jahn-Teller distortions, and various structural transitions.

Two important classes of materials with such novel electronic properties that have been discovered in the last ten years are the high-temperature superconductors (HTSC)[1] and the so-called "colossal" magnetoresistors (CMR)[2]. Most of the materials that fall into these classes have a crystal structure that is related to the perovskite structure of calcium titanate, with important deviations. One example is the CMR material $La_{0.67}Ca_{0.33}MnO_3$, which is very nearly a perfect perovskite structure except for slight distortions[3]. These distortions appear to be manifestations of the Jahn-Teller distortions which occur in the parent compound $LaMnO_3$. Some scientists believe that the Jahn-Teller effect assists polaron localization above the Curie temperature[4], which accounts for the anomalously high resistivity and gives rise to the unusually large magnetoresistance.

The HTSC's have a layered structure, with each layer approximating a distorted perovskite. Each family of HTSC's share a similar structure, yet the small differences can have big effects on T_c. These materials are very sensitive to certain kinds of changes of the unit cell. For instance, T_c appears to peak for a given structure if the mean valence of the coppers in the CuO_2 planes is $\sim +2.3$. Therefore, the superconducting (SC) properties are very sensitive to vacancies (such as oxygen) or substitutions that change the number of valence charges, such as cobalt for copper. For example, in $YBa_2Cu_3O_{7-\delta}$ (YBCO) almost any trivalent (like yttrium) rare earth can be substituted for yttrium with minimal impact on the superconducting properties, yet a substitution of praseodymium decreases T_c smoothly to 55% Pr, where the samples are no longer superconducting. One explanation for this behavior is that some charge carriers are localized by hybridization of the praseodymium $4f$ and the oxygen $2p$ states[5]. Such a hybridization should cause a lattice distortion that looks locally like a Pr^{4+}-O bond, as in PrO_2. Measurements of such a distortion are presented in Chap. 7. Even proximity to other atoms can have a big effect, such as for the planar-copper, axial-oxygen pair distance; there is a strong correlation between this distance in a crystal and its T_c, with the materials with the longest distance having the highest T_c's (the Hg-based superconductors).

Such distortions should be static, and only affect the SC properties by redistributing the charge carriers within the unit cell. However, other distortions may not be static. There has been a long history of controversial measurements of lattice distortions at or near T_c, starting with x-ray diffraction measurements of crystal axes changing near T_c in YBCO[6] that took four years to verify by capacitive dilatometry measurements[7]. More compelling measurements that relate lattice properties to electronic properties include ion channeling measurements that show correlated displacements of the Cu(1), O(4) and Cu(2) atoms in $ErBa_2Cu_3O_{7-\delta}$[8], and the huge pressure dependence on T_c, especially in the Hg-based superconductors[9]. Despite these measurements, a determination of what local displacements drive the distortions has been elusive. Direct comparisons of XAFS and diffraction data revealed anomalously large broadening parameters of the Cu-O(1) (axial oxygen) bond in $HgBa_2CuO_4$ which can be interpreted as anti-correlated displacements, as in an optical phonon or a hopping polaron (Chap. 8). A similar analysis has recently shown a split Cu-O (planar) bond distribution; the size of the splitting decreases near T_c[10]. However, such distortions may be best described as static displacements, such as the ferroelectric-like distortions in $Tl_2Ba_2CuO_y$[11].

Another controversial measurement of lattice activity near T_c is the measurement of a split Cu(1)-O(4) (chain-copper, axial-oxygen) in YBCO that becomes smaller near T_c[12]. This measurement generated some excitement because some researchers thought it may be evidence for charge redistribution from the Cu-O chains to the planes, thereby giving the planes the "critical" number of holes to allow superconductivity. Others thought that the measurement may be evidence for a bipolaron charge-lattice coupling[13]. However, no other experiments were able to conclusively verify the measurement, probably because of variations between samples. Using high-quality and well-oriented single crystals and thin films, the data in Chap. 9 shows that the magnitude of any possible splitting cannot be directly related to T_c.

Although many measurements of lattice distortions and anomalous disorder have been made on the HTSC materials, a clear picture of how the lattice relates to SC has not yet emerged. A much clearer picture (and a good demonstration of the importance of understanding local structure) is provided by the CMR materials, and in particular, $La_{1-x}A_xMnO_3$, where A is one of certain divalent atoms. As mentioned above, these materials are thought to conduct by charge hopping. When a charge is localized, as occurs above the metal-insulator transition (in say, a covalent bond), the lattice must contract around that charge, forming a polaron. Because of the random (i.e. not periodic) nature of such distortions, a probe which relies on long-range order (such as diffraction) is not very sensitive to them. In particular, if the distortions are short-lived, then the distribution of bond lengths will appear Gaussian. Only a combination of a probe which measures *correlated* displacements between atom pairs and a probe which gives mean displacements for individual atomic sites can really discern a distortion caused by atoms moving together or apart. Chap. 10 presents XAFS data which, when considered in the light of diffraction studies, determines the size of the lattice-polaron.

In order to best describe the experimental studies on some of these perovskites, the remainder of this dissertation is split into two parts: "I. XAFS methodology" and "II. Experimental studies." Part II contains the measurements discussed above. In Part I, the XAFS technique is described. Beyond the basic equations, two fundamental aspects of the technique are described. First, a discussion of how correlations between atomic displacements can be measured by combining XAFS and diffraction data are presented. Measurements of correlated motions are very important for detecting dominant phonon modes or polaron distortions, and are, I believe, one of the most important advantages to employing a local probe in addition to (rather than just) diffraction. Several measurements of the correlation parameter are presented in later chapters, most importantly in Chap. 9, which gives correlation measurements for several atom pairs as a function of temperature in a film of YBCO.

Another fundamental aspect is the origin of certain structures which occur in the background absorption of certain species of absorbing atoms in certain crystal structures. In the basic XAFS analysis, a normalization function must be obtained which is proportional to the number of photoelectrons ejected from absorbing atoms in the crystal. Measurements of large features in the K-edges of Ba, Ce and Pr in various structures are presented. With the help of J. J. Rehr, we postulated that these features are similar to XAFS, except that the photoelectron actually scatters off that part of the potential in the interstices between the absorbing atom and its nearest neighbor. Identification of features as large as these may be very important to an XAFS analysis. For instance, if the background functions are *not* determined correctly, atom-pair distances may be skewed several hundredths of an angstrom.

Several of the studies reported here relied on the fluorescence signal as a measure of the absorption coefficient in thin film samples. Some aspects of fluorescence experiments are discussed. In particular, a discussion of how the dead time introduced by the energy-resolving peak-shaping filters used with a solid-state detector can affect an XAFS experiment, and examples of making good corrections. Also, the reduction of the XAFS amplitude by the self-absorption of the fluorescing photon by the sample is described, as well as how to correct for this reduction. Unlike previous treatments, the derivation of the correction factor includes the effect of the XAFS on the absorption coefficient, and thus on the correction.

Finally, an application of lock-in techniques to fluorescence XAFS data from a film of YBCO is presented. Chap. 6 describes a simple extension to the usual fluorescence-XAFS technique that allows the experimenter to take full advantage of the counting statistics in an XAFS experiment that looks for *changes* in the structure of some compound when some external variable is cycled. The YBCO film data is presented as an example. The state of the film is switched between normal and superconducting by applying a small heat pulse through a thin heater film on the back of the substrate. A standard XAFS experiment is performed during this switching, except that the fluorescence x-rays are collected with electronics which can store the counts in two separate memory locations, depending on the state of the film. The change in the structure should then be the difference of the two signals. This method has the ability to reduce all systematic noise sources below whatever counting noise exists by cycling the state faster and thus taking advantage of the $1/f$-character of non-counting noise. The experiment in this example was limited to ~ 2 Hz, but the noise level was count-rate limited up to 1:10^4. Although no significant structural changes were observed, very strict limits were placed on the possible magnitude of any possible changes. This experiment holds the promise of observing with precision any structural change that can by turned on and off by varying some external parameter at a reasonable rate (> 0.1 Hz).

Part I

XAFS Methodology

Chapter 2

Experimental introduction

The x-ray-absorption fine-structure technique is now well established, so I will not give a detailed theory of the effect here. A good review of the theory is Ref. [14]. The analysis techniques are summarized in Ref. [15, 16, 17, 18]. The following explanation will suffice for the rest of the information in this document.

The primary features in the absorption of x-rays by atoms as a function of energy are sudden increases of the absorption coefficient that occur when the x-ray energy is sufficient to eject a photoelectron (p.e.) from the absorbing atom. When the absorbing atom has neighboring atoms, such as in a solid or a liquid or even a diatomic gas, there are oscillations above the absorption edge. These oscillations are primarily due to an interference of the outgoing photoelectron and the part of its wave function which is backscattered by the neighboring atom. This interference is immediately apparent from Fermi's Golden Rule:

$$\mu \sim | < f|\hat{\epsilon} \cdot \vec{r}|i > |^2 \tag{2.1}$$

where $|i>$ and $<f|$ are the initial and final states of system, which includes the superposition of the outgoing and the backscattered photoelectron. Because the degree of interference

between $|i>$ and $<f|$ is proportional to their amplitudes, the oscillation amplitude of μ is proportional to several factors unique to each experiment. First of all, the amplitude must be proportional to the number of photoelectrons available for backscattering. If we consider that the oscillations decrease rapidly with the incident photon energy (see discussion of Debye-Waller factor below), then we can assume that only the photoelectrons arising from the nearest absorption edge contribute. To remove the effect of all other photoelectrons one could consider tabulated data for the elements and calculate the contribution from the other atoms in the absorbing material, or simply subtract a function which makes the absorption data follow the tables for the absorbing atom. Once this has been accomplished one can define a function which is equal to the amplitude of the XAFS oscillations by exploiting the fact that the number of photoelectrons available for backscattering is proportional to the part of the absorption coefficient that does not include the backscattering effects. We can define this latter absorption as $\mu_0(E)$ and then write:

$$\chi(E) = \frac{\mu(E) - \mu_0(E)}{\mu_0(E)} \tag{2.2}$$

where $\mu(E)$ is the total absorption due to the absorbing atom. Experimentally, $\mu_0(E)$ is usually obtained by fitting a smooth function through the oscillatory $\mu(E)$. This method is generally accurate, although other absorption processes can affect the shape of $\mu(E)$ (Chap. 4).

Now that we have removed the number of p.e.'s from the oscillatory amplitude (which, by the way, includes the number of irradiated atoms), we can consider other variables which the material introduces into $\chi(E)$. $\chi(E)$ must be proportional to the number of neighboring atoms N, the probability of backscattering off such atoms F(E), and include the effective decay of the p.e.'s via scattering [$\exp(-\lambda/r)$, where λ is the mean-free-path]. Rather than use E as a variable, the magnitude of the p.e. wave vector ($k = \left[\frac{2m}{\hbar^2}(E - E_0)\right]^{1/2}$, where E_0 is the p.e. threshold energy) is generally used. Also, since the interference term goes like $\sin(2kR)$, where k is the p.e. wave vector and R is the distance to the backscattering atom, a term to account for the distribution of R from disorder (thermal or static) is necessary. Lastly, one must consider that the p.e. wave function is spherical ($\propto 1/kR^2$) and that other absorption processes, such as multiple electron excitations can reduce the overall amplitude of χ. One may then write a simplified version of the "XAFS equation":

$$\chi(k) = S_0^2 \sum_{i=1}^{\infty} N_i F_i(k) \mathrm{Im} \int_0^{\infty} \exp[-r/\lambda(k)] g_i(r) \frac{e^{i[2kr+\phi_i(k)+2\phi_0(k)]}}{kr^2} \mathrm{d}r \qquad (2.3)$$

where S_0^2 is an amplitude reduction factor which accounts for p.e. losses to other (non-backscattering) mechanisms, and $\phi_i(k)$ and $\phi_0(k)$ account for the phase shift of the p.e. due to the backscattering and absorbing atom, respectively. $g_i(r)$ is the pair distribution function for scattering path i, and is usually taken to be Gaussian (harmonic):

$$g_i(r, R_i) = \frac{1}{\sqrt{2\pi}\sigma_i} e^{-\frac{(r-R_i)^2}{2\sigma_i^2}},$$

where σ_i is known as the "Debye-Waller factor." (Sometimes σ is called the "correlated-Debye-Waller factor" for reasons explained in Chap. 3.) A glance at Eq. 2.3 reveals that it is essentially a Fourier transform of a peaked function ($g_i(r)$). In other words, a Fourier transform of Eq. 2.3 will be a function with peaks that correspond directly to the number and scattering distance of the individual scattering paths i. We often refer to this transform as being in "r-space" and Eq. 2.3 as being in "k-space."

In practice, we write the r-space XAFS equation as

$$\tilde{\chi}(r) = \sum_i S_{0,i}^2 N_i \int_0^{\infty} g_i(r', R_i) F_{\mathrm{eff},i}(r, r') \mathrm{d}r', \qquad (2.4)$$

where $F_{\text{eff},i}(r,r')$ is the transform for a normalized (single) scattering path for an atom pair at a distance r'. This function includes all the λ, phase shift, and $1/kr^2$ dependencies. The integral in this equation is basically a convolution of the pair-distribution function and $F_{\text{eff},i}(r,r')$.

To extract structural information from an experimental measurement of $\chi(k)$, we fit Eq. 2.4 to the data, allowing the overall amplitude to vary, as well as R_i, σ_i and E_0. Usually, we use a theoretical calculation from the FEFF code[19, 20] to get $F_{\text{eff},i}(r,R_i)$. These calculations are not perfect. In fact, they were not considered applicable for precise measurements until the early part of this decade. The improved codes have now been tested on a wide variety of standard compounds, and excellent fits are obtainable[17, 21]. However, to account for small errors in the FEFF calculations, we sometimes have to allow some individual paths to have their own S_0^2, and very often assign each backscattering-atomic species its own E_0.

2.1 Experimental setup

The usual experimental apparatus for measuring the transmission of x-rays through a cooled sample is very simple. (A somewhat more complete description and diagram is in Chap. 5.) The x-rays are provided by a synchrotron light source, such as the one at the Stanford Synchrotron Radiation Laboratory. Once the broad-band radiation passes through a double-crystal monochromator, a typical flux is 10^{10} counts per second (cps) into a slit of 1×10 mm, depending on the electron beam current and the particular geometry of the beam line. For samples where the absorbing atom produces an edge step of unity, this flux means the fractional statistical noise level is $\sim 10^{-5}$, below the systematic errors introduced by beam motion, sample non-uniformity, FEFF errors, etc. For cases where the absorbing atom is only in a 10-20% abundance or less, fluorescence detection often produces a cleaner signal. Fluorescence detection is discussed in Chap. 5.

Powder samples are ground, put through a 30 μm sieve and brushed onto Scotch tape. The tape preferentially holds onto the smaller particles. In one recent experiment, we looked at grains of $LaMnO_3$ under an optical microscope and estimated the mean particle size to be 5-10 μm. Such small grains allow us to ignore the so-called "thickness effect" for energies above 5 keV. (The thickness effect becomes important in materials where the mean grain size is on the order of or larger than one absorption length[22].) All samples are usually placed in a LHe flow-cryostat which allows temperatures between 15-320 K. Ion chambers are filled with N_2 or a noble gas, with increasing Z for harder x-rays. Sometimes a second sample is placed in between the I_1 and I_2 counters as an energy reference. For a more complete description of the experimental setup, please see Ref. [18].

Chapter 3

Correlations between the positions of neighboring atoms

The XAFS technique is very useful for many reasons. It is atomic-species specific, so one can look at the PDF from the viewpoint of any type of atom in the crystal. This feature is especially useful when trying to understand the disorder around impurities in a sample. XAFS is a local probe; diffraction relies on the coherent scattering of light from many lattice planes that must be periodic in order to give a measurement, whereas XAFS has no requirement of periodicity. This feature makes it especially useful in the study of glasses and other disordered materials. Another feature that has been under-appreciated until recently is that the XAFS Debye-Waller factor contains complimentary information to the diffraction Debye-Waller factor. The difference is that the XAFS Debye-Waller factor measures the average deviation in the PDF for a *pair* of atoms, while diffraction measures the average deviation of individual crystal sites.

In diffraction, the width parameter U can be defined as

$$U_i =< (\vec{P}_i - < \vec{P}_i >)^2 >$$

where $\vec{P}_i$ are the position vectors of the individual atomic sites and the average is over each site and the vector components. U_i may be broken into vector components if the disorder is not isotropic.

In XAFS, we measure the broadening of bonds:

$$\sigma_{ij}^2 =< (r_{ij} - < r_{ij} >)^2 >$$

where r_{ij} are the radial pair distances between atoms i and j. This equation may be rewritten in terms of the position vectors:

$$\sigma_{ij}^2 =< (|\vec{P}_j - \vec{P}_i| - | < \vec{P}_j > - < \vec{P}_i > |)^2 > .$$

To first order, we can assume that $\vec{P}_j - \vec{P}_i$ lie along the average direction of the pair. Then, defining $\Delta P_j = P_j - < P_j >$, we have

$$\begin{aligned}
\sigma_{ij}^2 &= < (\Delta P_i - \Delta P_j)^2 > \\
&= < \Delta P_i^2 + \Delta P_j^2 - 2\Delta P_i \Delta P_j > \\
&= < \Delta P_i^2 > + < \Delta P_j^2 > -2 < \Delta P_i \Delta P_j >
\end{aligned}$$

The last term depends on how the position vector components ΔP_i and ΔP_j are correlated. If they are completely uncorrelated, this term will average out to zero. If they are completely correlated, then $< \Delta P_j \Delta P_i >=< \Delta P_j >< \Delta P_i >$. If they are *anti*-correlated, or negatively correlated, then $< \Delta P_j \Delta P_i >= - < \Delta P_j >< \Delta P_i >$. With this correlation in mind, we can write σ^2 finally in terms of the diffraction Debye-Waller factor:

$$\sigma_{ij}^2 = U_i + U_j - 2\sqrt{U_i U_j}\phi$$

where $\phi \equiv \frac{<\Delta P_i \Delta P_j>}{\sqrt{U_i U_j}}$, and therefore,

$$\phi = \frac{U_i + U_j - \sigma_{ij}^2}{2\sqrt{U_i U_j}}. \tag{3.1}$$

Notice that ϕ is in terms of measurable quantities.

The concept of ϕ is in no way new. The early work in XAFS was well aware that XAFS and diffraction measure different width parameters and how they are different. The reason that most experimenters haven't taken a close look at a measurement of ϕ in their systems is that until the last 4 years or so, an *absolute* measurement of σ_{ij}^2 was not considered to be possible; high-quality fits of XAFS data relied on the measured XAFS signal from well characterized compounds (standards) whose width parameters were not known. In other words, XAFS experimenters had no reliable measure of the "zero width" signal with which to measure the σ_{ij}^2. The FEFF codes by Rehr and co-workers is now developed enough[19, 20] and characterized enough[17, 21], that we can now say that measurements of σ_{ij}^2 are good to roughly 10%, and even better for near-neighbor atom pairs.

3.1 random distortions and disorder

To illustrate the usefulness of a measurement of ϕ, consider Fig. 3.1. The top panel shows snapshots-in-time of a long wave length acoustical phonon, where, to a local approximation, all the atoms are displaced the same distance and in the same direction from their mean positions. If diffraction were to measure the mean displacement over time of the individual atomic sites, it would measure $\sqrt{U} = \Delta$. On the other hand, if XAFS were to measure the separation between the central atom and its neighbors, it would always get the same result (r_0) for each time, and thus would measure a zero width for the distribution function. In this case, we say the atom-pair displacements are completely correlated, and $\phi = 1$. The bottom panel shows a similar picture for an optical phonon mode. Here, diffraction would still measure $\sqrt{U} = \Delta$, but XAFS would give $\sigma = 2\Delta$. This situation gives $\phi = -1$.

Since XAFS is a very fast probe ($\sim 10^{-15}$s) on the time scale for atomic motions ($\sim 10^{-13}$s), the above example could have been for static displacements in the crystal. In such a case, the acoustical phonon picture could be replaced by different domains in a crystal that have phase-separated, and the optical phonon picture could be replaced by a charge-ordered state, such as occurs in $La_{0.35}Ca_{0.65}MnO_3$.

3.2 non-Gaussian PDF's

If we only encounter well characterized materials with Gaussian pair-distribution functions, ϕ must be between 1 and -1. However, if some static distortion occurs which is below the resolution of both diffraction and XAFS, and the pair-distributions are still modeled as Gaussian, the calculated ϕ can be less than -1 if diffraction does not provide the proper U parameter. Diffraction can "fail" if a distortion exists that has no long-range order in certain cases. For instance, in $Ga_{1-x}In_xAs$, diffraction indicates a Ga-As bond length that changes linearly with x from the same bond length as in GaAs to the In-As bond length in InAs. However, XAFS has shown that the Ga-As bond length stays very close to the same length as in GaAs for all x[23]. That is, diffraction inadvertently measures an ordered atom pair at a distance that does not occur in the crystal. If neither XAFS or diffraction resolves such a distortion, a measurement of $\phi < -1$ could be evidence for its presence.

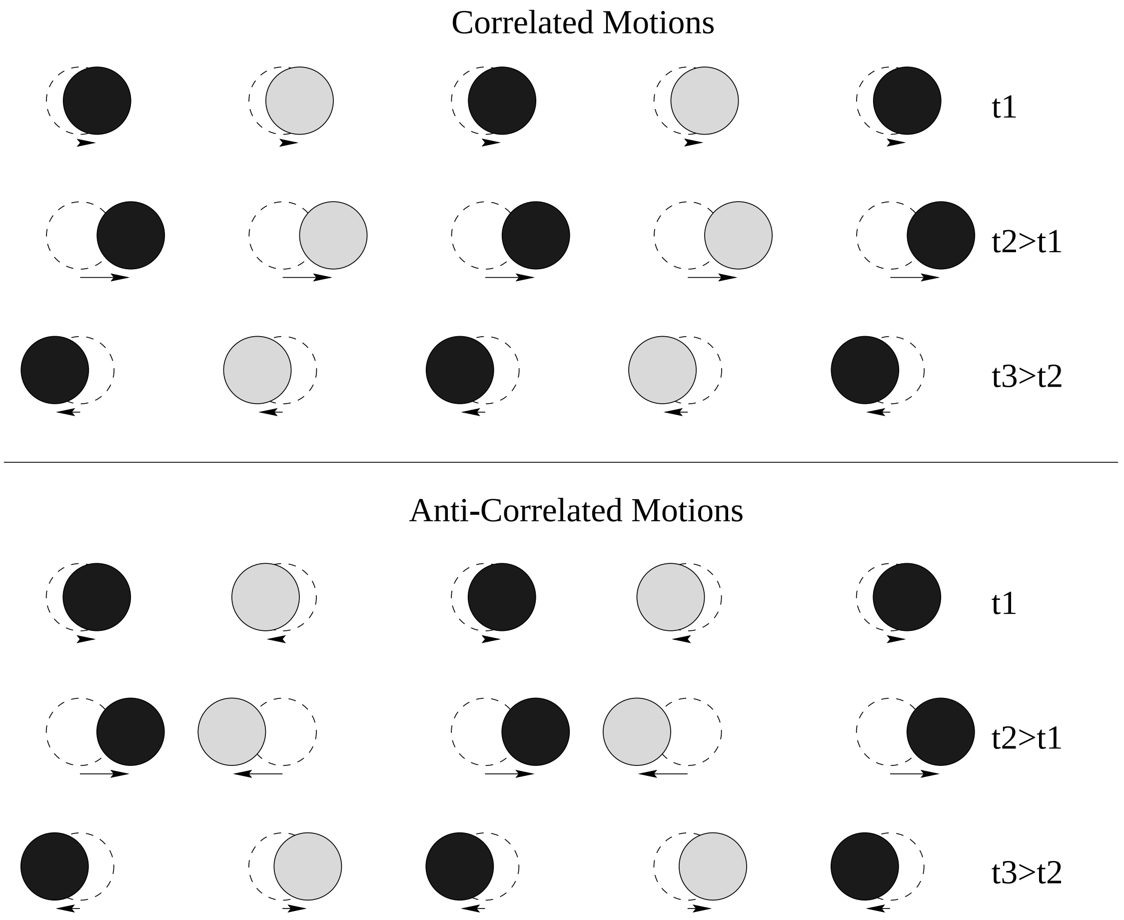

Figure 3.1: Snapshots in time of two vibrational modes that illustrate correlated broadening measurements. The top panel shows a long wavelength acoustical phonon at three different times. Notice that while the average displacements of the individual atoms may be significant, the bond length does not change with time. The bottom panel shows a short wavelength optical phonon. Here, the bond length changes twice as much as the average site positions.

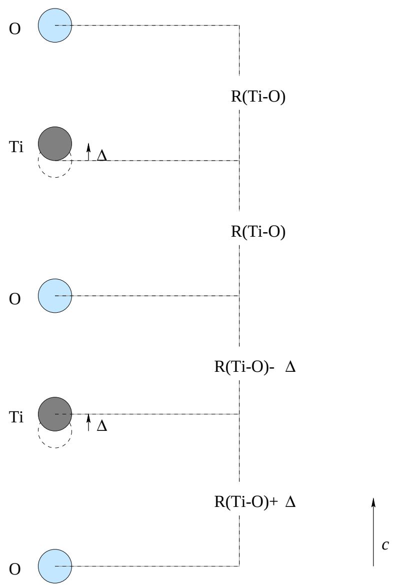

Figure 3.2: Ti-O chain with ferroelectric distortions, as along the c-axis in $BaTiO_3$. Dotted circles show position of atoms according to diffraction above the Curie temperature.

As an example, consider the ferroelectric shown in Fig. 3.2. Above the Curie temperature, $BaTiO_3$ displays a cubic diffraction pattern with a perovskite unit cell (the bariums on the corners, the titanium in the body-center and the oxygens at the face-centers). Below T_c, the crystal undergoes a tetragonal distortion whereby the titanium and barium atoms move approximately 0.1 Å along the c-axis and the oxygens above and below the titanium move a smaller amount in the opposite direction. Recent XAFS measurements on $PbTiO_3$ have shown that even above T_c, this distortion still exists, even though diffraction indicates a well ordered cubic crystal[24]. This apparently contradictory situation occurs because the tetragonal distortion has no long-range order above T_c. In a diffraction experiment, the atoms occur at the perovskite sites, with apparently normal thermal parameters. If an XAFS experimenter could not resolve the distortion, (s)he may fit, say, the two Ti-O peaks along the c-axis to one peak. Let's say the thermal disorder is isotropic, and for the Ti site, we will denote it as $\sigma_{\mathrm{T}i}$, and similarly for oxygen. Let's also write the distortion along the c-axis as $\Delta_{\mathrm{T}i}$. Assuming no correlation between the thermally-generated displacements, the XAFS width would be

$$\sigma^2_{\mathrm{T}i-O} = (\Delta_{\mathrm{T}i} + \Delta_{\mathrm{O}})^2 + \sigma^2_{\mathrm{T}i} + \sigma^2_{\mathrm{O}}. \tag{3.2}$$

If the U parameters from diffraction measure mainly the thermal displacements, then we get

$$\phi = -\frac{(\Delta_{\mathrm{T}i} + \Delta_{\mathrm{O}})^2}{2\sigma_{\mathrm{T}i}\sigma_{\mathrm{O}}}. \tag{3.3}$$

If we use some typical numbers, such as $\Delta_{\mathrm{T}i} = 0.1$Å, $\Delta_{\mathrm{O}} = 0.02$Å, $\sigma_{\mathrm{T}i} = 0.04$Å, and $\sigma_{\mathrm{O}} = 0.05$Å, then we get $\phi = -3.6$.

Other anomalous measurements of ϕ could occur simply because all these distributions are fit to harmonic functions. In these case, measurements of the "harmonic" mean-square displacements, could be either too large or too small for either XAFS or diffraction, allowing negative measurements of ϕ and even measurements slightly greater than one.

3.3 polarons

As mentioned in Sec. 3.1, the situation in Fig. 3.1 could be either for static or dynamic disorder. One very important situation where non-Debye-like behavior can mimic the disorder in Fig. 3.1 occurs in the case of a hopping small polaron. A polaron (static or hopping) is the combination of a charge (hole or electron) and the lattice distortion that occurs around it. An extreme (and mundane) case would be a charge ordered state. For instance, if you have a chain of manganese and oxygen atoms, and every other Mn-O pair has an extra hole, that is you have a chain of ...-Mn^{+4}-O^{-2}-Mn^{+3}-O^{-2}-..., the Mn^{+4}-O^{-2} atom pairs will be separated by less distance than the Mn^{+3}-O^{-2} pairs, similarly to a time-slice of the optical phonon in Fig. 3.1. Such a situation would be easily detectable by diffraction experiments. However, if the polaron *hops*, as is thought to occur in many insulators and in $La_{0.67}Ca_{0.33}MnO_3$ (Chap. 10), the situation would look very much like an optical phonon as a function of time (Fig. 3.3), and as discussed in Sec. 3.1, only a combination of a long-range probe (i.e. diffraction) and a local probe (i.e. XAFS) can detect the characteristic negative correlations in the atomic displacements.

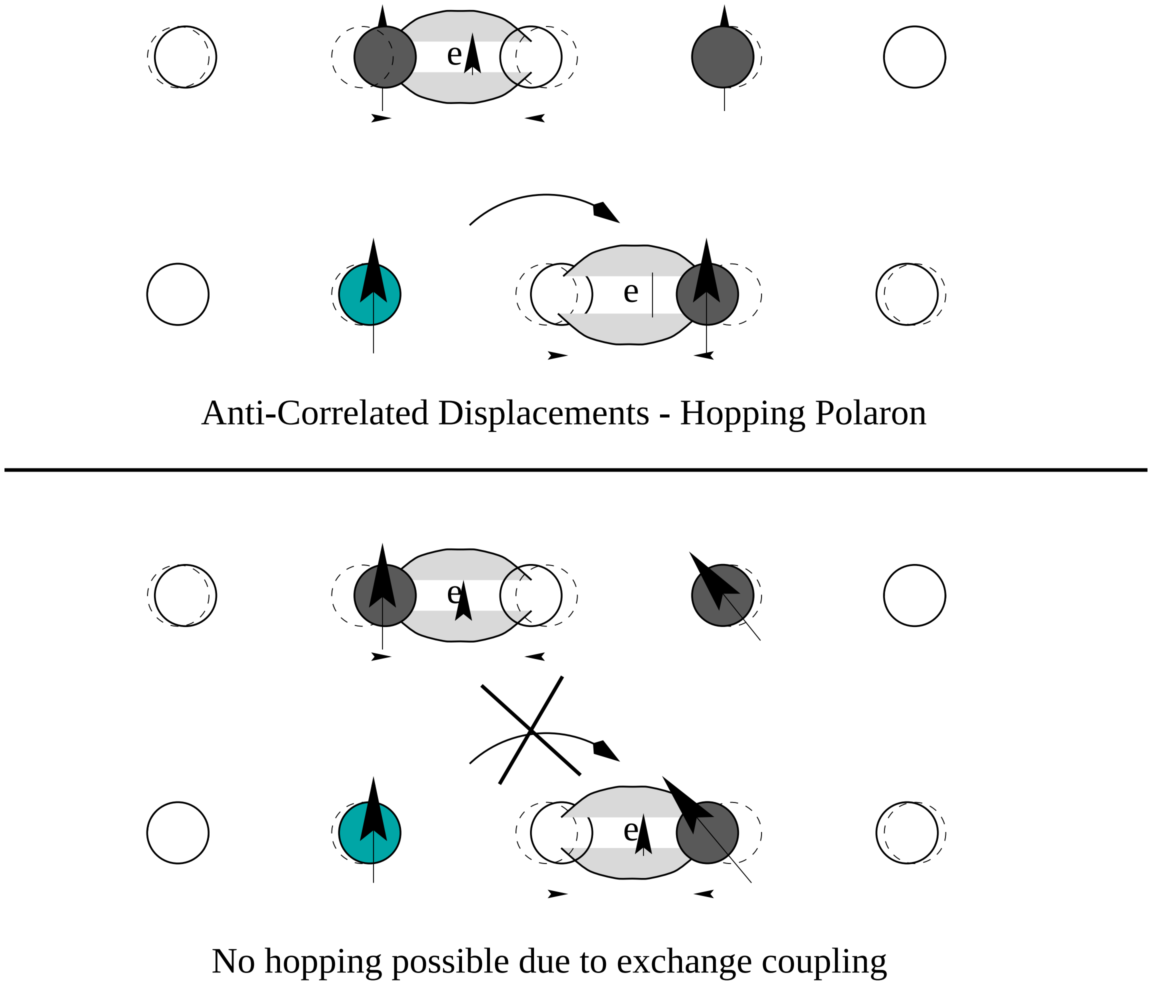

Figure 3.3: Schematic picture of a hopping charge and the lattice distortion that can accompany it, i.e. a small polaron. A large polaron occurs when the charge is delocalized over some area, and the lattice distortion is thus spread out over a larger range in the crystal. This figure represents the particular case of "double exchange." The large arrows represent the magnetic moment of the t_{2g} electrons on the Mn atoms (dark circles). The smaller arrows are the spin of the e_g electron that may be present under certain doping conditions. Double exchange describes the ability of the e_g electron to hop to a neighboring Mn if its t_{2g} electrons' moments and the hopping e_g electron's moments are aligned. Since there is a strong Hund-coupling of these states within a given Mn atom, double-exchange hopping occurs below a Curie temperature. See Chap. 10.

Chapter 4

X-ray-absorption fine-structure in embedded atoms

 The archival version of this work was published in J. J. Rehr, C. H. Booth, F. Bridges and S. I. Zabinsky, Phys. Rev. B, **49**, *R12347 (1994). Regarding this dissertation, C. H. Booth was soley responsible for Sec. 4.2 and Sec. 4.4 and J. J. Rehr was solely responsible for Sec. 4.3.*

4.1 Introduction

The main features of X-ray absorption spectra μ(E) are due to one-electron transitions from deep core levels. In molecules and solids, oscillatory fine structure exists in $\mu(E)$

due to scattering of the photoelectron by neighboring atoms. The well known technique of x-ray-absorption fine structure (XAFS), which includes both extended-XAFS (EXAFS) and x-ray-absorption near-edge structure (XANES), is based on the analysis of this fine structure. In XAFS the oscillatory part χ is defined relative to an assumed smooth "atomic background" absorption $\mu_0(E)$, i.e., $\chi = (\mu - \mu_0)/\mu_0$. A complication is that $\mu_0(E)$ is not necessarily smooth. For example, the background may exhibit such well known structures as white lines, resonances and jumps due to multi-electron transitions, even well above threshold. Less well known, however, is the possible fine structure in $\mu_0(E)$ itself, in molecules and condensed systems, as discussed by Holland *et al*[25]. The purpose of this study is to show that this atomic x-ray-absorption fine structure (AXAFS) can produce large oscillations, has an XAFS like interpretation, and can alter XAFS analysis. In view of recent advances in XAFS theory and analysis techniques[26, 27, 28], in which the background plays a crucial role, this structure is now particularly important.

This extra fine structure originates from resonant scattering "in the periphery of the absorbing atom"[25]. The effect is like an internal Ramsauer-Townsend (RT) resonance where the incident electron is a spherical wave created at the center of the atom, rather than a wave scattered by an atom. As the photoelectron electron approaches a potential barrier - in this case the edge of an embedded atom potential - the reflection coefficient oscillates with energy, with a pronounced increase just above threshold, followed by a dip and subsequent oscillations that conserve integrated oscillator strength. We find that AXAFS can be the dominant background fine structure and has features in the same energy range as multi-electron transitions, complicating detection of the latter. Using a new background subtraction technique[27], experimental backgrounds for Ba, Ce and Pr K-edges are obtained which exhibit AXAFS as large as 60% of the XAFS amplitude. Theoretical calculations[26] based on an *ab initio* XAFS/XANES code FEFF 5X confirm these observations. To our knowledge, the only previous attempt[25] to identify AXAFS was only partly successful, and the work did not derive its oscillatory character. Also, notable discrepancies between theory and experiment were found at low energies, and no attempt was made to observe AXAFS in crystalline solids. We believe, however, that evidence for AXAFS exists in many previous studies, although not heretofore identified as such. In particular we suggest that AXAFS is largely responsible for the spurious peak at about half the first neighbor distance often observed in XAFS Fourier transforms[27, 29].

4.2 Experimental Backgrounds

XAFS analysis differs from LEED and other spectroscopies where the full theoretical spectrum is compared with experiment. Although the XAFS spectrum $\chi(E)$ can now be calculated remarkably well ($< 1\%$ errors for many systems), some features in background absorption spectra $\mu_0(E)$ in solids are not yet as well described by theory. Deviations typically about 5% have been found in the few cases where detailed comparisons have been made, and systematic errors in absorption measurements are a further complication. Consequently, theoretical background functions are not usually used to fit the full absorption spectra $\mu(E)$.

Until recently, estimating the background by a smooth spline through the XAFS has been the standard approach in detailed XAFS analyses. However, a number of improved background subtraction techniques have recently been developed[27, 28]. The approach adopted here[27] is based on an iterative procedure, which makes use of the high quality of present theoretical XAFS functions. After removing the pre-edge absorption, a smooth spline function is fit to the absorption data $\mu(E)$ (Fig. 4.1), which simulates to lowest order the free atomic absorption $\mu_0(E)$ without XAFS or other features present. Then a trial XAFS function $\chi(E) = [\mu(E)/\mu_0(E)] - 1$ is obtained. A Fourier transform of χ with respect to wave number k defined with respect to threshold energy E_0, yields peaks in r-space corresponding to the distribution of neighbors to the absorbing atom. Initially, the transforms often have a spurious, r-space peak near 1 Å that is inconsistent with their known structures. Next an approximate fit of the first few peaks of the r-space transform is made using theoretical XAFS standards[30, 31]. This fit is transferred back to energy space and subtracted from the experimental data to remove most of the low frequency XAFS oscillations. A high order spline is used to smooth the remaining data (Fig. 4.1). The positions of the knots in this spline are varied to follow the larger features in the residue. This spline function then becomes a new $\mu_0(E)$ and a new XAFS function is extracted. The process is iterated to convergence, typically in several iterations. With this procedure the background $\mu_0(E)$ contains all the atomic fine structure and the spurious r-space peak near 1 Å is eliminated.

This procedure was tested on a theoretical absorption spectrum from FEFF 5X for a model of $PrBa_2Cu_3O_7$ (PBCO) which included many XAFS shells and a background with the above RT-like resonance. PBCO was chosen because the contribution from higher shells is significant. This check therefore tests both the fit to the XAFS and to the background. The extracted background fits the simulated background well (Fig. 4.1).

This procedure was then applied to Ba, Ce, and Pr K-edge data of BaO, CeO_2, and PBCO. The data were collected at $T \simeq 80$ K, at the Stanford Synchrotron Radiation

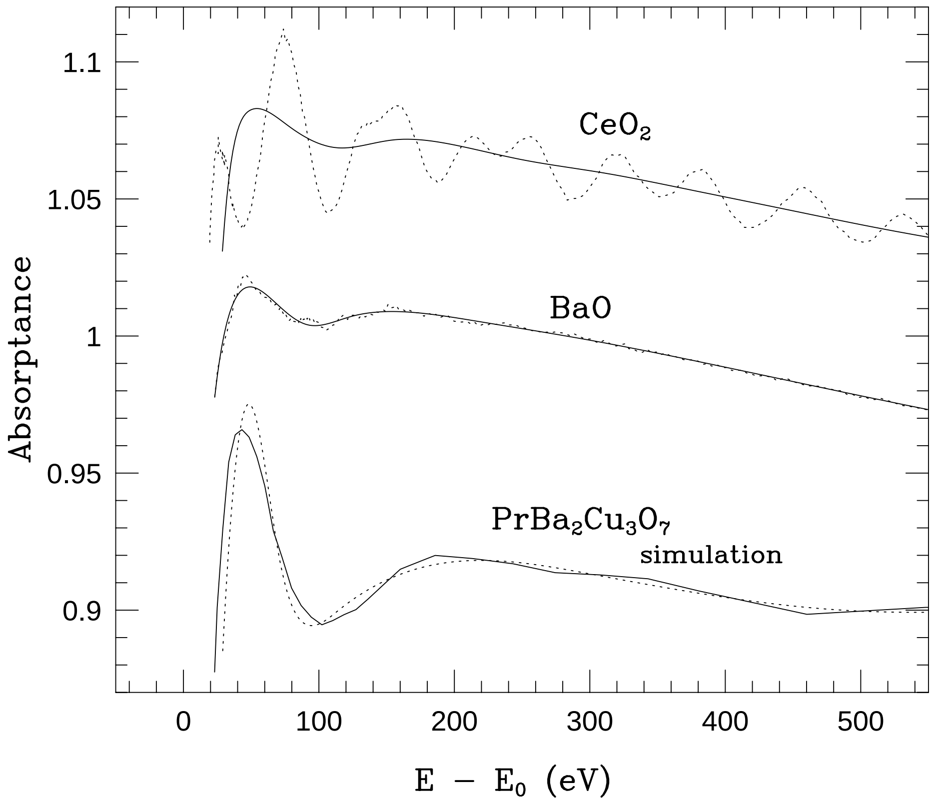

Figure 4.1: Top curves: Ce K-edge absorption $\mu(E)$ (dotted) and $\mu_0(E)$ (solid) from CeO_2 vs. energy E above the Ce K-edge (40441 eV). All spectra in this paper have their step height normalized to unity, and shifted as displayed. The oscillatory structure above the edge (dotted) is the XAFS. The solid curve is the experimentally obtained "atomic background" absorption $\mu_0(E)$ (see text). Note the sharp dip in this background at $\simeq$ 115 eV. Middle curves: residue function and fit for Ba K-edge data from BaO. The residue functions are the difference between the data and the fit in E-space, *i.e.*, $\mu_{res}(E) = \mu(E)/(\chi_{fit}(E) + 1)$. Bottom curves: simulated background (solid) and extracted background (dotted) as a test of our extraction method.

Laboratory (SSRL) using (400) monochromator crystals on beam line 10-2. Details are given in a separate paper[32]. The extracted backgrounds of all these high energy K-edges (Fig. 4.2) are similar in shape and energy scale, exhibiting the near-edge peak and dip structure consistent with that expected for a RT resonance. The magnitude of this structure is comparable to EXAFS amplitudes and is a factor of four larger than the step-like structures observed above the edge for the rare gas Kr or for the Rb and Br K-edge data for RbBr.

4.3 AXAFS Theory

We now briefly discuss the theory of AXAFS and show that it has an interpretation analogous to the curved-wave theory of XAFS[33]. "Embedded" atoms in solids may be defined in terms of their respective scattering potentials. The final state potential v_0 at the absorption site consists of a bare atomic potential v_a, plus extra-atomic contributions v_e from the tails of the electron distributions of neighboring atoms. In the muffin-tin approximation,

$$\begin{aligned} v_0(r) &= v_a(r) + v_e(r), \qquad && (r < R_{mt}), \\ &= v_{mt}, && (r \geq R_{mt}), \end{aligned} \tag{4.1}$$

where R_{mt} is the muffin-tin radius. For simplicity we consider a one-electron calculation of photoabsorption by an embedded atom using the Fermi Golden rule and the dipole approximation, i.e.,

$$\mu_0(E) = 4\pi^2\alpha\omega \sum_f |\langle c|\hat{\epsilon}\cdot\vec{r}|f\rangle|^2 \delta(E - E_f), \tag{4.2}$$

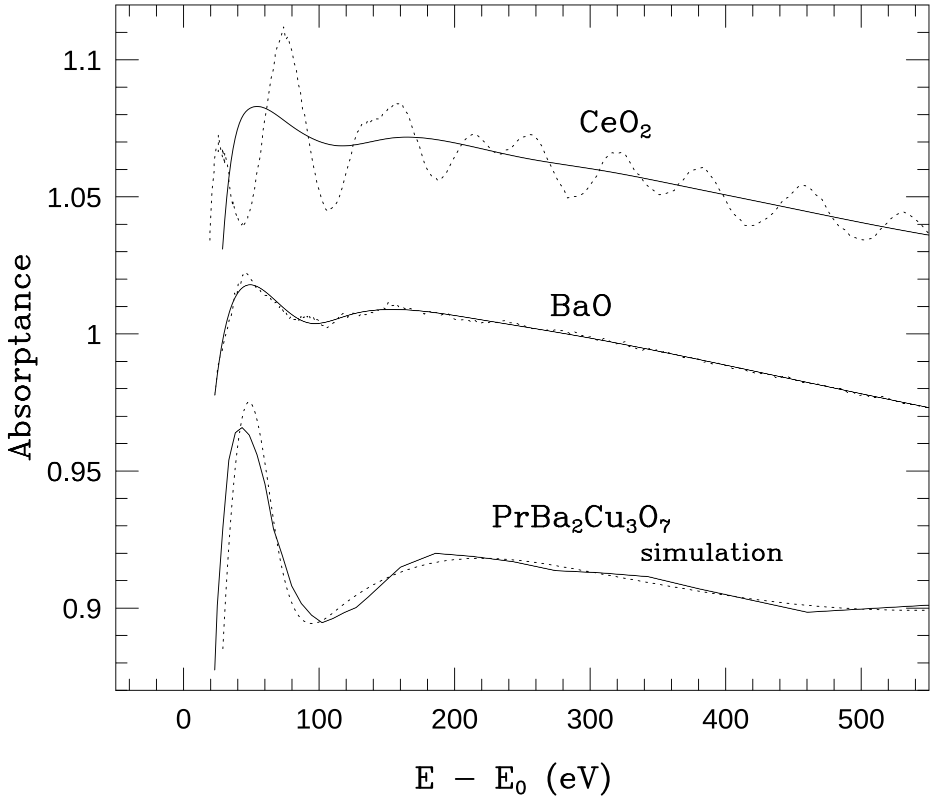

Figure 4.2: Experimental (dotted lines) and theoretical (solid lines) background absorptions, $\mu_0(E)$, for the Ba, Ce, and Pr K-edges of BaO, CeO_2, and PBCO. ΔE is the energy above threshold, *i.e.,* 37,444, 40,441, and 41,991 eV for the Ba, Ce and Pr edges, respectively. Both the experimental and the theoretical backgrounds have been adjusted to fit the Victoreen formula with a 4th-order polynomial. The calculations are currently limited by discontinuities at R_{mt} which can effect the AXAFS amplitude. The BaO calculation has an additional threshold energy shift of +20 eV. Arrows indicate the positions of Z+1 excitation thresholds.

where $\alpha \simeq 1/137$ is the fine structure constant, ω is the X-ray energy (we use Hartree atomic units $e = m = \hbar = 1$), $E = \omega - E_c$ is the photoelectron energy, $\hat{\epsilon}$ is the x-ray polarization vector, and the final states $|f\rangle = (1/r)R_0(r)Y_{lm}(\hat{r})$ are calculated at energy $E_f = (1/2)k^2$ in the embedded atom potential v_0. The normalized radial wave functions $R_0(r)$ are obtained by matching the regular solution of the radial l-wave Schrödinger equation to the asymptotic form $R_0(r) = kr[j_l(kr)\cos\delta_l - n_l(kr)\sin\delta_l]$, $(r \geq R_{mt})$, where j_l and n_l are spherical Bessel functions, δ_l is the $l-$th partial wave's phase shift, and l is fixed by dipole selection rules. This matching procedure is equivalent to a calculation of the Jost function $F_l(E)$ which guarantees final state normalization, as discussed by Holland *et al.*[25] and by Newton[34]. In particular Holland *et al.* show that the atomic cross-section can be written as $\tilde{\mu}_0/|F_l|^2$, where $\tilde{\mu}_0$ is a reduced matrix element which varies smoothly with energy. All of the calculations of AXAFS reported here are based on an analogous matching procedure for the relativistic spinor wavefunctions used in FEFF, without any of the simplifying approximations of the following discussion. Additional details will be given elsewhere[20].

The formal relations[34] satisfied by the Jost function are very general and do not explicitly show the oscillatory behavior of AXAFS. Thus to illustrate its nature we present a highly simplified model based on first order perturbation theory with respect to the free atom potential. We will assume that the free atomic background has negligible oscillatory structure; sample calculations with large muffin-tin radii support this assumption. Using the spectral representation of the embedded atom Green's function, the final state sum in Eq. (4.2) can be expressed as $\Sigma_f |f\rangle\delta(E - E_f)\langle f| = (-1/\pi)\,\mathrm{Im}\,G_0$ where $G_0 = (E - H_0 + i0^+)^{-1}$ is the embedded atom Green's function (operator) and H_0 the embedded atom Hamiltonian. To first order in the perturbation $\delta v = v_0(r) - v_a(r)$, G_0 is given by $G_0 \simeq G_a + G_a \delta v G_a$, where G_a is the free atomic Green's function. For deep core absorption, the core states are highly localized so we need only evaluate G_0 in position space for very small arguments r and r', where δv is negligible. The radial part of G_a[34], is given by $G_a(r,r') = (-1/k)R_a(r_<)R_a^+(r_>)$, where $r_{>(<)}$ is the greater(lesser) of r and r', and $R_a^+ = S_a + iR_a$ is the outgoing part of the radial Schrödinger equation. Combining these ingredients, one finds that $\mu(E)$ can be factored as in conventional XAFS theory[35], i.e., $\mu_0 = \mu_a(1+\chi_e)$, where μ_a is given by Eq. (4.2) calculated with free atomic states $|f_a\rangle$ and the AXAFS χ_e is

$$\chi_e \simeq -\mathrm{Im}\,\frac{1}{k}\int_0^\infty dr[R_a^+(kr)]^2\delta v(r). \tag{4.3}$$

An analogy to the curved-wave XAFS formula[33] is obtained by recognizing that the perturbation arises from the periphery of the atom where one may approximate R_a^+ by its asymptotic form, $R_a^+ \simeq c_l(kr)\exp(ikr + i\delta_l^a)$. Here $c_l(kr)$ is the curved wave factor[33] in the spherical Hankel function $h^{(+)}(kr) = c_l(kr)\exp(ikr)/kr$. For simplicity we model the perturbation as $\delta v(r) \simeq v_{mt}/[1+\exp(\zeta(R_{mt}-r))]$, where ζ characterizes the decay of the atomic potential tails near R_{mt}. The integral (4.3) can then be expressed as

$$\chi_e = -\frac{1}{kR_{mt}^2}|f_e|\sin(2kR_{mt} + 2\delta_l^a + \Phi_e). \tag{4.4}$$

where $f_e = |f_e|\exp(i\Phi_e)$ is an effective curved-wave scattering amplitude. With the above model the AXAFS is analogous to a damped harmonic oscillator, $f_e \sim \exp(-2\pi k/\zeta)/k$. For comparison to experiment, the Eq. (4.4) should have a few additional factors as in the usual XAFS formula, namely an amplitude reduction factor S_0^2, a Debye-Waller factor, $\exp[-2\sigma^2(R_{mt}/R)^2k^2]$, and a mean-free path term, $\exp(-2R_{mt}/\lambda)$.

4.4 Comparison with Experiment

AXAFS comparisons between the theoretical calculations and experimental results presented here are in reasonable agreement with each other (Fig. 4.2), especially for the simple oxides. The discrepancy at the edge for BaO is not fully understood, but may point to errors in FEFF's muffin-tin potential and energy reference. The long range oscillatory structure in the calculations is likely due to a small discontinuity in FEFF's muffin-tin potential at R_{mt}.

To check whether multi-electron excitations might also be present, we used the Z+1 model to estimate where the step for a two-electron excitation would begin. In this model excitation energies correspond to the ionization energies of Z+1 atoms, and are 99 eV for Ba and 113 eV for Ce, as indicated by arrows in Fig. 4.2. Small features in the background were previously attributed to multi-electron excitations based on this model[27, 28]. However, it is likely that part of the observed structure can also be attributed to AXAFS.

We point out that our calculations of the atomic backgrounds shown in Fig. 4.2 were all done with ground state exchange potentials. We found that the usual Hedin-Lundqvist (HL) self-energy model used in FEFF[30, 31] gives too large an oscillatory amplitude near threshold. This is an indication of the sensitivity of the AXAFS to the exchange interaction. Evidently improvements to FEFF's muffin-tin potentials are necessary, and AXAFS may be useful in assessing various improvements.

4.5 Discussion and Conclusions

It is well known that simple, monotonic approximations to the atomic background are not sufficient to obtain accurate XAFS data, emphasizing the importance of improved background removal methods[27, 28]. However, the atomic background μ_0 and the XAFS χ are tightly linked by the definition $\chi = (\mu - \mu_0)/\mu_0$, so the backgrounds obtained for theoretical and experimental standards may differ. Thus an understanding of AXAFS is essential to obtain experimental backgrounds. This difference also affects XAFS analysis; if one tries to isolate a Ce-O standard without taking its oscillatory background into account, one cannot obtain a good fit to the first Pr-O peak in PBCO. The inclusion of extra-atomic contributions in the atomic background may at first seem arbitrary. For example, the XAFS could be defined with respect to the bare atomic background, which is independent of the environment. However such a definition is problematical and inconsistent with multiple-scattering theory based on independent scattering sites; also because the exchange interaction is not additive, it is not possible to construct the scattering potential by superposing free atomic potentials.

For the materials discussed in this paper, the AXAFS is quite large, and is the dominant contribution to the background fine structure, exceeding multi-electron effects in magnitude. *Ab initio* calculations of the AXAFS agree reasonably well with these observations and with the simplified model introduced here. The size and character of these background features, particularly their interference with the first coordination shell peak, indicate that accurate fits to XAFS data must take them into account. AXAFS is also interesting in its own right, because it depends critically on the scattering potential in the outer part of the absorbing atom. Thus, it provides a new and useful probe of chemical effects, the electron self-energy, core-hole effects, and other contributions to the embedded atom potentials.

Chapter 5

Fluorescence-XAFS

Fluorescence-yield measurements of absorption have several advantages over the more traditional transmission experiment. The most important advantage is for materials with dilute amounts of the absorbing atom present. As the concentration is lowered, more and more of the incident light gets transmitted, until the measured absorption coefficient is completely dominated by the absorbing background. In the fluorescence configuration, background absorption can be at least partially masked because the energy of the fluorescing photon is both known and constant as the energy of the incident photon is varied for the XAFS scan. Near $Z = 30$, "notch filters" can be made by simply putting a thin sample of material with Z one less than the absorbing atom. For instance, for a Cu K_α fluorescence, a Ni filter will preferentially filter out both the incident beam (which is well above the Ni K-edge) and fluorescences at lower energy (since the absorption coefficient goes roughly as λ^3).

Another big advantage of the fluorescence configuration is for well-oriented samples. Since the absorption coefficient is polarization dependent, the combination of the high degree of polarization of synchrotron light and the (presumably) known orientation of the sample may allow certain scattering paths to be enhanced or eliminated. Well-oriented samples come in one of three forms: (1) single crystals, (2) oriented powders and (3) films. Oriented powders are generally not as well oriented as the other two, since the crystallites must be ordered by applying an external force, such as a magnetic field, and the medium which holds the powder (such as epoxy) may not allow the crystallites to fully orient. Also, this method necessarily assumes each particle is a "single" crystal, that is, does not consist of several crystal orientations (a particular problem for substituted samples). Such powders usually can be ordered better than 10%, sometimes even better. Single crystals and thin films are usually much better; usually a good single crystal or thin film is oriented to at least 2% and generally better than 1%. If the degree of orientation is important in the experiment, single crystals pose the problem that they are generally small, so placing them at a steep angle to the beam may make getting enough beam onto and through the sample impossible. Transmission experiments on films are usually impossible because of the substrate onto which the film is necessarily grown.

5.1 solid-state detection

Current detector technology has also enhanced the possibilities for obtaining information from FY XAFS experiments. Solid-state detectors, such as the 13-element Ge detectors at SSRL, have fairly good energy resolution ($\sim$ 300 eV) that allow for even a very small fluorescence peak to be measured. Background photons from the Compton scattered peak, other scattered peaks and other fluorescences can at least be reduced if not virtually eliminated by such high resolution. Another advantage is that the detector elements can be very small, allowing for multiple detectors to be used and thus provide some spatial resolution.

5.1.1 dead time

Unfortunately, the throughput of a solid-state detector is not nearly as good as a gas-ionization detector. For instance, the maximum throughput of the SSRL Ge detectors *before* the energy-resolving peak-shaping filters is on the order of several hundred thousand counts per second. Once the filters are included, the maximum count rate is less than 200 kcps ($\sim 5\mu$s). The primary effect on the XAFS signal is to reduce the amplitude of the absorption edge and the XAFS oscillation in e-space at higher count rates. Even at 50 kcps, the dead-time introduced by these filters is very significant compared to the statistics required for an XAFS experiment (at least one part in 10^3). Even if the experimenter repeats measurements on the same sample, different absorption coefficients will be measured due to the finite lifetime of the storage ring, which can cause up to a factor of two (SSRL, 1996) change in the incident beam flux (depending on beam line, energy, fill schedule, etc.).

Even larger changes in the measured intensity can occur if a diffraction occurs that sends a Bragg spot onto a detector. These can occur in well-oriented samples or substrates, and can occur from diffraction of either the incident beam or a fluorescence "beam." Since the incident beam is at a very different energy than the fluorescence signal, the effect of the incident beam being diffracted into a detector is to *decrease* the apparent fluorescence (Fig. 5.1). Since such diffractions can be fairly common, it is very important to be able to correct for this dead time.

The basic idea behind making a correction for the dead-time is rooted in the fact

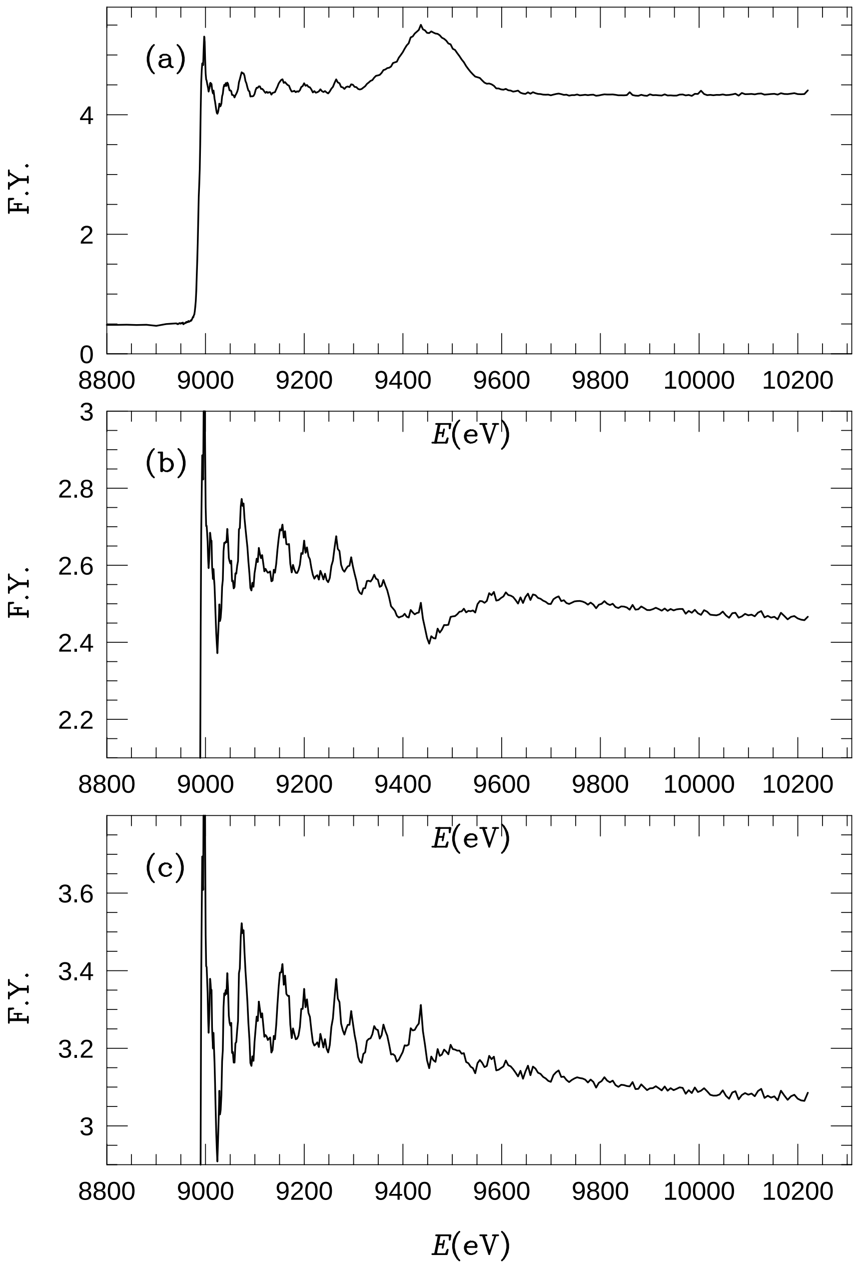

Figure 5.1: (a) Fluorescence yield (F.Y.) for the integrated count rate from channel 7 from the SSRL 13-element Ge detector array (I_{ICR}/I_0). The broad bump centered near 9450 eV is from diffraction off a 5000-Å film of YBCO on a MgO substrate. (b) Fluorescence yield from the same channel into the single channel analyzer windowed on the Cu K_α fluorescence ($I_{\mathrm{m}SCA}/I_0$). (c) The "true" fluorescence yield from the same channel after the dead-time correction (($I_{\mathrm{t}SCA}/I_0$).

that the shaping filters take a finite amount of time to shape the signal. The chance of a photon coming into the detector during this time is also proportional to a geometrical factor based on the energy resolution. The following equation contains the basic physics:

$$I_{\mathrm{mSCA}} = \kappa(I_{\mathrm{ICR}} - I_{\mathrm{offset}})e^{-(I_{\mathrm{ICR}} - I_{\mathrm{offset}})\tau}, \tag{5.1}$$

where I_{mSCA} is the measured count rate in the single-channel analyzer (set to measure the total counts within some energy range), I_{ICR} is the total count rate at all energies, κ is the fraction of the total count rate that would fall within the SCA energy range in the absence of any dead-time, τ is the dead-time and I_{offset} is an electronic background current (dark current).

All the quantities in Eq. 5.1 can be obtained by performing an experiment that allows Eq. 5.1 to be well defined. At least two conditions must be met: κ has to be a constant as a function of I_{ICR} and any dead-time in the collection of I_{ICR} has to be much smaller than the dead-time in I_{SCA} (τ). We typically collect a "dead-time scan" by using two sets of slits (parallel-plate apertures). The experimental set-up is shown in Fig. 5.2. The first set of slits are in front of the monochromator and are usually used to decrease the heating of the crystals. We vary the incident flux on a sample by scanning the table position and thereby changing the overlap of the second set of slits with the beam position as defined by the first set. The only possible problem with this method is that the part of the beam being used for each table position changes, and is different than whatever part of the beam is actually being used for an XAFS scan. This problem could result in a different energy spectrum at each table position, i.e. different harmonic content, and therefore would manifest in a κ that was not constant.

Fig. 5.3 shows I_{ICR} vs. I_0. The ionization counter can handle must higher count

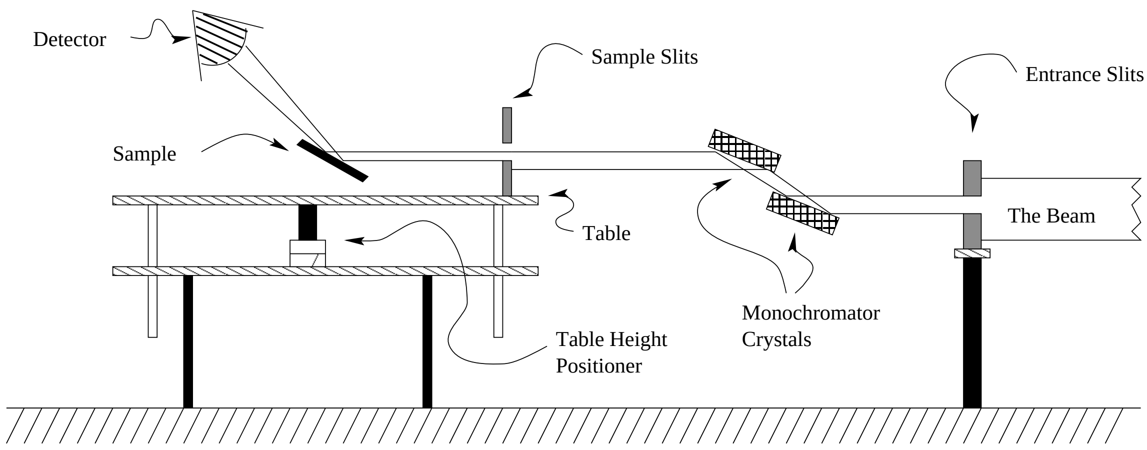

Figure 5.2: Schematic diagram showing the experimental setup for determining the appropriate dead-time correction. Flux on the sample is held at a fixed energy and changed in magnitude by varying the table height, and thus the overlap between the entrance slits and the sample slits.

rates than the Ge detector, so this plot gives us some idea how much any dead-time in $I_{\rm ICR}$ might affect our measurement, and if any other effects, such as a changing harmonic content, are causing any problems. In other words, this plot should represent a straight line in order to try and determine τ from the data. The data in Fig. 5.3 are linear to about 5% at 100 kcps. Assuming $I_{\rm ICR}$ represents the true total count rate measured by the detector, we can observe the effect of the dead-time on $I_{\rm SCA}$ in Fig. 5.4. The $I_{\rm ICR}$ at the maximum of $I_{\rm SCA}$ gives a quick measure of $\tau \cong 1/I_{\rm ICR}^{max}$. κ, $I_{\rm offset}$ and τ can be determined by fitting Eq. 5.1 to the data in Fig. 5.3. The results of this fit are shown in Table 5.1.

Now that the parameters from Eq. 5.1 are measured, we can apply them to any data set to get the true windowed count rate $I_{\rm tSCA}$:

$$I_{\rm tSCA} = I_{\rm mSCA} e^{(I_{\rm ICR} - I_{\rm offset})\tau} + \kappa I_{\rm offset}. \tag{5.2}$$

Fig. 5.5 shows the data from Fig. 5.4 after the application of Eq. 5.2.

Table 5.1: Typical fit results of dead-time data to Eq. 5.1. "det" refers to the detector number (out of 13), χ^2 is the statistical measure of the goodness of fit, and ν is the degrees of freedom.

det	κ	σ_κ	offset	σ_{offset}	τ	σ_τ	χ^2/ν
1	0.132	0.0005	342	11	4.467	0.019	3.3
2	0.082	0.0004	283	14	4.508	0.021	7.3
3	0.083	0.0004	249	16	4.960	0.019	12.1
4	0.139	0.0005	307	10	5.498	0.018	18.0
5	0.194	0.0006	370	8	5.091	0.016	10.5
6	0.571	0.0011	270	5	6.288	0.009	8.6
7	0.263	0.0007	272	8	6.172	0.013	8.9
8	0.329	0.0009	305	6	7.378	0.014	10.8
9	0.650	0.0013	341	4	7.002	0.011	34.6
10	0.246	0.0007	245	8	5.131	0.015	5.5
11	0.121	0.0005	244	11	5.330	0.019	2.5
12	0.309	0.0008	294	7	5.602	0.013	18.0
13	0.645	0.0010	428	5	5.294	0.006	77.8

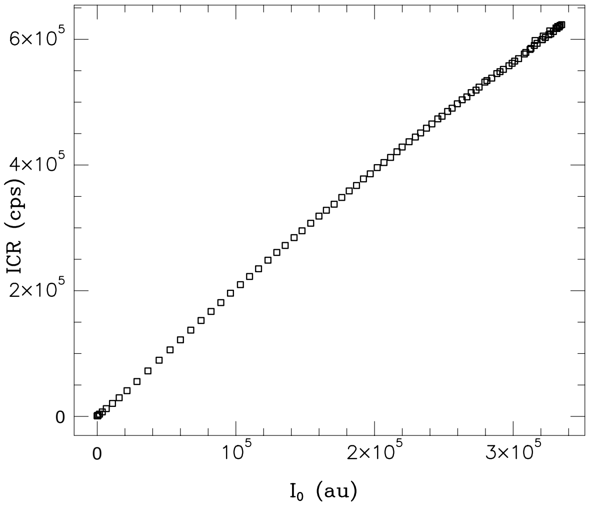

Figure 5.3: Dead-time curve for the total count rate (ICR) into detector #3. The I_0 counter has a negligible dead-time associated with its read-out, and therefore is assumed to be proportional to the real count rate. This figure shows that $\tau_{ICR} << 1\mu$s.

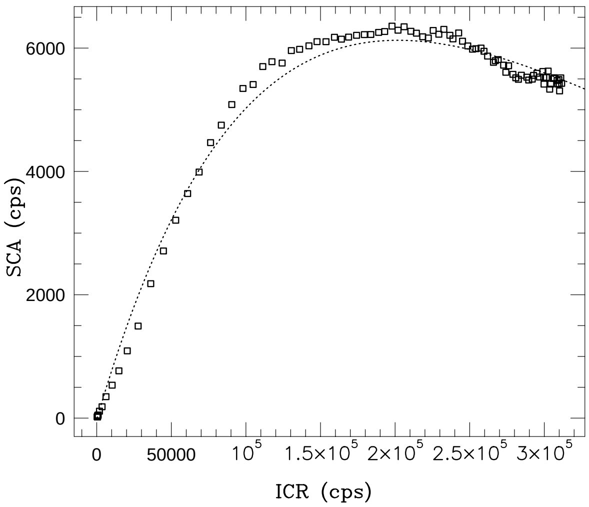

Figure 5.4: Dead-time curve for the windowed count rate (SCA) into detector 3. The peak in SCA occurs at ICR $\sim 2{\times}10^5$ cps, which indicates that $\tau_{\rm SCA} \sim 5\ \mu$s. The dotted line shows a fit of Eq. 5.1 to the data.

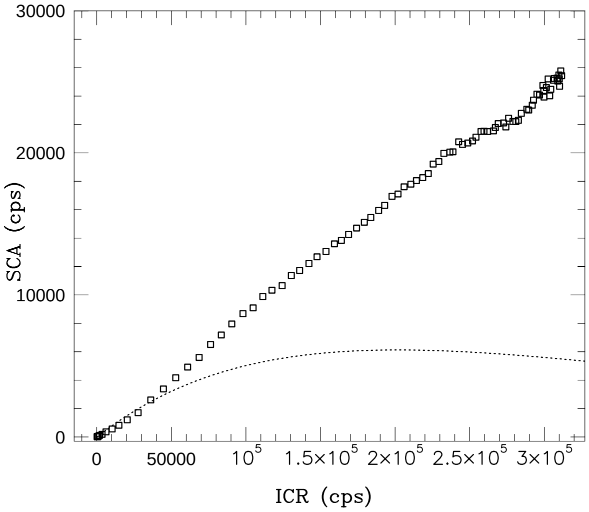

Figure 5.5: Corrected dead-time curve for the windowed count rate (SCA) into detector 3. The dotted line shows the fit in Fig. 5.4 for comparison.

5.1.2 Statistics

The dead-time introduced by the energy-resolving peak-shaping filters affects the statistical noise such that maximizing the count rate can actually be counterproductive. For instance, if the experimenter operates at the top of the curve of Fig. 5.4, i.e. $I_{ICR} \sim 1/\tau$, a higher count rate can actually *decrease* the number of counts in the SCA window. Although the correction given by Eq. 5.2 can, in principle, obtain the correct count rate, the statistical noise will be increased.

The ideal count rate, that is, the count rate that provides the best statistics is easily calculated. Our goal is to calculate the relative error on the corrected count rate, namely,

$$E^2 \equiv \frac{\sigma^2_{I_{\rm tSCA}}}{I^2_{\rm tSCA}} = \frac{1}{I^2_{\rm tSCA}} \left[(\frac{\partial I_{\rm tSCA}}{\partial I_{\rm mSCA}})^2 \sigma^2_{I_{\rm mSCA}} + (\frac{\partial I_{\rm tSCA}}{\partial I_{\rm ICR}})^2 \sigma^2_{I_{\rm ICR}} + (\frac{\partial I_{\rm tSCA}}{\partial \tau})^2 \sigma^2_\tau \right], \tag{5.3}$$

again ignoring the small effect of the offset. $\sigma_{I_{\rm mSCA}}$ can be calculated from Eq. 5.1 to be

$$\sigma^2_{I_{\rm mSCA}} = I^2_{\rm mSCA} (\frac{1}{I_{\rm ICR}} - \tau)^2 I_{\rm ICR} + I^2_{\rm ICR} I^2_{\rm mSCA} \sigma^2_\tau, \tag{5.4}$$

where I have used the fact that the error on $I_{\rm ICR}$ is simply $\sqrt{I_{\rm ICR}}$. E^2 can be written as

$$E^2 = I_{\rm ICR} \left[\tau^2 + (\frac{1}{I_{\rm ICR}} - \tau)^2 + 2 I_{\rm ICR} \sigma^2_\tau \right]. \tag{5.5}$$

Finally, we want to minimize this quantity, which occurs under the condition

$$0 = 2\tau^2 - \frac{1}{I^2_{\rm ICR}} + 4 I_{\rm ICR} \sigma^2_\tau. \tag{5.6}$$

If the error on τ is negligible, the "best" count rate is $I_{\rm ICR} = \frac{1}{\sqrt{2}\tau}$.

Using a typical maximum from Table 5.1 of $\sigma_\tau = 0.02\ \mu$s, the last two terms are only comparable for $I_{\rm ICR} \sim 1.4 \times 10^5$cps, which (coincidentally) is equal to $\frac{1}{\sqrt{2}\tau}$. Therefore, it is important to obtain the best possible measurement of τ is one wants to run at the optimal (in terms of S/N) count rate.

5.2 self-absorption correction

Under ideal circumstances (such as a very thin sample), the absorption coefficient is proportional to the number of fluorescence photons escaping a sample. The key to being able to make this assumption is that the mean depth in the sample at which the fluorescing photons are coming from is constant with energy. However, for thicker samples, the mean depth may change with energy, either from the basic λ^3 (Victoreen) dependence of μ, or from the XAFS oscillations themselves. The subsequent reduction in the XAFS amplitude (often larger than 50%) is known as the "self-absorption effect." This reduction can be calculated and thus corrected. The following discussion is partially due to Goulon *et al.*[36], but follows the notation of Tröger *et al*[37].

The fluorescence yield at the point of absorption is proportional to the x-ray flux at that point and the fluorescence efficiency. The radiation intensity at a depth y is

$$I = I_0 e^{-\mu(E)y}$$

The fluorescent photon then has to escape. The fluorescent flux from this point in the sample is then

$$I_f = I_0 e^{-\mu(E)y} e^{-\mu(E_f)z} \epsilon_a(E) \mu_a(E),$$

where $\mu_a(E)$ is the absorption due to the absorbing atom, $\mu(E)$ is the total absorption, $\epsilon_a(E)$ is the fluorescence efficiency, E is the incident beam energy, E_f is the energy of the fluorescing photon, and I'm assuming that all the measured fluorescence is coming from the desired process (eg. Cu K_α, any other counts can be subtracted off). This equation is only true at a particular y and z, so we must integrate

$$dI_f = I_0 \epsilon_a \mu_a e^{-(\mu_T y + \mu_f z)} dy.$$

Here I've dropped the energy dependences and used $\mu_T = \mu(E)$ and $\mu_f = \mu(E_f)$. z and y are dependent via $y \sin\phi = z \sin\theta \cong x$. Changing variables:

$$dI_f = I_0 \epsilon_a \mu_a \frac{1}{\sin\phi} e^{-(\frac{\mu_T}{\sin\phi} + \frac{\mu_f}{\sin\theta})x} dx$$

$$I_f = I_0 \epsilon_a \mu_a \frac{1}{\sin\phi} \int_0^d e^{-(\frac{\mu_T}{\sin\phi} + \frac{\mu_f}{\sin\theta})x} dx \tag{5.7}$$

$$I_f = -\frac{I_0 \epsilon_a \mu_a}{\mu_T + g\mu_f} \left[1 - e^{-(\frac{\mu_T}{\sin\phi} + \frac{\mu_f}{\sin\theta})d} \right], \tag{5.8}$$

where I've defined $g \cong \frac{\sin\phi}{\sin\theta}$ and d to be the thickness of the sample. This is the *total* fluorescence. If the experimenter wants to get the fluorescence measured by a detector, a factor of $\frac{A}{r^2}$ (where A is the detector area and r is the distance from the sample to the detector) must be included. For the rest of this discussion, such a factor would just ratio out.

In XAFS, we want

$$\chi = \frac{\mu_a - \bar{\mu_a}}{\bar{\mu_a}},$$

but what we actually calculate experimentally is

$$\chi_{exp} = \frac{I_f - \bar{I_f}}{\bar{I_f}},$$

where $\bar{I_f}$ is the spline function fit to the data to simulate what the fluorescence would be without the XAFS oscillations. I will now make the following substitutions:

$$\mu_T = \bar{\mu_T} + \chi\bar{\mu_a} \tag{5.9}$$

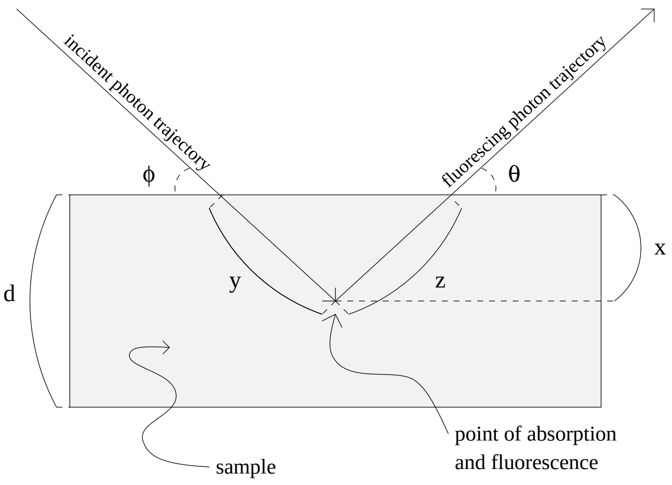

Figure 5.6: Geometry used in calculating self-absorption correction in XAFS

$$\mu_a = (\chi+1)\bar{\mu_a} \tag{5.10}$$

$$\mu_T - \bar{\mu_T} = \mu_a - \bar{\mu_a}. \tag{5.11}$$

Now we can plug these equations and the equation for I_f into χ_{exp}:

$$1+\chi_{exp} = \frac{\mu_a(\bar{\mu_T}+g\mu_f)[1-e^{-(\frac{\mu_T}{\sin\phi}+\frac{\mu_f}{\sin\theta})d}]}{\bar{\mu_a}(\mu_T+g\mu_f)[1-e^{-(\frac{\bar{\mu_T}}{\sin\phi}+\frac{\mu_f}{\sin\theta})d}]}$$

Dividing by $1+\chi$ and defining $\alpha \equiv \bar{\mu_T}+g\mu_f$, we get:

$$\frac{1+\chi_{exp}}{1+\chi} = \frac{[1-e^{-(\bar{\mu_T}+\chi\bar{\mu_a}+g\mu_f)\frac{d}{\sin\phi}}]\alpha}{(\alpha+\chi\bar{\mu_a})[1-e^{-\frac{\alpha d}{\sin\phi}}]}.$$

Now we can write χ_{exp} in terms of the actual χ:

$$\chi_{exp} = \frac{1-e^{-(\alpha+\chi\bar{\mu_a})\frac{d}{\sin\phi}}}{1-e^{-\frac{\alpha d}{\sin\phi}}}\frac{\alpha(\chi+1)}{\alpha+\chi\bar{\mu_a}} - 1. \tag{5.12}$$

At this point in the calculation, the relation between χ and χ_{exp} is exact. However, Eq. 5.12 is for χ_{exp} in terms of χ, when what we really want is the other way around. In order to invert Eq. 5.12, I will make a simple approximation. Assuming that

$$\frac{\chi\bar{\mu_a}d}{\sin\phi} << 1$$

we can say

$$1 - e^{-(\alpha + \chi\bar{\mu_a})\frac{d}{\sin\phi}} \sim 1 - e^{-\frac{\alpha d}{\sin\phi}}(1 - \frac{\chi\bar{\mu_a}d}{\sin\phi}).$$

This approximation gets worse with large χ and $\bar{\mu_a}$. It also has a maximum for both ϕ and d, because of the $e^{-\frac{\alpha d}{\sin\phi}}$ term. Plugging in some typical numbers from the Cu K-edge of YBCO ($\phi = 10°, \bar{\mu_T} = 0.132, \mu_F = 0.1095, \bar{\mu_a} = 0.1$ and $\chi = 0.5$) the maximum error is $\sim$ 2.7% at a thickness of $\sim 1.9\mu$m. Such a high value of χ does not actually occur in YBCO. Indeed, such a high χ is very rare. In any case, various combinations of the above parameters can conspire to produce errors above 1%, so the approximation should be monitored when making the corrections outlined below.

With the above approximation, and defining the following quantities:

$$\begin{aligned} \beta &= \frac{\bar{\mu_a} d\alpha}{\sin\phi} e^{-\frac{\alpha d}{\sin\phi}} \\ \gamma &= 1 - e^{-\frac{\alpha d}{\sin\phi}}, \end{aligned}$$

Eq. 5.12 is reduced to a quadratic equation in χ and we can finally write the full correction formula:

$$\chi = \frac{-[\gamma(\alpha - \bar{\mu_a}(\chi_{exp}+1)) + \beta] + \sqrt{[\gamma(\alpha - \bar{\mu_a}(\chi_{exp}+1)) + \beta]^2 + 4\alpha\beta\gamma\chi_{exp}}}{2\beta}, \tag{5.13}$$

where the sign of the square root is determined by taking the thick or thin limits. In the thick limit ($d \to \infty$), Eq. 5.13 gives:

$$\chi = \frac{\chi_{exp}}{1 - \frac{\bar{\mu_a}}{\alpha}\chi_{exp} - \frac{\bar{\mu_a}}{\alpha}}, \tag{5.14}$$

which is the same equation as calculated in Ref. [37] without the χ_{exp} term in the denominator. In the thin limit, it can be shown that Eq. 5.13 reduces to $\chi = \chi_{exp}$, as expected.

5.2.1 effect of XAFS on correction

For disordered materials, including the XAFS in the correction term will have a small effect on Eq. 5.13 (for instance, one could take $\chi_{exp} = 0$ in the denominator of Eq. 5.14 as in Ref. [37]). However, for well-ordered, thick materials, χ can have a surprisingly large effect. Fig. 5.7 shows the correction for Cu K-edge absorption data from a 17 μm-thick single crystal of $YBa_2Cu_{2.958}Ni_{0.042}O_{6.95}$. The sample is oriented with the polarization vector $\vec{\epsilon}$ perpendicular to the surface of the film, which maximizes the correction term. The orientation and the thickness of the material combine for a large average correction ($\sim$ 1.6). On top of the average correction, the effect of the XAFS causes a 6% variation of the correction at $k \sim 4\text{Å}^{-1}$. The magnitude of this term is comparable to the current error limits on S_0^2[17], and should be taken into account.

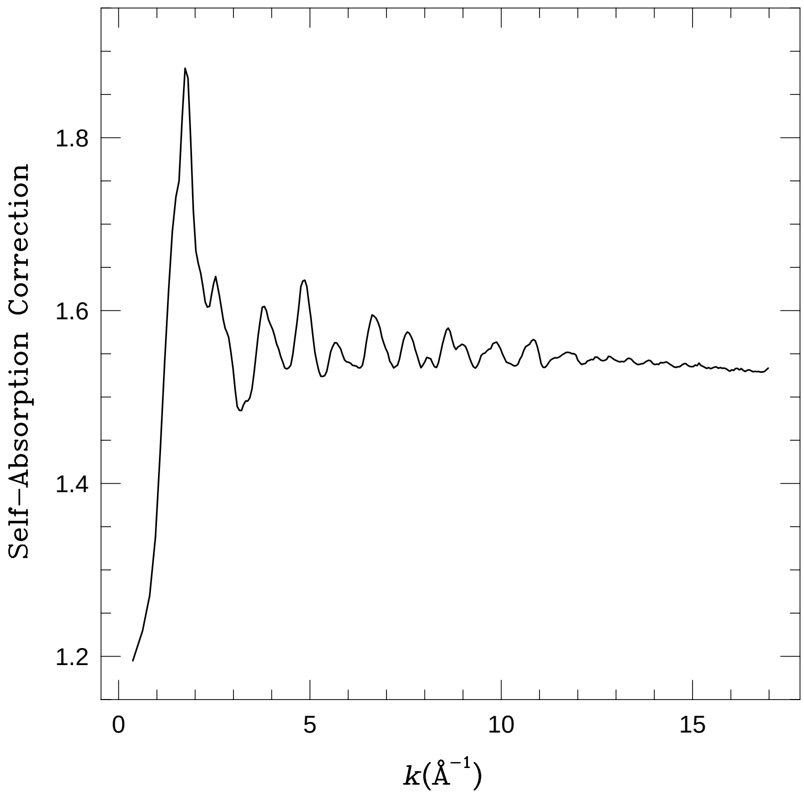

Figure 5.7: Correction given by Eq. 5.13 for Cu K-edge absorption data from a 17 μm-thick single crystal of $YBa_2Cu_{2.958}Ni_{0.042}O_{6.95\pm0.005}$. The sample is oriented with the polarization vector $\vec{\epsilon}$ perpendicular to the surface of the film, which maximizes the correction term.

Chapter 6

Phase-lock XAFS (PLEXAFS?)

The XAFS technique is a very powerful probe for identifying local structure, even in systems where one wants to know the structure around a dilute species of atom. However, sometimes an experimenter may want to look for a change in the structure accompanying a phase transition that may be quite small. Unfortunately, fundamental problems exists for all experiments investigating tiny structural changes: there are unavoidable systematic differences from one data point to the next. These errors occur primarily because it takes time to move from one temperature (for example) to the next. During this time, beam alignment may change, the temperature may fluctuate, etc. Beam movement can be a particularly frustrating problem because it changes the distribution of flux across the sample for beams that do not have a uniform intensity profile. In XAFS these changes in the intensity profile causes different parts of a sample with perhaps spatially varying stoichiometry to be probed. More importantly, these changes can couple to variations in sample thickness (especially pin holes) to produce "glitches"[38]. Yet another systematic error that plagues XAFS occurs when studying well-oriented single crystals or (especially) thin films. When the beam angle and energy match a Bragg condition, a significant amount of flux can be lost to diffraction, sometimes directly into the detector. Although these "events" are completely reproducible, it can be very difficult to account for them in the data analysis. All of these systematic errors conspire to make up the dominant noise source, limiting fits to XAFS data, for instance, to a signal (counts measured) to noise ratio (S/N) of about 2000. Even S/N as high as 2000 is rarely achieved. In light of the fluxes available from a typical wiggler beam line at a synchrotron x-ray source, such a low S/N ratio is particularly unfortunate.

The dominant noise sources mentioned above all have power spectra that fall off rapidly with frequency. If an experimenter is really only interested in two different states of a system that may be accompanied by a structural change, and if an experiment can be designed that switches the state of the sample at a frequency that reduces the "dominant" noise sources below the noise from counting statistics, then a simple "phase-lock" detection scheme (taking the difference of the data in the two states) can be utilized.

6.0.2 Interpretation of phase-lock data

We can estimate the signal obtained by taking the difference of two spectra from the derivative of the XAFS equation. With a Gaussian pair-distribution function, χ is given by

$$\chi = \sum_i \frac{S_0^2 F_i(k) N_i e^{-\frac{r}{\lambda}}}{\sqrt{2\pi}\sigma_i} Im \int_0^\infty \frac{e^{-\frac{(r-r_i)^2}{2\sigma_i^2}} e^{i(2kr+\phi_i)}}{kr^2} dr. \tag{6.1}$$

We can model the lock-in signal by Taylor-expanding this equation and keeping the lowest order term proportional to the change of a structural parameter. In order to utilize the power of the Fourier transform, I will only expand the integrand of Eq. 6.1, which at $r = r_i$

is equal to the amplitude r-space data. For a shift in the distance of an atom pair, we have

$$\left[\frac{\partial\chi}{\partial r_i}\right]_{r=r_i} = \left[\frac{-A_i(r-r_i)e^{-\frac{(r-r_i)^2}{2\sigma_i^2}}e^{i(2kr+\phi_i)}}{r^2}\right]_{r=r_i} = 0 \tag{6.2}$$

$$\left[\frac{\partial^2\chi}{\partial r_i^2}\right]_{r=r_i} = \left[\frac{A_i}{r^2\sigma_i^2}e^{-\frac{(r-r_i)^2}{2\sigma_i^2}}\left[1+\frac{r-r_i}{\sigma_i^2}\right]e^{i(2kr+\phi_i)}\right]_{r=r_i} = \frac{A_i}{r_i^2\sigma_i^2}e^{i(2kr_i+\phi_i)} \tag{6.3}$$

$$= \frac{\chi(r_i)}{\sigma_i^2} \tag{6.4}$$

where $A_i = \frac{S_0^2F_i(k)N_ie^{-\frac{r}{\lambda}}}{\sqrt{2\pi}\sigma_ik}$ and I've made the assumption that $F_i(k)$ depends slowly on r_i for small shifts of r_i (Δ_{r_i}). We can now write the signal size for a given shift Δ_{r_i} as

$$\Delta_{r_i} = \sqrt{2\sigma_i^2\frac{\Delta\chi(r_i)}{\chi(r_i)}}, \tag{6.5}$$

where $\Delta\chi(r_i)$ is the change (difference) between $\chi(r_i)$ at the two extremes of the state-modulation.

For a shift in the pair-distribution width (Δ_{σ_i}), we need

$$\left[\frac{\partial\chi}{\partial\sigma_i}\right]_{\Delta_{sigma_i}=0,r=r_i} = \left[B_i\left(-\frac{1}{\sigma_i^2}+\frac{(r-r_i)^2}{\sigma_i^4}\right)e^{-\frac{(r-r_i)^2}{2\sigma_i^2}}e^{i(2kr+\phi_i)}\right]_{\Delta_{sigma_i}=0,r=r_i} \tag{6.6}$$

$$= -\frac{B_ie^{i(2kr_i+\phi_i)}}{\sigma_i^2}, \tag{6.7}$$

where $B_i = \frac{S_0^2F_i(k)N_ie^{-\frac{r}{\lambda}}}{\sqrt{2\pi}k}$. The signal size for a given shift Δ_{σ_i} is then

$$\Delta_{\sigma_i} = -\frac{\Delta\chi(r_i)}{\chi(r_i)}\sigma_i. \tag{6.8}$$

Both Eq. 6.5 and Eq. 6.8 are easily tested by making FEFF simulations. Shifts of $\frac{\Delta_{r_i}}{r_i}$ of $\sim 5\%$ can give errors in $\Delta(\chi(r_i))$ between Eq. 6.5 and the simulation of up to 10%, presumably because shifts in the near-neighbors can have an effect on $F_i(k)$, which was assumed to be negligible in the derivations above. A shift of $\frac{\Delta_{\sigma_i}}{\sigma_i} = 20\%$ gave an absolute error in $\Delta\chi(r_i)$ less than 2% comparing a simulation to Eq. 6.8.

6.0.3 A sample problem in high-T_c

One example of a structural problem that seems to be below the S/N level of current experiments occurs in the high-temperature superconducting cuprates. There is increasing evidence for small structural changes in the high-temperature superconductors that occurs at or near the superconducting temperature T_c. This possible structural change may be associated with small charge redistributions that take place at T_c. Evidence supporting this notion includes ion channeling experiments[8] and XAFS experiments which show split copper-axial oxygens distributions in Tl compounds[39] and possibly in YBCO[40]. Raman scattering[41, 42] and ultrasonic studies[43, 44] also indicate possible structural anomalies that appear to correlate with T_c.

One way to determine what structural changes are related to superconductivity is to devise an experiment that would only be sensitive to changes in structure that are induced when the sample becomes superconducting. The accepted experiments for structural probes do *not* fall into this category. Temperature dependent diffraction experiments explore the average structure, which may include changes with temperature, but small changes may be lost in the overwhelming signal from the rest of the structure; diffraction studies have not clearly seen any structural anomalies in YBCO that correlate with T_c[45]. Standard XAFS experiments suffer from a similar problem, although they probe local structure rather than average structure. Channeling experiments have indicated that correlated motions of the Cu(1)-O(4)-Cu(2) chains perpendicular to the c-axis must be occurring[8] but are not sensitive to any more detailed information. Raman and ultrasonic measurements don't give exact information as to what in the crystal changes near T_c.

One simple approach to this problem is to exploit the fact that we are looking only for *changes* in the structure (i.e. small changes in the distances between atoms in the unit cell) when the sample becomes a superconductor. If we can turn the superconductivity on and off, and thereby modulate the distances or some other structural parameter within the unit cell, we can use lock-in detection to observe the changes in the XAFS function. This approach virtually eliminates the systematic noise sources enumerated above, as we demonstrate below.

6.1 Experimental setup

We chose to cycle the state of the sample by modulating the temperature above and below T_c. We obtained some 4500 Å c-axis films of YBCO with various oxygen concentrations from H. Kinder and W. Prusseit at Technische Universität, München. These films have been grown on ~0.1 mm sapphire substrates to allow the thermal mass of the film+substrate to be as small as possible. Also, a 65 Å film of NiCr was deposited on the opposite side of the substrate which we use as a resistive heater ($\sim$ 33 Ω). We then cycle the YBCO film between the SC and the normal states by sending a current pulse ($\sim$ 80 mA) into the NiCr film (Fig. 6.1). A standard four-point probe on the YBCO film with a small current ($\sim$ 10 mA) across the sample allows a measurement of the state of the film by measuring the voltage drop. This system can be cycled between the normal and SC state with a frequency of up to 5 Hz, depending on the amount of exchange gas in the cryostat and the size of the heat pulse (Fig. 6.2). We found that a 2 Hz heat pulse produced a very stable modulation of the state. Triggering signals for the detector are built from this signal and from the master clock used by the beam-line computer. This system allows for (non-counting) noise sources with characteristic frequencies above 2 Hz to enter into the

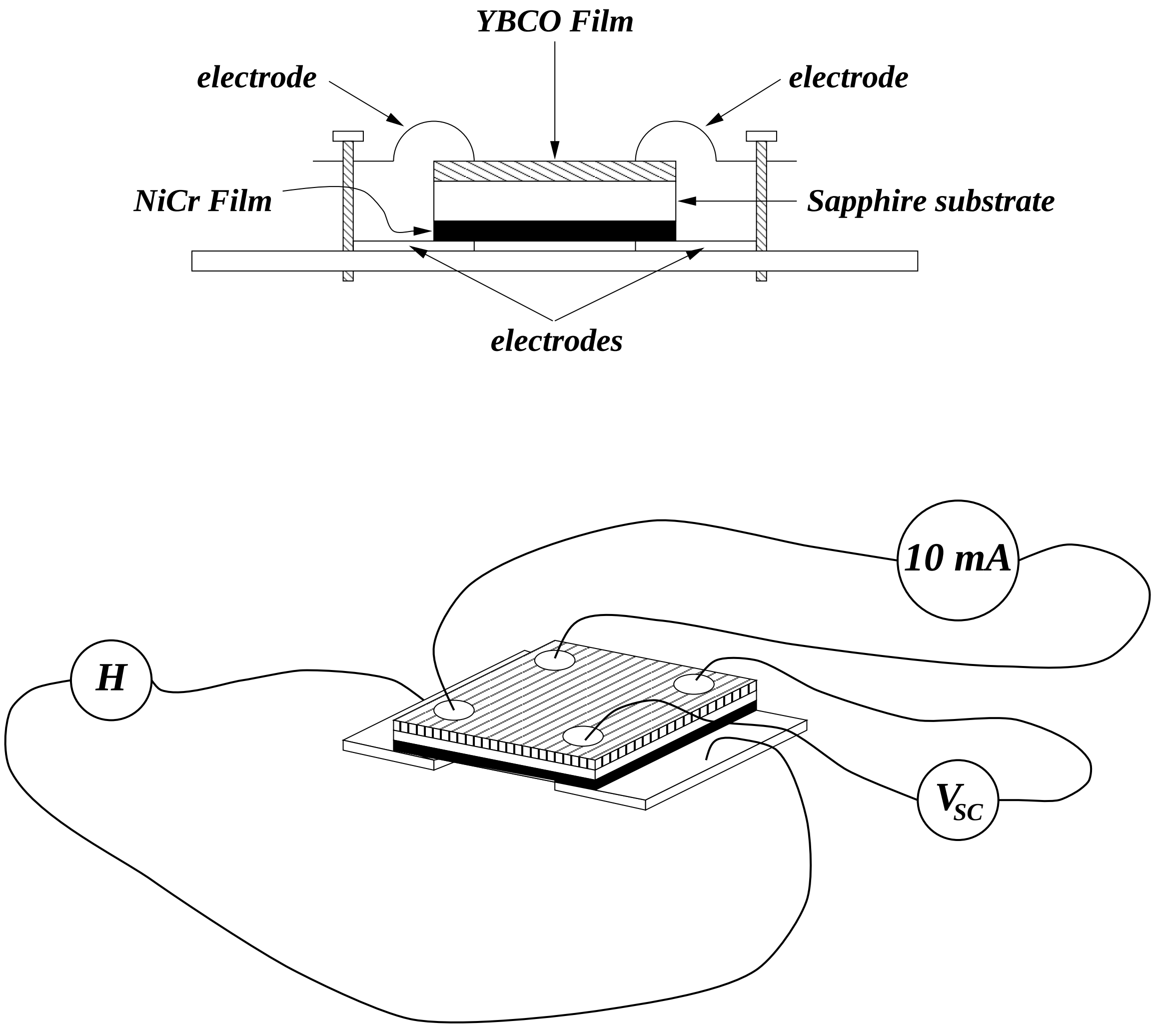

Figure 6.1: Basic set-up for modulating the state of a thin film of YBCO.

data.

The sample and probe are placed in a LHe flow cryostat, with a thermocouple placed about 3 cm from the sample. We estimate the systematic error in temperature to be less than 0.5 K for this experiment. Temperature is regulated to within 0.1 K. The sample was placed at a 57° angle to the incoming beam to simulate a random orientation of the film. Fluorescent x-rays emitted by the sample were detected using the 13-element Ge detector array available at SSRL. Detector channels 2,3,4, and 7 were counted using

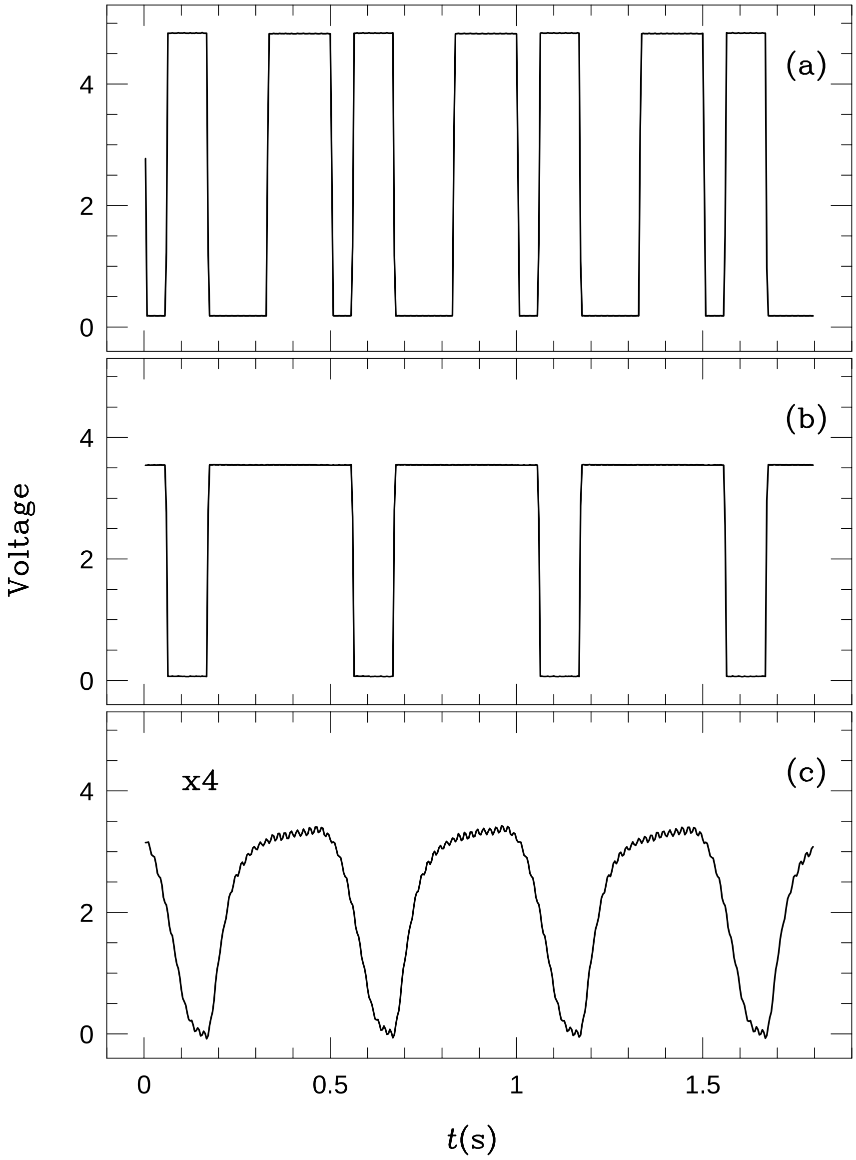

Figure 6.2: Reference signal used for switching detector memory. (a) Signal C, determining whether data is collected (high) or not (low), (b) signal M, determining state of sample (high indicates normal), and (c) V_{SC}, the voltage across the sample. Triggering points for C and M were set either by a reference voltage compared to V_{SC}, or by a separate timing circuit.

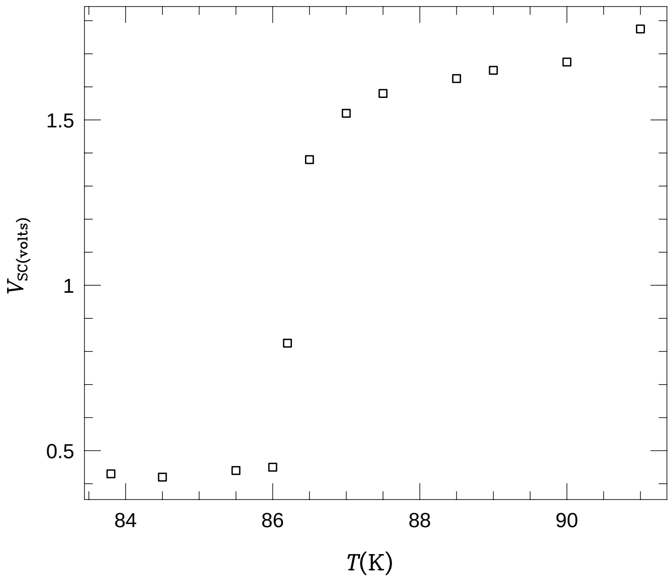

Figure 6.3: Amplified voltage measured across the YBCO film (V_{SC}) with a 10 mA current flowing thought it as a function of temperature.

read-out electronics supplied by W. Warburton and B. Hubbard at X-ray Instrumentation Associates (XIA). Their system allows the input of two switching signals which allow data to be stored in two locations. The basic signals are C, which determine whether data should be collected or not, and M, which determines in which of the two memory locations data should be stored (Fig. 6.2).

We performed three experiments with this apparatus on a fully oxygenated 4500-Å film of YBCO (T_c=86.3 K, Fig. 6.3). We collected data with a modulated temperature as depicted in Fig. 6.2 with the temperature pulsing from approximately 84.5 K to 87.5 K (referred to as "big" in the text below). We also collected data where we pulsed the temperature from $T = 86K \sim T_c$ to above T_c at 89 K("fluc"), and always above T_c, from about 89 K to 92 K("above").

6.2 Analysis

This experiment is designed to measure very small signals, and as such I have defined an expression that tests for the presence of such a signal:

$$S = \frac{2(\mu_N - \mu_{SC})}{(\mu_N + \mu_{SC})}, \tag{6.9}$$

where μ_N and μ_{SC} are the absorption coefficients in the normal and superconducting states, respectively. This equation is similar to the difference of the XAFS equations for the normal and SC states, since $\mu_0 \sim < \mu >= (\mu_N + \mu_{SC})/2$, the main difference being that all the quantities have measurable errors (reliable errors on μ_0 are impossible to determine). Fig. 6.4 shows this quantity with error bars for a modulation between the SC and N states, and Table 6.1 compares the mean of the amplitude squared to the variance for the same data. $< S^2 >$ would be significantly larger than σ_S^2 in the presence of a measurable signal. The results displayed in Table 6.1 show that within the limits set by counting statistics for this experiment, we measure no significant amplitude of S. Table 6.1 also shows these statistics for the modulation only above T_c and for the modulation between the transition temperature and above T_c. We see no statistical data for any of these data sets that is inconsistent with purely counting statistics.

6.3 Limits on structural changes

Although we measured no signal from a structural change, the noise level given by counting statistics puts certain limits on the possible structural changes that might be

Table 6.1: Signal statistics for a modulating signal between below T_c to above T_c.

	Big		Fluc		Above	
Run	$\sum_i^{nx} S_i^2$	$\sum_i^{nx} \sigma_{S_i}^2$	$\sum_i^{nx} S_i^2$	$\sum_i^{nx} \sigma_{S_i}^2$	$\sum_i^{nx} S_i^2$	$\sum_i^{nx} \sigma_{S_i}^2$
11	6.9 $\times 10^{-4}$	7.6$\times 10^{-4}$				
12	9.4	8.2				
13	9.2	10.3				
14	2.9	2.4				
15	3.6	3.5				
16	3.1	3.5				
31	4.7	4.2				
39	5.7	7.6				
40	8.7	8.3				
35			6.5 $\times 10^{-4}$	5.9$\times 10^{-4}$		
36			5.3	6.1		
37			6.8	6.5		
38			6.6	6.9		
17					3.4 $\times 10^{-4}$	3.6$\times 10^{-4}$
19					3.5	2.8
20					2.9	2.2
27					5.0	6.0
28					11.9	11.1
32					4.0	5.0
run average	8.6 $\times 10^{-5}$	7.7 $\times 10^{-5}$	1.5 $\times 10^{-4}$	2.1 $\times 10^{-4}$	8.3 $\times 10^{-5}$	10.0 $\times 10^{-5}$

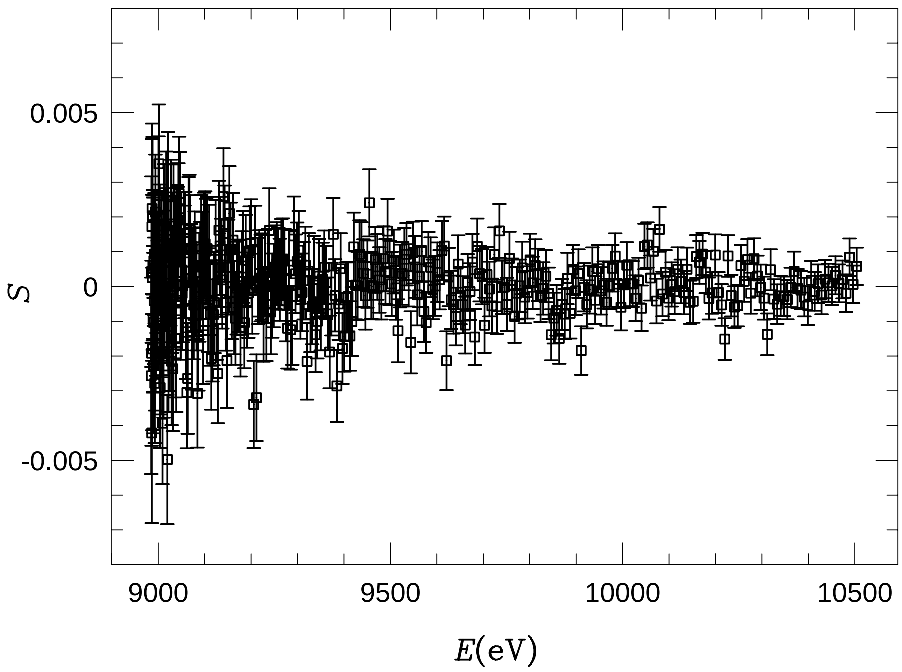

Figure 6.4: S vs. E for the difference between the normal and superconducting state absorption coefficients.

occurring. Fig. 6.5 shows the k-space data of (a) $\chi_{SC}(k)$, (b) $\Delta(\chi(k))$ obtained from

$$\chi(k) = \frac{\mu_N - \mu_{SC}}{\mu_0}$$

where μ_0 is obtained by fitting a spline through $\mu_{tot} = \frac{\mu_N + \mu_{SC}}{2}$ in the usual way, and (c) the difference of $\chi_N(k)$ and $\chi_{SC}(k)$ for traces taken at different times. The data in (c) were reduced quickly, i.e. no special effort was made to remove glitches and Bragg spikes. The effect of the lock-in method is very clear in this figure. The main effect of using the lock-in technique is to remove the effect of the Bragg diffraction spikes in the regular data.

The data in Fig. 6.5 can be transformed into r-space in the usual way. Fig. 6.6 shows the final transforms for the averaged data for the four experiments. Since we know that there is no signal above the counting statistics in these traces from Sec. 6.2, we can take the mean amplitude of the transforms as an estimate of the maximum $\Delta\chi(r_i)$ that

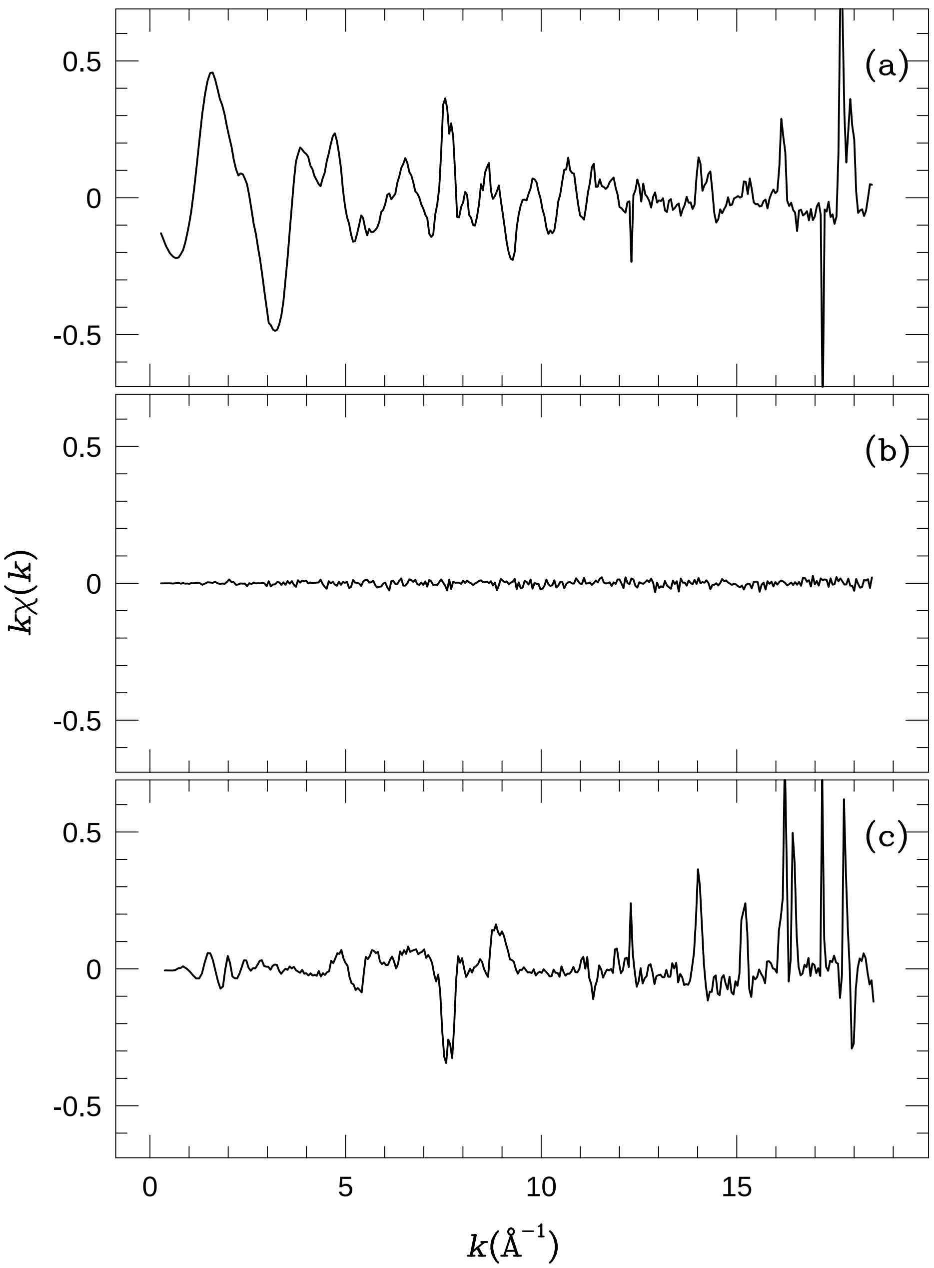

Figure 6.5: (a) The XAFS signal from the part of the modulated absorption that was below T_c. (b) $k\Delta\chi(k)$. (c) Difference of traces at $T < T_c$ and $T > T_c$ collected at different times for comparison to (b).

Table 6.2: Limits on shifts of r_i and σ_i for data above and below T_c ($\Delta_{r_i,big}$,$\Delta_{\sigma_i,big}$), at T_c and above T_c ($\Delta_{r_i,big}$,$\Delta_{\sigma_i,big}$), and a similar ΔT but always above T_c ($\Delta_{r_i,big}$,$\Delta_{\sigma_i,big}$). All units shifts are in Å. $|\chi(r_i)|$ and σ_i are based on FEFF simulations, and are known to be accurate to 10% for this crystal and this calculation.

path	$\|\chi(r_i)\|$	σ_i	$\Delta_{\sigma,big}$	$\Delta_{\sigma,fluc}$	$\Delta_{\sigma,above}$	$\Delta_{r_i,big}$	$\Delta_{r_i,fluc}$	$\Delta_{r_i,above}$
Cu1-O4	0.14	0.062	0.0028	0.0038	0.0037	0.018	0.022	0.021
Cu1-O1	0.13	0.063	0.0031	0.0043	0.0041	0.020	0.023	0.023
Cu1-Ba	0.30	0.041	0.0009	0.0012	0.0012	0.008	0.010	0.010
Cu1-Cu1ms	0.05	0.051	0.0061	0.0084	0.0081	0.025	0.029	0.029
Cu1-O4-Cu2	0.08	0.047	0.0039	0.0054	0.0052	0.019	0.023	0.022
Cu2-O2,3	0.51	0.064	0.0008	0.0011	0.0011	0.010	0.012	0.012
Cu2-O4	0.08	0.084	0.0066	0.0091	0.0088	0.033	0.039	0.038
Cu2-Y	0.31	0.043	0.0009	0.0012	0.0011	0.009	0.010	0.010
Cu2-Cu2c	0.05	0.047	0.0055	0.0076	0.0074	0.023	0.027	0.026
Cu2-Ba	0.32	0.041	0.0008	0.0011	0.0011	0.008	0.010	0.009
Cu2-O2,3l	0.08	0.073	0.0057	0.0079	0.0076	0.029	0.034	0.033
Cu2-Cu2ms	0.25	0.051	0.0013	0.0018	0.0017	0.011	0.014	0.013
Cu2-O4-Cu1	0.07	0.047	0.0040	0.0055	0.0054	0.019	0.023	0.022

might be present to give maximum Δ_{r_i} and Δ_{σ_i} for each scattering path. From Eq.s 6.5 and 6.8 we can write

$$\Delta_{r_i} = \sqrt{2\sigma_i^2 \frac{|\Delta\chi(r_i)|}{|\chi(r_i)|}} \tag{6.10}$$

$$\Delta_{\sigma_i} = \sigma_i \frac{|\Delta\chi(r_i)|}{|\chi(r_i)|}. \tag{6.11}$$

The average amplitude of the lock-in transforms in Fig. 6.6 are

$$< |\Delta\chi(r_i)| >_{big} = 0.0063$$

$$< |\Delta\chi(r_i)| >_{fluc} = 0.0084$$

$$< |\Delta\chi(r_i)| >_{above} = 0.0087,$$

where, again, the subscript "big" refers to a jump from T=84.5 K to 87.5 K, "fluc" refers to a jump from 86 K to 89 K and "above" refers to a jump from 89 K to 92 K. Table 6.2 summarizes the limits on the shifts.

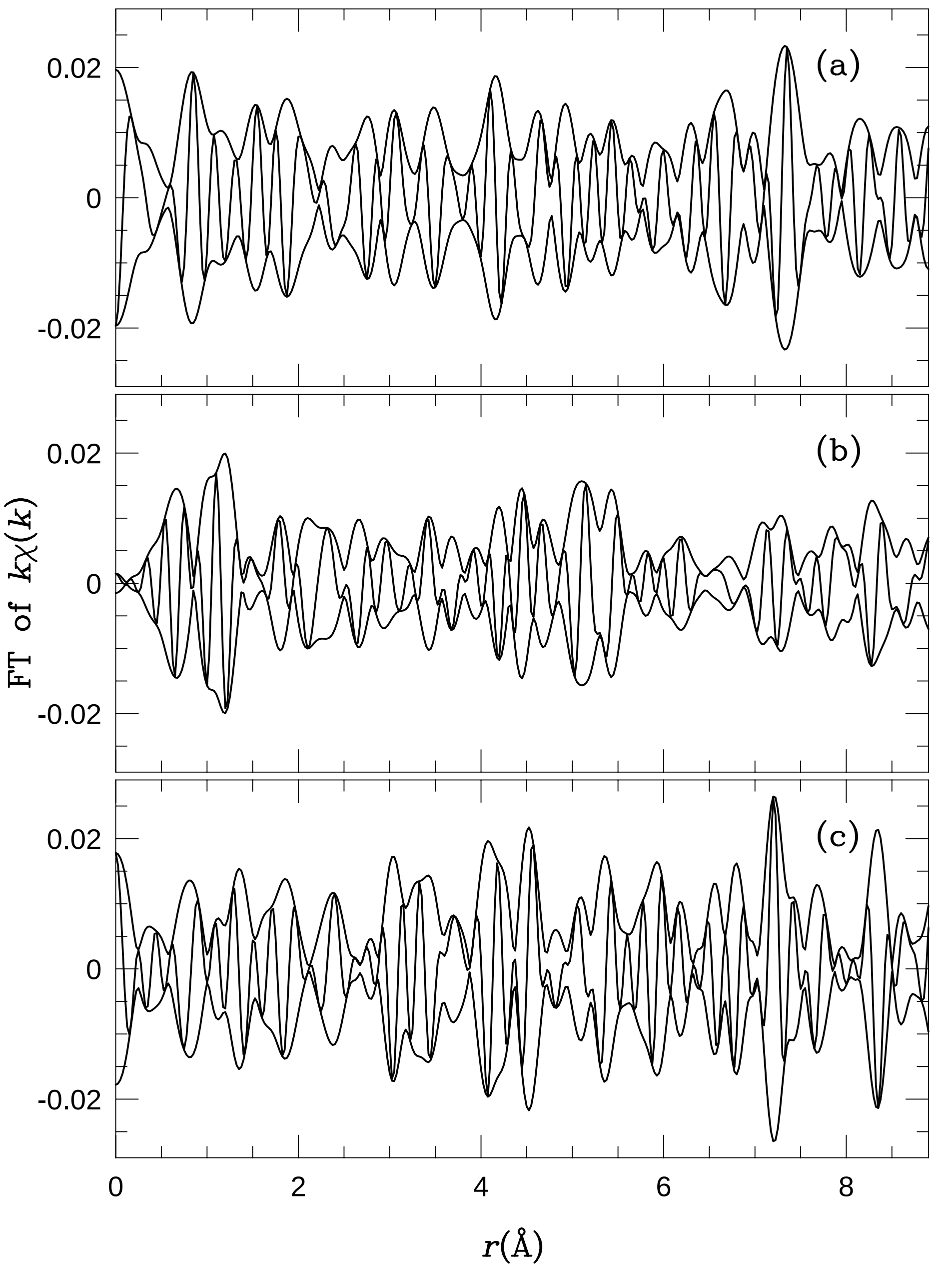

Figure 6.6: The FT of $k\Delta\chi(k)$ from 1.5-18.5 Å^{-1} and Gaussian broadened by 0.3 Å^{-1} for difference between data (a) below and above T_c, (b) at and above T_c and (c) always above T_c. See text for temperatures.

6.4 Discussion

Although many of these limits may not represent the highest precision of any previous XAFS experiments, they do rule out several features in the data reported in Chap. 9, and help clarify the character of some of the oxygen bonds which previous measurements suggested were changing above and below T_c[40]. In particular, the fluctuations in the $\sigma_{Cu(1)-O(4)}$ in Fig. 9.8 near T_c do not appear to occur according to the limits in Table 6.2. Since the fluctuations near T_c in Fig. 9.8 are just outside the error bars, this result is not very surprising. The better resolved jump in $\sigma_{Cu(2)-O(4)}$ in Fig. 9.8 is, unfortunately, below the noise limit of the lock-in data.

One of the more interesting results apparent in Table 6.2 is that the technique can place such stringent limits on so many of the atom-pairs' changes near T_c. These limits are small because we are only considering changes in a single pair of atoms when we calculate the possible shifts. Therefore, the usual interference between neighboring peaks in the XAFS spectrum does not occur, and we can use the full amplitude of an atom-pair. For instance, this separation of the paths enhances the Cu-Ba peak amplitudes by nearly a factor of two. *However*, if two neighboring atom pairs each shift as the temperature is modulated, the effective amplitude ($|\chi(r_i)|$) will be smaller (larger), and the limit on any shifts will be larger (smaller). This situation almost certainly would occur for the Cu(1)-O(4)-Cu(2) and the Cu(2)-O(4)-Cu(1) scattering paths, since they describe practically the same path.

6.5 Conclusions

This experiment successfully placed stringent limits for changes of local atoms around the coppers in a film of YBCO at the superconducting transition. In particular, a measured jump in $\sigma_{Cu(1)-O(4)}$ below T_c from Chap. 9 has been determined to not occur for the data reported here, and is thus from some kind of noise in the previous experiment.

We have successfully demonstrated that the lock-in technique can be applied to modulating temperatures of a high-T_c superconductor and that the S/N is count-rate limited up $\sim 10^8$ counts for a modulation frequency of 2 Hz, even in the presence of diffraction spikes and any other glitches in the XAFS.

Unfortunately, the technique still must be applied to a system with known, measurable changes (and measure those changes) before it can be readily believed.

Part II

Experimental studies on perovskite materials

Chapter 7

Local oxygen disorder around praseodymium in $Y_{1-x}Pr_xBa_2Cu_3O_7$

7.1 Introduction

An interesting property of $YBa_2Cu_3O_7$ (YBCO) is that one may replace yttrium with almost any rare earth and still obtain a high-T_c superconductor[46, 47, 48], isostructural with YBCO. However, there are two rare earths that do not form a high-T_c superconductor when attempts are made to substitute them onto the Y site: cerium and praseodymium[49, 50]. Attempts to substitute with Ce have not produced the YBCO structure, even in small concentrations. Praseodymium, however, substitutes readily onto the Y site, with T_c dropping monotonically with Pr concentration. Therefore, $PrBa_2Cu_3O_7$ (PBCO) is a unique material in that it has the YBCO structure, with a rare earth instead of Y, yet is not superconducting. In contrast, substitution by Gd, for example, has essentially no change in T_c or in the crystal structure[51]. There has been a large effort to explain this reduction in T_c as a new avenue in the search to explain why YBCO is superconducting in the first place. PBCO is interesting in its own right, however, as an insulating layer between layers of YBCO in multilayer films, or as a well matched substrate for epitaxial films of YBCO.

There are many related explanations for the decrease in T_c in $Y_{1-x}Pr_xBa_2Cu_3O_7$ (YBCO:Pr), mostly involving the localization of holes through valence change or magnetic pair breaking mechanisms. The earliest arguments note that Ce, Pr and Tb are the only rare earths that can exist in either a +3 or +4 valent state[50]. Since Y only exists in a +3 valent state, one explanation for the decrease in T_c with Pr concentration is that some fraction of the Pr exists in its formal +4 state, filling a hole state in the Cu-O planes and localizing it onto the Pr site. There is some experimental evidence to support this view, notably the measured magnetic susceptibility of 2.7 μ_B per Pr ion in PBCO[52, 53], which may be compared to the Pr^{3+} ion (3.58 μ_B) and the Pr^{4+} ion (2.54 μ_B). However, this result should be considered in light of some model systems that give moments significantly different than the ionic moments, such as the moment of $BaPrO_3$ (0.7 μ_B)[54], where Pr^{4+} is presumably the natural state.

Another possible mechanism for suppressing T_c in this material utilizes the fact that, except for Ce, the Pr^{3+} ion is the largest of all the rare earth +3 ions. The $4f^2$ electrons are far enough extended to hybridize with the O $2p$ electrons, and thus interfere with the conduction band[55]. In fact, crystal field measurements can be reconciled with Pr in a completely +3 state[55, 56], with broad transitions that can be attributed to hybridization between the Cu $5d$-O $2p$ states and the Pr $4f$ states[56].

X-Ray Absorption Near-Edge Structure studies (XANES) also indicate that Pr is primarily trivalent. Comparisons of the Pr L_{III}-edge of PBCO to that for PrO_2 and Pr_2O_3 indicate a valence close to +3[57], or slightly above it[58, 59]. The latter studies suggest that a small amount of Pr +4 is present; Horn *et al.* [58] give a mean valence of +3.1, while Lytle *et al.* [59] find that the valence decreases from +3.45 for YBCO:Pr 20% to +3.25 for YBCO:Pr 60% with all of the Pr^{4+} on the Cu(2) site (see Fig. 7.1 for structural notation). M-edge studies [60] and electron-energy loss spectroscopy (EELS) studies [61] also find that the Pr valence is close to +3. These same studies show that the number of holes in the CuO_2 planes does not change with Pr concentration, while normal-state Hall effect measurements [62] show a decrease in the number of mobile charge carriers with x, indicating that the holes are being localized rather than filled. Photoemission experiments also find that the Pr valence is close to +3 and that there is significant hybridization of the Pr $4f$ states with other valence states[63]. In addition, thin films of $Y_{0.5}Tb_{0.5}Ba_2Cu_3O_7$

have recently been produced, with a T_c of 92 K[64]. Such a high T_c for a 50% terbium sample brings into question the argument that the suppression of T_c arises solely because two valence states can exist.

A theory which combines many of these ideas, proposed by Fehrenbacher and Rice[5], shows that three electronic configurations are favored: a $Pr^{3+}(4f^2)$-O state, a $Pr^{4+}(4f^1)$-O state, and a $Pr^{3+}(4f^2\underline{L})$-O, where the $Pr^{3+}(4f^2\underline{L})$ indicates that the hole does not reside within the praseodymium's electronic structure; rather, the hole is in the ligand. The low-energy ligand hole is obtained via a superposition of O $2p_\pi$ orbitals with f symmetry. The most energetically favorable configuration has Pr^{3+} 60-70% of the time, with the remaining Pr-O bonds split between the other two configurations. They reason that such a mixture would be consistent with all the above measurements, since ionic Pr^{4+} would only exist 15-20% of the time, even though formally the Pr is in a +4 state 30-40% of the time.

There is also some structural evidence from neutron and x-ray diffraction for a mixed Pr valency. Diffraction results show that PBCO is isostructural with YBCO. The diffraction result for the average Pr-O nearest-neighbor distance of 2.45 Å [65, 66, 67, 68] is reasonably consistent with Pr^{3+}-O bond lengths in other Pr oxides, such as in bixbyite Pr_2O_3, which has a range of Pr-O bond lengths from 2.33 Å to 2.66 Å[69]. It has been noted, however, that both the Cu-O plane separation [66, 68] and the Pr-O(2) and Cu(2)-O(3) bond lengths[68] are more consistent with a valence in the range of +3.3-3.4, as determined by interpolating trends in these bond lengths with rare-earth ionic radius. However, this interpolation argument has at least two possible flaws. First, just because the trend with ionic radius is no longer linear for Pr does not necessarily mean Pr is in a mixed valence state. The Pr^{3+} ion is the largest ion anyone has been able to place between the Cu-O

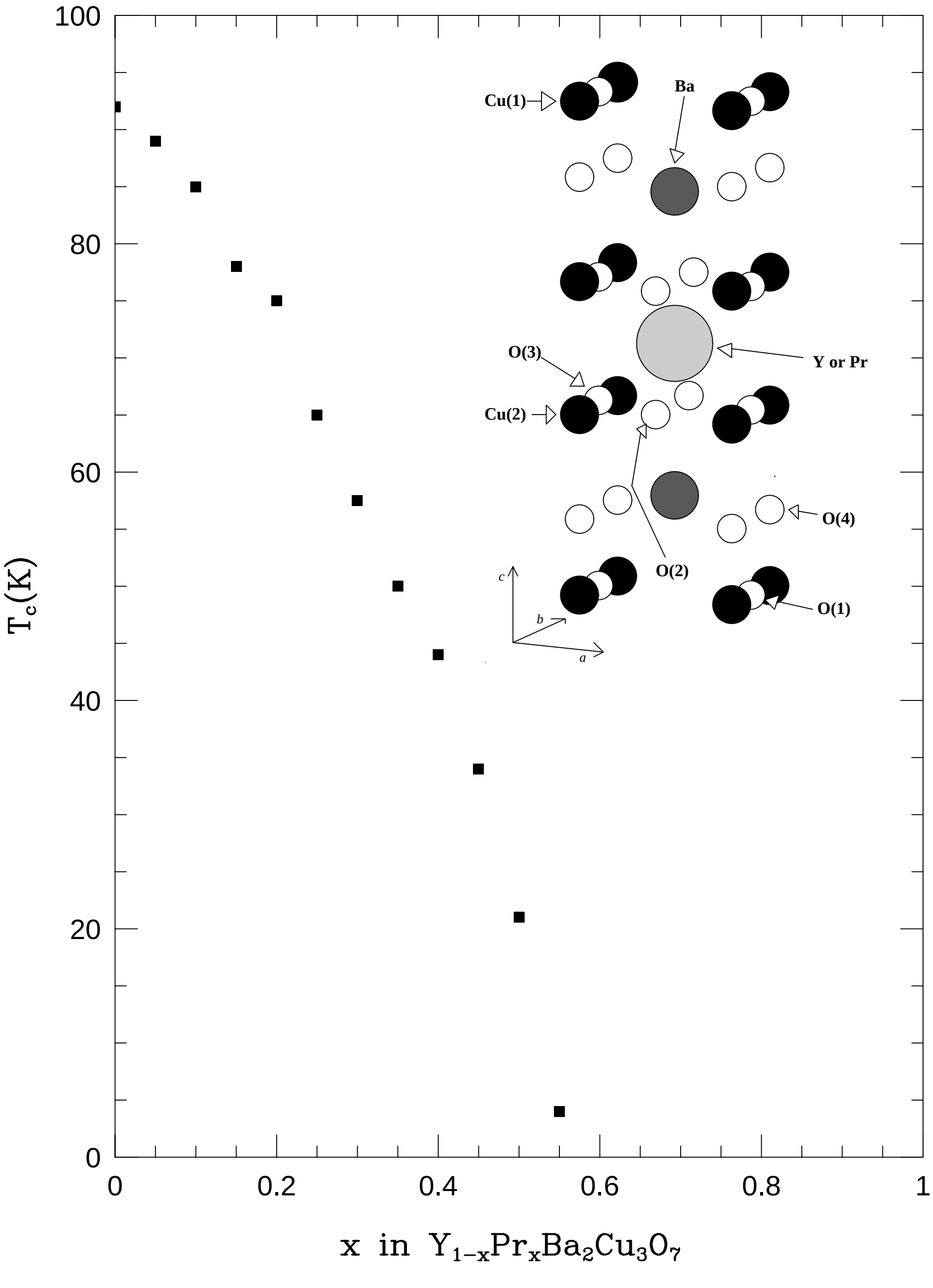

Figure 7.1: T_c vs. Pr concentration. The inset shows the structure of $YBa_2Cu_3O_7$ with the notation used in this paper.

planes in this structure, so new forces, including more oxygens bonding to the Pr than, say, Y, may be coming into play. In addition, there are several compounds that show a wide range of Pr^{3+} bond lengths, such as bixbyite Pr_2O_3. Secondly, if three Pr-O states exist, as suggested by Fehrenbacher and Rice[5], then one would expect to see two, and perhaps three, different Pr-O bond lengths; Pr^{4+}-O bonds range in length from 2.18 Å in $BaPrO_3$ to 2.32 Å in PrO_2. Therefore the three Pr-O states should have bond lengths made up of a long $Pr^{3+}(4f^2)$-O, a short $Pr^{4+}(4f^1)$-O, and a $Pr^{3+}(4f^2\underline{L})$-O (formally, Pr^{4+}-O), whose bond length should be closer to $Pr^{4+}(4f^1)$-O. Diffraction would not be sensitive to such a distribution. It will either see the dominant bond length (perhaps the $Pr^{3+}(4f^2)$-O), or an average bond length consistent with a mixed valency, depending on the degree of disorder.

Likewise, trends in the local O environment around the Pr with Pr concentration are only obtainable with large Pr concentrations. If trends exist in the concentration region where YBCO:Pr is still superconducting, that is, Pr concentrations $\leq 55\%$, diffraction may not see them. Therefore diffraction results do not rule out disorder and/or distortions of the O around the Pr. A distortion in the Pr local structure could indicate the presence of some formal or ionic Pr^{4+}, but other disorder may also exist. For instance, there is experimental evidence from x-ray diffraction to show that the Cu(2)-O(4) distance is anomalously short[67], and therefore may impede charge transfer between the planes and the chains. The length of this bond is consistent with the trend with ionic radius of Pr^{3+}[68], but it is still the shortest Cu(2)-O(4) bond measured in the YBCO-type materials. Any of these results could produce some localization of charge carriers.

Since local distortions and/or disorder in the oxygen environment around praseodymium may indicate the presence of some Pr with a formal valence of 4+, we have conducted X-Ray Absorption Fine Structure (XAFS) experiments on several concentrations of $Y_{1-x}Pr_xBa_2Cu_3O_7$, at the Cu, Y, and Pr K-edges ($E_o \simeq 9$ keV, 17 keV, and 42 keV, respectively). (A preliminary version of this work has recently appeared in the literature[70].) XAFS is ideally suited to this problem, because it can give us precise information about the local structure around the absorbing atom, including average bond distances and harmonic broadening factors. In particular, we should be able to determine exactly which site the Pr is occupying and observe changes in the XAFS compared to YBCO. By taking data at three different absorption edges, we can further constrain our results for the CuO_2 planes and get more information regarding the O(4) site.

In Sec. 7.2 we describe some details of the sample preparation and data collection. We explain our data reduction procedures and describe some visible features of the data in Sec. 7.3. Our analysis and fit results are detailed in Sec. 7.4. We discuss the implications of our results in Sec. 7.5 and give a brief conclusion of our findings in Sec. 7.6.

7.2 Samples and data collection

7.2.1 XAFS Samples

All the samples were prepared by the same procedure as described in Ref. [71]. Stoichiometric amounts of CuO, $BaCO_3$, Y_2O_3, and Pr_6O_{11} were mixed, ground, and heated at 920^{o}C in air for 20 hours. They were then reground, pressed into pellets, calcined at 940^{o}C in an oxygen atmosphere, and slowly cooled at 60^{o}C/h to room temperature. All the $Y_{1-x}Pr_xBa_2Cu_3O_{7-y}$ samples were characterized by x-ray diffraction using Cu Kα radiation. The patterns indicate that all the samples with x $\leq$ 0.6 are essentially single phase. The 100% Pr sample may have small amounts of phase impurities, but they are

Table 7.1: Sample information: a, b, and c lattice parameters for the $Y_{1-x}Pr_xBa_2Cu_3O_y$ samples.

x	a	b	c	y
0.0	3.821	3.882	11.621	6.96
0.3	3.826	3.894	11.667	6.94
0.5	3.846	3.907	11.691	6.96
1.0	3.902	3.916	11.715	6.98

too small to be seen in the XAFS (see Sec. 7.4). Oxygen content was analyzed by an improved gaseous volumetric technique and found to be within the range of 6.95±0.02 for all samples. In all the compounds T_c was determined by a standard four-probe method. Superconducting phase purity was checked using an AC mutual inductance bridge. Only one step was observed for all superconducting samples. Fig. 7.1 shows T_c as a function of Pr concentration and Table 7.1 gives the lattice parameters and the oxygen content measurements for these samples.

XAFS scans were performed on the 0, 30, 50, and 100% Pr samples at about 80 K for the Pr K-edge and about 50 K for the Cu and Y K-edges. To prepare the samples for these transmission experiments, we reground the pellets and sifted the powder through a 30 μm filter onto pieces of scotch tape. The tape was then cut and stacked into multiple layers to obtain samples of thickness, t, such that $\mu t \simeq 1$ at the absorption edge, where μ is the absorption coefficient. All XAFS experiments were performed at SSRL on beamlines 7-3 and 10-2. Measurements of the incident and transmitted intensities were made with gas-ionization chambers. Si (111) monochromator crystals were used for the Cu and Y K-edge experiments, while Si (400) crystals were required for the Pr K-edge.

7.3 General Features of the data

7.3.1 Standard reduction and comparison of different absorption edges

Y, Pr, and Cu K-edge data for $\chi(k) = (\mu - \mu_o)/\mu_o$ show XAFS oscillations beyond 16 $Å^{-1}$ for all K-edges. Fig. 7.2 shows kχ(k) for all three K-edges for $Y_{0.5}Pr_{0.5}Ba_2Cu_3O_7$. The "free atom absorption" μ_o is determined in the usual way [15] by fitting a spline function or a polynomial through the data above the absorption edge. The photoelectron wave vector k is given by k= $\sqrt{(2m_e/\hbar^2)(E - E_o)}$, where E_o is the K-edge threshold energy. This procedure was modified somewhat for the Pr K-edge data, as detailed in part B of this section.

The most striking difference between the Y and the Pr K-edge XAFS in Fig. 7.2 is the overall drop in amplitude of the Pr K-edge XAFS, particularly in the low k part of the spectrum. The amplitudes of the high-k XAFS are similar. The Cu K-edge XAFS are comparable to data we have previously obtained on YBCO.

The Fourier transform (FT) of the data yields peaks in r-space corresponding to different radial distances from the excited atom. The peaks in the FT of kχ(k) are shifted in distance due to phase shifts at the scattering and absorbing atoms, and must be compared to standard compound XAFS to obtain the bond lengths. In the figures showing FT data, the shifted position of the peaks are given by vertical lines. In Fig. 7.3a and 7.3b, the FT of kχ(k) for data collected on PBCO at the Pr K-edge and for CeO_2 at the Ce K-edge are compared. FT's for several concentrations of Pr in YBCO:Pr for the Y, Pr, and Cu K-edges are presented in Fig. 7.4, 7.5, and 7.6.

By comparing the FT of the XAFS from the various edges, we can quickly ascertain

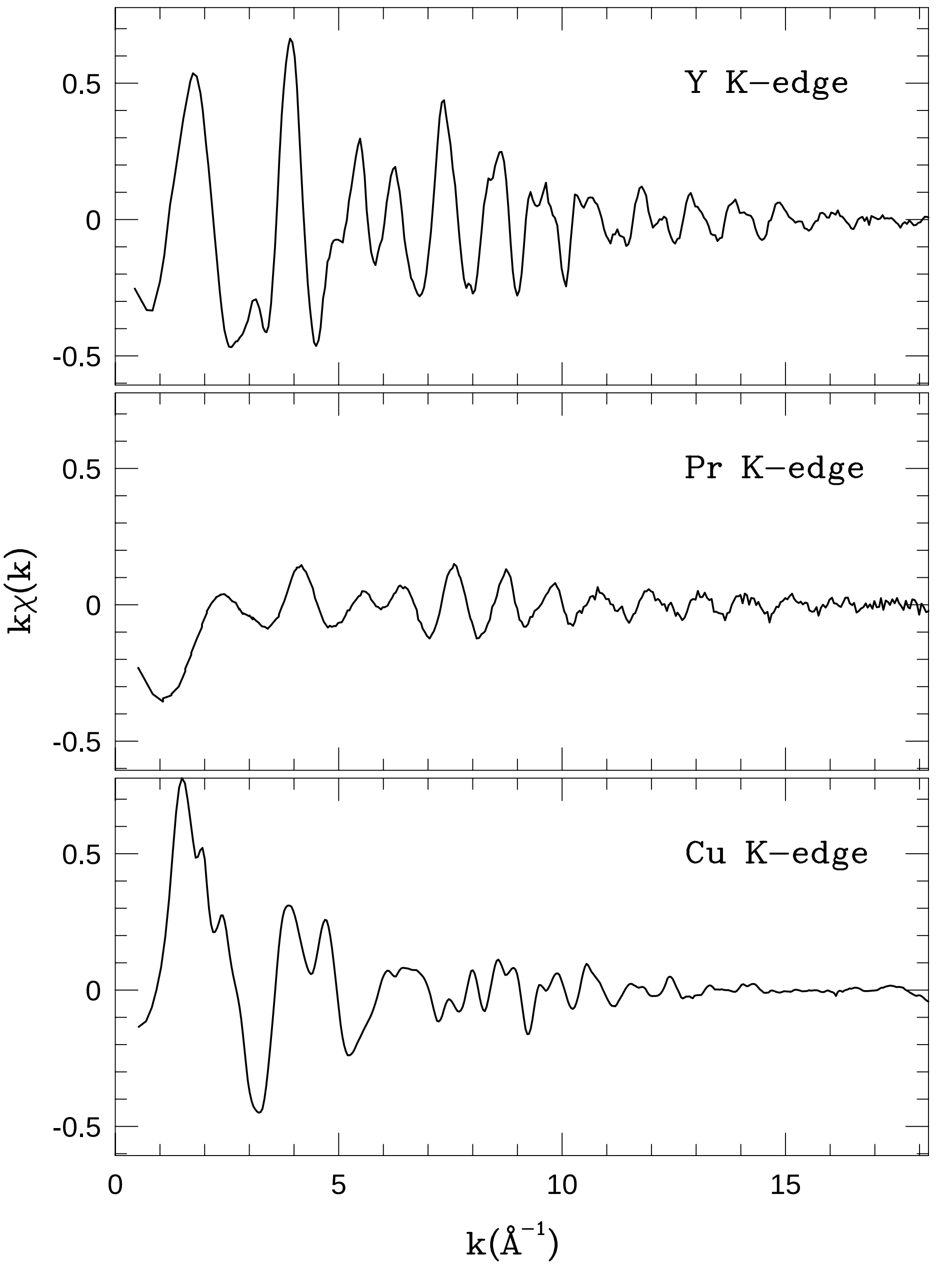

Figure 7.2: kχ(k) for the 50% Pr sample from the Y, Pr and Cu K-edges (at 17080 eV, 41991 eV, and 8979 eV, respectively).

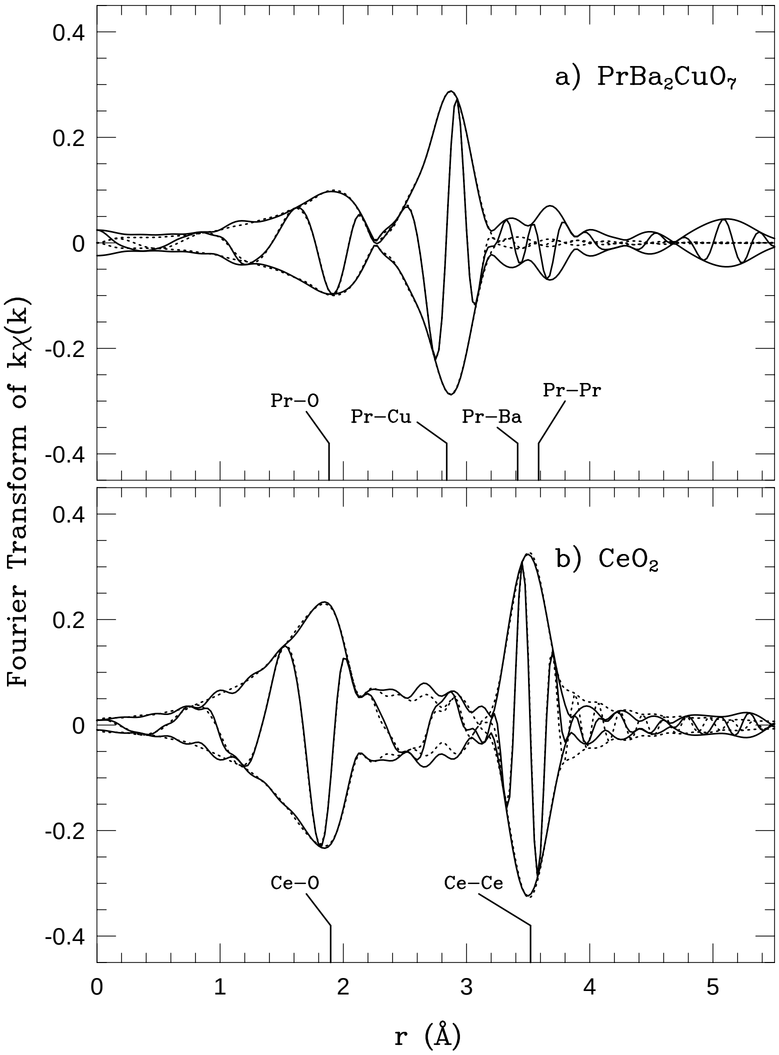

Figure 7.3: Fourier Transforms of kχ(k) for (a) $PrBa_2Cu_3O_7$ and (b) CeO_2, together with fits to the first two major peaks (dotted). The outer envelope is the magnitude of the FT, while the modulating curve is the real part. All the fits discussed in the text are of similar quality to the PBCO fit shown here. The first peak in both cases is an eight-fold coordinated oxygen peak. Single pair peak positions are approximately given by vertical lines that meet the x-axis. These peak positions are shifted from the actual positions by phase shifts at the absorbing and backscattering atoms. Both transforms are from 3.5-17.0 $Å^{-1}$, with a 0.3 $Å^{-1}$ gaussian window.

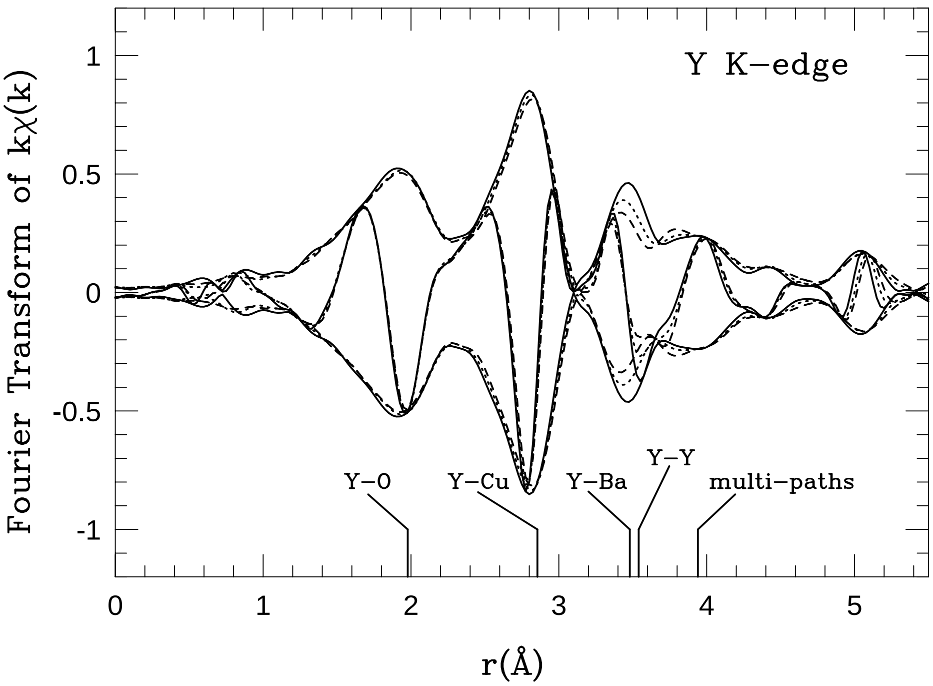

Figure 7.4: Fourier Transform of $k\chi(k)$ for Y K-edge data for 0% (solid), 30% (dotted), and 50% (dash) Pr concentrations. The only dramatic changes occur in the Y-Ba, Y-Y, Y-Pr region. These transforms are taken from 3.5-15.5 Å^{-1}, with a 0.1 Å^{-1} gaussian window.

the dominant substitution site for Pr. From the solid line in Fig. 7.3a (PBCO, Pr K-edge) and the solid line in Fig. 7.4 (YBCO, Y K-edge) we can see by the location of the first two peaks that the oxygen (first peak) and copper (second peak) environment around Pr in PBCO is very similar to that around Y in YBCO. In contrast, a simulation using FEFF5 [72] of the Ba K-edge XAFS in YBCO puts the oxygen and copper peaks at very different positions than observed in the Pr K-edge data. Similarly, the Cu K-edge data for YBCO (Fig. 7.6) also has a very different environment. This indicates that most of the Pr substitutes at the Y site.

We can also compare the Pr K-edge XAFS for the first Pr-O peak to the Ce K-edge XAFS for the first Ce-O peak in CeO_2. Both sites should be 8-fold coordinated, and since Ce and Pr are neighbors in the periodic table, their XAFS amplitudes and phases should

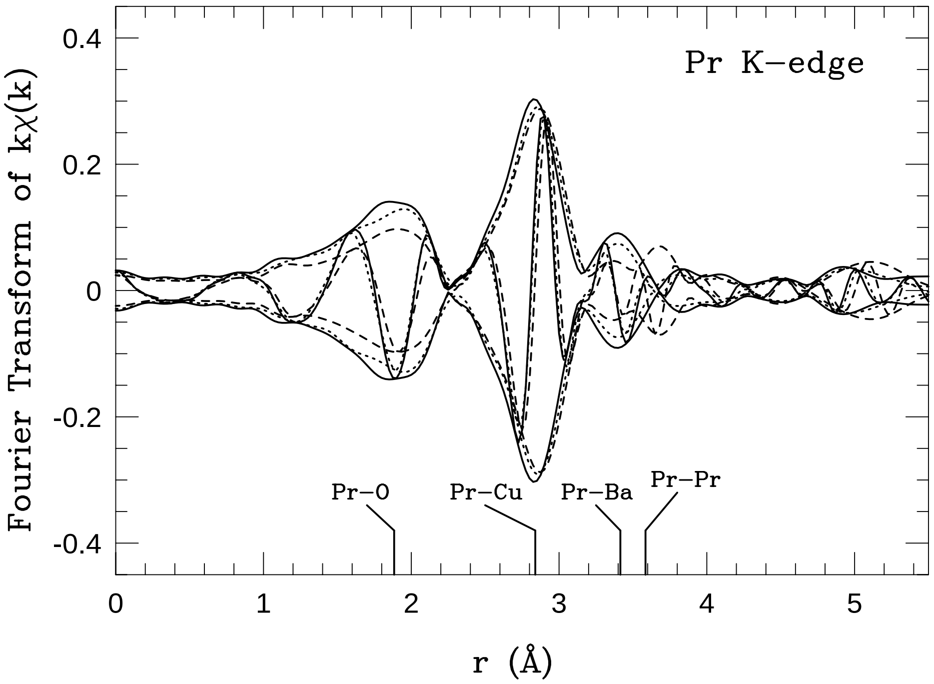

Figure 7.5: Fourier Transforms of kχ(k) for Pr K-edge data for 30% (solid), 50% (dotted), and 100% (dash) Pr concentrations. Notice the decrease of the first peak with Pr concentration. This decrease is most likely due to a combination of the relative amplitudes of two Pr-O distances and additional disorder in the shorter bond. The second peak is the Pr-Cu peak. It shows relatively little change with Pr concentration, indicating that the Pr is well ordered with respect to the Cu, and thus to the unit cell. The peaks in the 3-4 Å range are due to a mix of Pr-Y, Pr-Pr and Pr-Ba. This region is difficult to fit accurately because the Y and Pr backscattering amplitudes are similar, but π out of phase. The FT ranges are from 3.5-17.0 Å^{-1}, with a 0.3 Å^{-1} gaussian window.

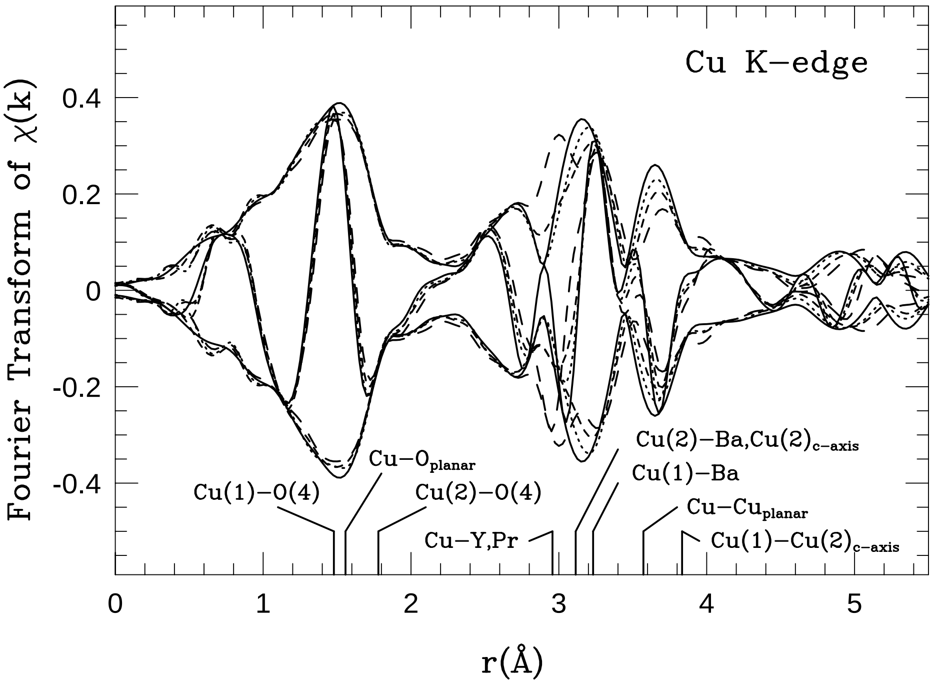

Figure 7.6: Fourier Transforms of kχ(k) for Cu K-edge data for 0% (solid), 30% (dotted), 50% (short dashed), and 100% (long dashed) Pr concentrations. The first Cu-O peak decreases with increasing Pr concentration by about 10% in PBCO. The Cu-Y, Cu-Pr, Cu-Ba region also changes dramatically, due to the changing phase shifts between these peaks; see text for further discussion. These transforms are taken from 3.0-15.8 Å^{-1}, with a 0.1 Å^{-1} gaussian window.

be comparable. However, the FT of kχ(k) shows a 60% drop in amplitude in the Pr-O peak in the 100% Pr sample when compared to the Ce-O peak (Fig. 7.3). In fact, the Pr-O peak amplitude decreases with increasing concentration (Fig. 7.5). The Pr-Cu peak in PBCO shows little change with concentration, suggesting that the praseodymium is occupying a well ordered site in the unit cell while the oxygen is not.

Changes in the oxygen environment around the yttrium in the Y K-edge XAFS, if any, are below the resolution of the experiment (Fig. 7.4). Changes in the further neighbor peaks are only evident in the Y-Ba, Y-Y, Y-Pr regime where the double hump at 3.6 Å becomes less lopsided toward the lower side with increasing Pr concentration. There is no visible changes in the Y-Cu peak.

The Cu K-edge XAFS of PBCO show a 10% reduction in the oxygen peak amplitude compared to YBCO indicating that some disorder in the oxygen environment exists (Fig. 7.6). Changes in the Cu-Ba, Cu-Y, Cu-Pr multi-peak (between 2.6 Å and 3.4 Å) are complicated, with the large peak at 3.15 Å breaking into two humps at 3.0 Å and 3.3 Å. The peak due to the $[\mathrm{Cu(1)\text{-}Cu(2)}]_{c-axis}$ and the ab plane Cu-Cu bonds (centered at about 3.65 Å) decreases monotonically with Pr concentration. This multi-peak includes the forward scattering due to the co-linear or nearly co-linear oxygens along most of these copper-copper paths. Since the forward scattering amplitude is strongly dependent on small deviations from co-linearity, the changes in this peak probably indicate small displacements of the O atoms.

7.3.2 Background features in high-energy K-edge XAFS

A preliminary FT of the Pr K-edge data which uses a simple spline or polynomial for μ_o indicates an anomalous hump near 1 Å. By fitting the data above 6 $Å^{-1}$ to the Pr-O and Pr-Cu peaks, and then subtracting the extrapolated fit from the original data, clear features in μ_o(E) emerge which cannot be reconciled as an XAFS signal (Fig. 7.7). The position of the feature roughly 115 eV above the absorption edge is consistent with a multielectron excitation, as estimated from the Z+1 model, i.e., with the $N_{IV,V}$ transition of Nd. As pointed out by Holland *et al.* [25], a Ramsauer-Townsend-like effect can also lead to significant structure in the atomic background absorption. Such background features arise when the wavelength of the photoelectron is comparable to the dimension of an "embedded" absorbing atom in a solid and are essentially an XAFS of atomic origin. The effect appears to be larger in atoms of higher atomic number. Calculations by J. Rehr (private communication) show that this structure can occur at energies comparable to those of possible multielectron excitations. The background structure for Pr K-edge data is indeed much larger than features we have seen in previous work[27]. We have removed the background structure using the iterative procedure discussed in Ref. [27]. Similar features were removed from the Ce K-edge data for the standard compound CeO_2. Our work on these background features will be the subject of a future paper.

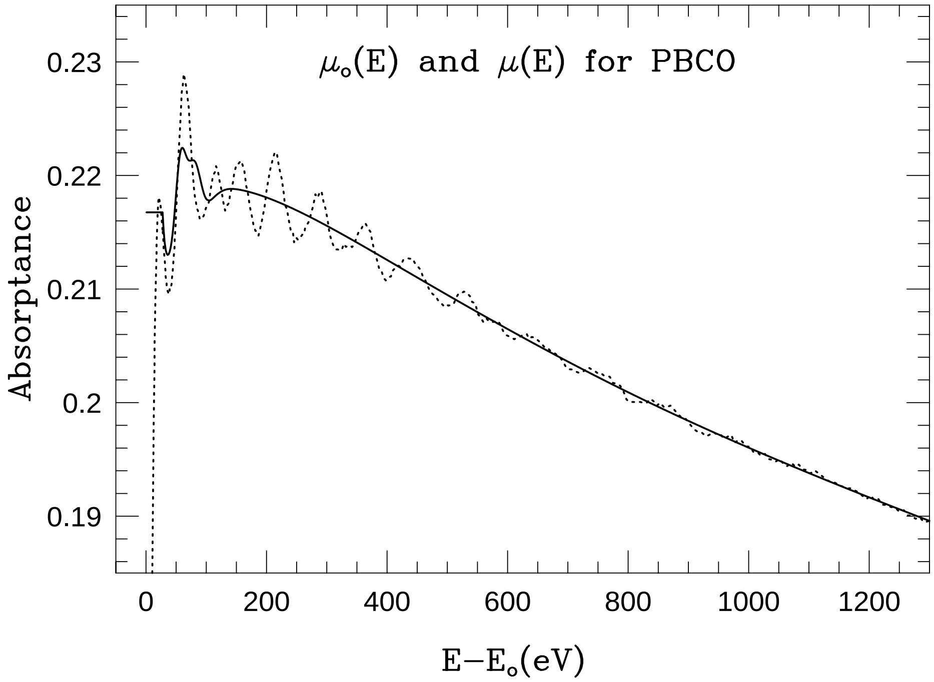

Figure 7.7: "Free-atom absorption" μ_o (solid) and total absorption μ (dotted) coefficients times sample thickness, t, as a function of energy above the K-edge. μ_ot was determined by an iterative procedure[27].

7.4 Detailed analysis and fit results

7.4.1 Fitting procedures and constraints

All fits to the XAFS data are carried out in r-space on the FT of kχ(k). We typically choose an appropriate range in k for the transform, and only fit it in some desired range in r. In the r-space fitting procedure, we vary the XAFS from standard compounds in amplitude, a Debye-Waller-like broadening σ, position, and the K-edge threshold energy E_o to obtain a good fit. We have developed experimental standards for many pairs of atoms. For pairs which we have no experimental standards, the theoretical standards calculated by FEFF5[72] were used. Fits to the Pr K-edge data used the theoretical standards, while Cu K-edge data were fit with experimental standards. Since we did not obtain standard compounds containing Pr, we evaluated the quality of the theoretical standards for Pr by comparing the Ce-O standard generated by FEFF5 to experimental data obtained from CeO_2, with good agreement for the Ce-O peak (Fig. 7.3b). The non-linear fitting routine minimizes a fit parameter, $C^2 = \sum |FT(k\chi(k)) - fit|^2 / < |FT(k\chi(k))|^2 >$, which is roughly proportional to the statistical χ^2. Each fit can include some constraints, such as setting the number of neighbors in one peak equal to some fraction of the number of neighbors in another peak. Such constraints are necessary to restrict the number of independent parameters[73] and can be used to test a model, or to control correlations between fit parameters. For instance, correlations between amplitude and broadening factors can be controlled by, say, constraining the sum of the number of neighbors for two peaks to be some fixed value. The constraints are generally self-consistent, i.e., various atomic pair distances and number of neighbors are related and must have the same results for measurements at different K-edges.

7.4.2 Determining substitution site of Pr

A fit to FEFF5 theoretical XAFS standards that includes a mix of Pr at the Y site and at the Ba site indicates that, at most, the Pr exists on the Ba site 8% of the time. This non-zero result could only be obtained if the fit allowed the energy of the Pr K-edge (E_o) to be significantly different (10 eV) for Pr in the Y site and Pr in the Ba site. Such a small concentration of Pr at the Ba site in these fits is consistent with all Pr substituting onto the Y site. More information regarding this issue from the other K-edges is difficult to obtain, because the backscattering amplitudes of both the Pr (Z=59) and Ba (Z=56) atoms are very similar.

A similar fit that allows some Pr to reside on the Cu(2) site is not as simple to interpret. For this discussion, we will refer to Pr at the Cu(2) site as $Pr_{Cu(2)}$, and Pr at the Y site as Pr_Y. We can obtain a fit to the Pr K-edge data that includes 20% of the Pr residing on the Cu(2) site, with a lengthening of the $Pr_{Cu(2)}$-O bonds by 0.25 Å and of the $Pr_{Cu(2)}$-Pr_Y bonds by 0.13 Å. Such a distortion in the oxygen environment is consistent with both the Pr K-edge and the Cu K-edge data. However, a distortion in the $Pr_{Cu(2)}$-Pr_Y bond should effect how the Pr_Y sits in the unit cell, and should thus be reflected in the Pr_Y-Cu bond. This effect should be large even for small ($\sim$ 20%) $Pr_{Cu(2)}$ concentrations, because the shift in the $Pr_{Cu(2)}$-Pr_Y bond length is large enough to cause nearly a complete cancellation of the distorted Pr_Y-Cu peaks. The data (Fig. 7.5) and the fits (see Sec. 7.4.4) show very little change in the Pr-Cu peak. Therefore, these data are not consistent with Pr at the Cu(2) site within the amplitude limits of XAFS spectra ($\sim$ 10%), for all Pr concentrations measured.

7.4.3 Y K-edge fits

Fits to the Y K-edge data were performed, without any constraints, on the 0, 30, and 50% Pr samples. Results for the oxygen and copper peaks are in Table 7.2. Further peaks, such as the Y-Ba, Y-Pr, and the Y-Y peak were fit but are not reported, because they are all at similar distances, and the Y-Ba, Y-Pr peaks are almost exactly out of phase with the Y-Y peak. This situation allows changes in amplitude to be mimicked by changes in position, and thus does not give reliable results.

The number of oxygen neighbors shown in Table 7.2 changes very little with concentration (about 5% up to 50% Pr), while the copper peak shows a slight increase. Such

Table 7.2: Y K-edge fit results. These fits include further peaks than the Y-Cu peak, but these peaks are plagued by an interference effect when Pr is present (see Sec. 7.4.4). Y-Cu amplitudes are consistently larger than those calculated by FEFF5 by nealy 25%. Since we do not have data for a similar standard pair, we have normalized the Y-Cu number of neighbors to the YBCO result. The number of Y-O nbrs is not normalized. The fits are from 1.0-3.1 Å in R, and from 3.5-17 $Å^{-1}$ in the wave vector k. Each bond is expected to be comprised of 8 neighbors. The errors are ± 0.01 Å in R, and $\pm 10\%$ in both σ and number of neighbors for all XAFS fits reported in this work, unless otherwise noted.

	Y-O			Y-Cu		
x	R(Å)	nbrs	σ(Å)	R(Å)	nbrs	σ(Å)
0.0	2.41	7.3	0.058	3.21	8.0	0.058
0.3	2.41	7.1	0.056	3.22	8.6	0.060
0.5	2.41	6.9	0.057	3.23	8.6	0.060

small changes are not within the resolution of this experiment, and the data are therefore consistent with no change in the number of O atoms surrounding Y. The Y-O distance remains constant. The Y-Cu distance does increase monotonically with Pr concentration, as one would expect from the diffraction results (Table 7.1).

7.4.4 Pr K-edge fits to a variety of models

Fits to the Pr K-edge XAFS spectra were performed with and without a variety of constraining models and initial conditions. Each model has an associated C^2 value for its fit, which should give the reader a feel for the range of models that may give plausible results. Table 7.3 gives fits to the 100% Pr sample with a variety of constraints imposed on the fits that simulate different models. None of the models constrain the Pr-Cu peak, and none of the fits to these models show any significant differences in this peak.

Model 1 assumes a single Pr-O bond, with no constraints, and gives a good quality of fit. This fit shows an oxygen deficiency around Pr, with only 4.8 of the expected 8 oxygens. Since this result is inconsistent with the fit results of the Y K-edge (Sec. 7.4.3), the Cu

Table 7.3: Fit results on $PrBa_2Cu_3O_7$ to a variety of models. Fitting procedures are detailed in the text. C^2 is the fitting parameter, and is approximately proportional to the statistical χ^2, as described in the text. The r-space fits are from 1.0 - 3.0 Å in R, and the FT from 3.5-17.0 Å^{-1} in wave vector k. The number of Pr-O neighbors is normalized to the CeO_2 result. No normalization has been applied to the Pr-Cu peak. Model 1 only allows for one Pr-O distance, with no constraints on the fit parameters. Model 2 also only allows for a single Pr-O bond, but constrains the amplitude to be 8, as is expected from the known crystal structure. Model 3 allows for two Pr-O bonds (Pr-O_{short} and Pr-O_{long}, as do all the subsequent models) with no further constraints. Model 4 constrains the total number of Pr-O bonds to 8. Model 5 constrains the number of Pr-O bonds to 8 and holds their bond lengths equal. Model 6 constrains the total number of Pr-O bonds to 8 and holds their broadening factors (σ) equal.

	Pr-O_{short}			Pr-O_{long}			Pr-Cu			
model	R(Å)	nbrs	σ(Å)	R(Å)	nbrs	σ(Å)	R(Å)	nbrs	σ(Å)	C^2
1				2.46	4.8	0.066	3.27	7.8	0.049	0.148
2				2.47	8.0	0.116	3.27	7.6	0.047	1.513
3	2.30	1.0	0.135	2.46	4.7	0.063	3.27	7.9	0.048	0.132
4	2.27	2.9	0.168	2.45	5.1	0.067	3.27	7.7	0.048	0.174
5	2.46	3.5	0.287	2.46	4.5	0.064	3.27	7.8	0.048	0.160
6	2.15	1.2	0.084	2.44	6.8	0.084	3.27	7.7	0.048	0.300

K-edge (Sec. 7.4.5) and the volumetric measurements of the oxygen concentration in these samples (Table 7.1), we constrained the next fit to give 8 oxygens. Model 2, which has one Pr-O distance and does not allow for an oxygen deficiency, yields a poor fit with a substantially larger σ and an increase in the goodness-of-fit parameter (C^2) by more than an order of magnitude. It is therefore highly unlikely that simple harmonic disorder of the Pr-O bond can explain the reduction in the Pr-O peak in the FT of kχ(k).

Next we considered several models that allow the first peak to be composed of two different Pr-O harmonic distributions. Since for K-edge data any shift due to differences in valence should be small, all of these models constrain any E_o shifts in the Pr-O bonds to be the same. Model 3 allows for a double Pr-O bond, with no further constraints. This fit has the best C^2 of any of the models. It indicates a total number of oxygens which is still low (5.7). However, a fit to model 4, which constrains the total number of nearest-neighbor oxygens to sum to 8, gives an C^2 which is only 30% higher.

Two other models were tested to see if the fits in models 3 and 4 can be distinguished from similar models. All these fits have a good quality of fit parameter, but shift certain parameters outside a reasonable range. A fit which constrains the length of the two bonds to be equal and the total number of oxygens to be 8 (model 5), but allows for different σ's gives a very large σ of 0.287 Å for the short Pr-O bond, with 3.5 O neighbors (roughly 36% of the O). However, a peak this broad has a tiny XAFS amplitude, and therefore this fit is essentially the same as the single Pr-O peak fit in model 1. Consequently we do not consider this possibility further. Constraining the σ's to be equal (rather than the bond lengths), with 8 total oxygen neighbors (model 6) gives a fit with a short Pr-O bond length of 2.15 Å and an increase in C^2 by less than a factor of two over model 4. In this fit, only 15% of the Pr-O bonds are short. Such a short bond length is not unreasonable, given that the short Pr-O bond in $BaPrO_3$ is 2.18 Å[69], although Pr is only 6-fold coordinated with respect to oxygen in that compound. Models 3, 4, and 6 all indicate that the radial distribution of Pr-O bond lengths is not a symmetric distribution; the major weight is near 2.45 Å but there is clearly some weight in a broad peak centered near $2.27^{+0.03}_{-0.12}$ Å.

Fits that allow for three Pr-O distributions (as suggested by Ref. [5]) are not conclusive, because the number of parameters required for such a fit exceeds the maximum number of parameters allowed by our fitting range[73]. However, the two peak fits described above giving large σ's for the shorter Pr-O distribution may mimic a situation with three distances.

The peaks that allow for two Pr-O distributions give the most consistent results. Therefore, fits that allow the Pr-O peak to be composed of two different harmonic distribu-

Table 7.4: Pr K-edge fit results to $Y_{1-x}Pr_xBa_2Cu_3O_7$ as in model 4 in Table 7.3.

	Pr-O_{short}			Pr-O_{long}			Pr-Cu		
x	R(Å)	nbrs	σ(Å)	R(Å)	nbrs	σ(Å)	R(Å)	nbrs	σ(Å)
0.3	2.25	1.7	0.128	2.43	6.3	0.056	3.25	7.5	0.046
0.5	2.29	2.7	0.115	2.43	5.3	0.053	3.25	7.4	0.047
1.0	2.27	2.9	0.168	2.45	5.1	0.067	3.27	7.7	0.048

tions (models 3 through 6) suggest 15-40% of the nearest-neighbor Pr-O bonds are either disordered and/or shifted ($\simeq$ 0.18 Å) compared to a more populated, ordered site.

Table 7.4 summarizes the results of a two-peak fit with the constraint that there be 8 oxygens in the first peak for all measured Pr concentrations. Debye-Waller factors for the disordered site increase linearly with Pr concentration, and are as much as 150% higher than for the "normal" site in PBCO. The fits show no appreciable change in the Cu environment around praseodymium with concentration, apart from the expected lengthening of the Pr-Cu bond due to the slight expansion of the lattice (Table 7.1). The number of copper neighbors around the praseodymium remains the same for the 100% Pr sample compared to the other Pr concentration samples. Therefore, we can conclude that the effect of the small fraction of other phases in the PBCO sample [71] on the XAFS is below the resolution of the experiment.

7.4.5 Cu K-edge fits

Cu K-edge fits to the 0% and 100% Pr samples were also carried out. Fits to partial concentrations of Pr are difficult to obtain because of the known distortions caused by the two sub-lattices. Several constraints were placed on the fits to maintain certain symmetries in the system. For instance, the Cu(1)-O(4) distance plus the Cu(2)-O(4) distance is constrained to equal the Cu(1)-Cu(2) distance obtained from diffraction[67].

The Ba position is constrained to be in the center of the ab-plane of the unit cell, while the Y or Pr position is constrained to be in the middle of all planes in the unit cell, consistent with the Cu(2)-Y and the Cu(2)-Cu(2) (c-axis) bond lengths. Other constraints on the number of neighbors have been imposed to maintain the number of atoms at certain sites while still allowing for overall shifts in amplitude. The proximity of the Cu(1)-O(1), Cu(2)-O(2), and Cu(2)-O(3) peaks makes an accurate determination of their relative amplitudes difficult. Consequently, measurements of changes in their relative amplitudes is beyond the resolution of our fits. We have treated the Cu(1)-O(1), Cu(2)-O(2), and the Cu(2)-O(3) as one peak (the Cu-O_{planar} peak), and constrained the relative amplitudes of this peak to the Cu(1)-O(4) and the Cu(2)-O(4) peaks.

The fits to the Cu K-edge data are summarized in Table 7.5. Fit parameters for YBCO are typical of fits we have obtained in previous work. There are several differences between the YBCO and the PBCO results. Bond length changes are, of course, expected, and will be dealt with in some detail in the next section. Number of neighbor values are 15% different for the combined Ba and Pr peak compared to YBCO, which is usually considered to be outside the expected error (10%) for XAFS amplitudes. However, the amplitude of this combined peak is very sensitive to the individual positions of the Ba and the Pr, as well as to the position of the Cu(2)-Cu(2)$_{c-axis}$ peak, and are therefore not very reliable. The broadening factors are slightly larger for the planar oxygens and the Cu(1)-O(4) bond in PBCO, as are the σ's for the Ba and Pr peaks. The Cu(2)-O(4) bond in PBCO is much narrower than in the YBCO. Again, the σ's for the Ba and Pr peak suffer from the same problems as their amplitudes, but the change in σ for the oxygen peaks is probably real.

Table 7.5: Cu K-edge fit results to $YBa_2Cu_3O_7$ (YBCO) and $PrBa_2Cu_3O_7$ (PBCO). The "pseudo-YBCO" is calculated from the lattice parameters of PBCO[67] and the relative atomic positions in YBCO[74]. The last column shows the differences between the XAFS results and the diffraction results for PBCO. The samples used in the diffraction measurements for PBCO had a mean oxygen content of $\simeq 6.77$. The PBCO XAFS results agree with the diffraction results, within calculated errors, except for the Cu(1)-O(4) and the Cu(2)-O(4) bond lengths, as discussed in Sec. 7.5. The calculated errors are the same as discussed in Table 7.2 except for the Cu-Ba,Pr neighbors in PBCO ($\pm$ 1.5), and the positions of the Cu-Ba, Pr and Y peaks for both PBCO ($\pm$ 0.03 Å) and YBCO ($\pm$ 0.02 Å).

	expected	PBCO XAFS			YBCO XAFS		
bond	nbrs	R(Å)	nbrs	σ(Å)	R(Å)	nbrs	σ(Å)
Cu(1)-O(4)	2	1.88	2.4	0.082	1.85	2.3	0.069
Cu-O_{planar}	10	1.98	11.8	0.082	1.94	11.7	0.069
Cu(2)-O(4)	2	2.22	2.4	0.056	2.27	2.3	0.110
Cu(2)-Ba	8	3.36	9.5	0.056	3.37	7.6	0.035
Cu(1)-Ba	8	3.47	9.5	0.056	3.49	7.6	0.035
Cu(2)-Y,Pr	8	3.23	9.5	0.051	3.21	7.6	0.051

	pseudo-YBCO	PBCO diffrac. [67]	XAFS-diffrac.
bond	R(Å)	R(Å)	R(Å)
Cu(1)-O(4)	1.856	1.849	+0.031
Cu-O_{planar}	1.965	1.965	+0.015
Cu(2)-O(4)	2.311	2.254	−0.032
Cu(2)-Ba	3.408	3.388	−0.018
Cu(1)-Ba	3.499	3.482	−0.012
Cu(2)-Y,Pr	3.232	3.265	−0.025

7.5 Discussion

7.5.1 Consistency between various K-edge data

Since each absorption edge gives us information about the oxygen environment within YBCO:Pr, we can constrain our results to give a consistent picture. Y K-edge data show little if any change in the structure of YBCO:Pr up to 50% Pr, except (possibly) in the expected lengthening of the Y-Cu bond. Even this expansion of the Y-Cu distance is at the edge of the accuracy of this experiment. These data therefore show that up to 50% Pr, the oxygen and copper environment around yttrium in YBCO: Pr is essentially the same as in pure YBCO. More specifically, there is little evidence of a loss of oxygens or of disorder in the oxygen or copper environment.

The Pr K-edge data and fit results indicate that either there are missing oxygens in the Cu-O planes or that there is a large amount of disorder and/or distortion in these planes. The former is inconsistent both with the measured oxygen content and with the number of neighbors for the Cu-O and the Y-O peaks in the XAFS data, and is therefore ruled out. The data is best fit by two Pr-O distributions, separated in pure PBCO by about 0.18 Å, with one distribution less populated and more disordered than the other.

The Cu K-edge data is more complicated because of the two copper sites. Nevertheless, the oxygen environment as seen from the coppers should be consistent with (and therefore can help constrain) the Pr K-edge results. The fit results to the oxygen peaks show essentially no change in the number of nearest-neighbors, but indicate a broadening in the Cu-O_{planar} peak consistent with the 10% decrease in the peak height. If the Pr-O distortion is completely radial, then a shortening of 0.18 Å would correspond to only a

0.04 Å lengthening of ~30% of the Cu(2)-O(2,3) bonds, which is not resolvable in the fits. However, such a distortion will contribute to a broadening of the Cu- O_{planar} peak, and therefore the measured broadening is consistent with the proposed radial distortion in the Pr-O bond. The small change in the number of Y-O neighbors (which can also be modeled as a slight increase in σ) is also consistent with a radial distortion in the Pr-O bonds.

7.5.2 On the question of valence

The fit results to the first oxygen peak from all three edges are consistent with a distortion of the Pr-O bond in the radial direction of approximately 0.18 Å. This distortion may be due simply to a hybridization of the O $2p$ and Pr $4f$ electrons. However, the magnitude of the shift is very consistent with some Pr^{4+}; the best fit gives a Pr-O_{short} bond length (2.27 Å) which is close to the nearest-neighbor bond length in 8-fold coordinated PrO_2. By constraining the broadening factors, we can obtain a much shorter bond length (2.15 Å) which is more consistent with 6-fold coordinated $BaPrO_3$. The comparison to the 8-fold coordinated PrO_2 makes the most sense, since Pr in PBCO is 8-fold coordinated, although it is possible that not all the oxygens participate in Pr-O bonds.

If we assign all of the short Pr-O bond lengths to the formal Pr^{4+} state, our fit results indicate that the Pr is in that state 15-40% of the time, corresponding to a formal valence of $+3.33^{+0.07}_{-0.18}$. Such an assignment is reasonable for the shortest measured Pr-O bond length, but if the bond length is closer to ~2.3 Å, then some could still include Pr^{3+}, as in bixbyite Pr_2O_3. Therefore, the upper limit on the valence range may be too high. Likewise, the lower limit was obtained by forcing the broadening factor of the short bond to be much lower than in the best fit, which may not be reasonable.

The possible disorder in the shorter Pr-O bond could cause localization of charge carriers, and could be a byproduct of a $4f$-$2p$ hybridization. On the other hand, since the disorder is greatest for the PBCO sample, the disorder could be due to the less common Pr^{4+}-Pr^{4+} combination, which will probably have different Pr-O bond lengths than either the Pr^{3+}-Pr^{3+} or the Pr^{3+}-Pr^{4+} combinations.

Our measured dominant Pr-O distance of 2.45$\pm$0.01 Å is in excellent agreement with diffraction results[65, 66, 67, 68] that give a mean Pr-O distance of 2.4539$\pm$0.0038 Å. We see no evidence of a longer distance ($\simeq$ 2.5 Å) as suggested by the Pr-O bond length trend with ionic radius[68]. Fits that include such a peak invariably shift the peak back to the values we report. Therefore, we must conclude that the discrepancy of this bond length with ionic radius is not directly due to a mixed valency. Indeed, given the existence of a short Pr-O bond, the long Pr-O bond seems to be entirely $Pr^{3+}(4f^2)$-O.

The range for the valence is in approximate agreement with the electronic studies mentioned in Sec. 7.1 that give the valence of Pr to be close to 3+. However our results clearly suggest a higher formal valence than 3.0, as was found in Pr L-edge studies of Horn *et al.* (3.1+ for PBCO)[58] and Lytle *et al.* (3.45+ for 20% Pr and 3.25+ for 60% Pr)[59]. In addition, our structural results show that the number of short Pr-O bonds, that is, formal Pr^{4+}, increases with increasing Pr concentration, and that any Pr^{4+} that may be present resides on the Y site. Both of these results are in contrast to the Lytle *et al.* results.

Our result is in striking agreement with the 4+ / hybridization model put forth by Fehrenbacher and Rice[5], which predicts that the Pr^{3+} state will exist 60-70% of the time. A ligand hole localized on the Pr-O(2)/O(3) bond would remove a hole from the conduction band and yield a formal Pr^{4+} site. The resulting Pr^{4+}-O bond length would likely be significantly shorter than the Pr^{3+}-O bond, based on the observed bond lengths in other materials. Although we cannot give a precise estimate of the number of short bonds present, our results are consistent with their prediction.

7.5.3 On the question of the relative position of O(4)

The Cu K-edge data for PBCO are consistent with the diffraction results of Lowe-Ma and Vanderah [67] which show the axial oxygen (O(4)) to be pushed toward the planar Cu site when compared to the YBCO structure (Table 7.4). The comparison to YBCO is properly made by taking the differences in the lattice parameters a, b, and c into account. Therefore, we also show the bond-lengths for "pseudo-YBCO" which is calculated using the lattice parameters for PBCO from Lowe-Ma and Vanderah[67] and the relative atomic positions of YBCO from Beno *et al.*[74]. The difference in Cu(2)-O(4) distance between the diffraction and the XAFS results can be explained by comparing the Cu(2)-O(4) distance as a function of oxygen concentration for R123-type materials. In all these materials that have been measured, the Cu(2)-O(4) distance decreases with increasing oxygen concentration. Our result is consistent with this trend (see Ref. [67]). An extrapolation of the measured Cu(2)-O(4) distance as a function of oxygen concentration in PBCO[67], to an O content of 6.98, yields a bond length of 2.23 Å, in excellent agreement with our result of 2.22 Å.

7.5.4 On the question of clustering in RBCO:Pr (R=rare earth and Y)

An interesting property of $R_{1-x}Pr_xBa_2Cu_3O_7$ is that the larger the rare-earth radius, the lower the Pr concentration required to completely suppress T_c. It has been suggested [71] that this is evidence for clustering of Pr in YBCO:Pr (where the ionic-size difference is comparatively large), thereby maximizing the superconducting Y-Y pairs of cells within a crystal. We had expected that both the Pr and Y K-edge data would be very sensitive to this clustering, by giving the number of neighboring Y and Pr atoms. The data in Fig. 7.4 and 7.5 show a significant change in the structure near 3.5 Å where the Y or Pr neighbor peak occurs, compared to the pure materials YBCO and PBCO. This means that in the 30 and 50% samples there are both Y and Pr neighbors at each Y/Pr site. If large scale clustering were present, these significant changes in the XAFS would not occur. Unfortunately, fits that try to precisely determine the ratio of Pr to Y neighbors are plagued by the interference effects from the Y-Ba and Y-Y peaks, as described in Sec. 7.4.3, which reduces our sensitivity. Consequently, we cannot differentiate between a random distribution and small clusters.

7.6 Conclusion

In summary, we have collected XAFS data on samples with several different concentrations of Pr in $Y_{1-x}Pr_xBa_2Cu_3O_7$ and on CeO_2 at the Y, Pr, Cu, and Ce K-edges. The main result of this investigation is that the XAFS data and analysis show that disorder in the oxygen environment around the praseodymium clearly exists. This disorder is most obvious when comparing the first oxygen peak in CeO_2 to the first oxygen peak in $PrBa_2Cu_3O_7$, which shows a 60% reduction in the Pr-O peak. The amplitude of this peak clearly shrinks with increasing Pr concentration.

This PBCO data is best fit by two harmonic radial distributions for the Pr-O bond, which are centered at $2.27^{+0.03}_{-0.12}$ Å and 2.45 ± 0.01 Å in PBCO. The shorter bond may be broader than the longer one by as much as a factor of 3. The magnitude of this distortion agrees well with the change in bond length in other Pr oxides between Pr^{4+}-O (2.18 Å - 2.32 Å) and Pr^{3+}-O (2.33 Å - 2.66 Å) and is therefore the first structural evidence of a split in the Pr-O bond lengths, and strong evidence for a mixed valent state of Pr in $Y_{1-x}Pr_xBa_2Cu_3O_7$.

We have also verified some results of previous measurements. By comparing the Pr K-edge data to FEFF5 simulations of $PrBa_2Cu_3O_7$ with Pr at the Y site and at the Ba or Cu(2) site, we see very little evidence for any of the Pr existing on the Ba or the Cu(2) site (upper limits of 8 and 10%, respectively). In addition, Cu K-edge data indicate the O(4) site has moved closer to the Cu(2) site (in agreement with Ref. [67]) and therefore may impede charge transfer between the planes and the chains.

Chapter 8

Negatively correlated atomic displacements in $HgBa_2CuO_{4+\delta}$

Since the first high T_c materials were discovered[1], a major question has remained unanswered - what is the mechanism for the formation of Cooper pairs? Another related and potentially important question is - does structure play an important role in high T_c superconductivity? The recently discovered Hg series of high T_c compounds[75] provide yet another opportunity to address these questions. These materials have the highest T_c's to date (T_c=164 K for the three CuO_2 under quasihydrostatic pressure[9]). More importantly, they also have the largest change in T_c with pressure[9] which indicates that local structural distortions may be playing a bigger role than in most other high temperature superconductors. The one CuO_2 layer compound, Hg 1201 ($HgBa_2CuO_{4+\delta}$), has a relatively simple structure (see Fig. 8.1 for definitions of sites); it has no Cu-O chains as found in the YBCO family and, although the structure is very similar to the Tl series, there is very little O in the Hg layer.

Conventional wisdom assigns superconductivity to the CuO_2 plane while the heavy-metal oxide layer (the BaO and Hg layer in Hg 1201) provides a charge carrier reservoir. Over the last five years there has been increasing evidence that structural distortions in this heavy-metal oxide layer play an important role. Consequently, models that involve coupling the superconducting pairs to this layer have received increased attention; for a review of charge transfer, excitonic, and polaronic models, see Ref.[13]. If the coupling involves local correlated atomic positions in pairs of atoms, diffraction experiments will not provide a measure of this correlation because diffraction can only measure average positions and broadening parameters over a macroscopic piece of a crystal. Only experiments which are sensitive to correlated displacements, such as ion channeling, pair correlation measurements from neutron scattering, and XAFS, can measure such effects.

In this report we present XAFS measurements that can be viewed as evidence for a large negative correlation in the relative displacements of the Cu and axial O(2) atoms, and possibly also for the Ba and O(2) atoms. These results can be interpreted in terms of a local, quasistatic, anti-ferroelectric (or ferroelectric) order, possibly induced by the defect O(3) site. Alternatively, it may be caused by a dynamic process in which the atoms are moving together or apart in a correlated manner. These measurements add to the

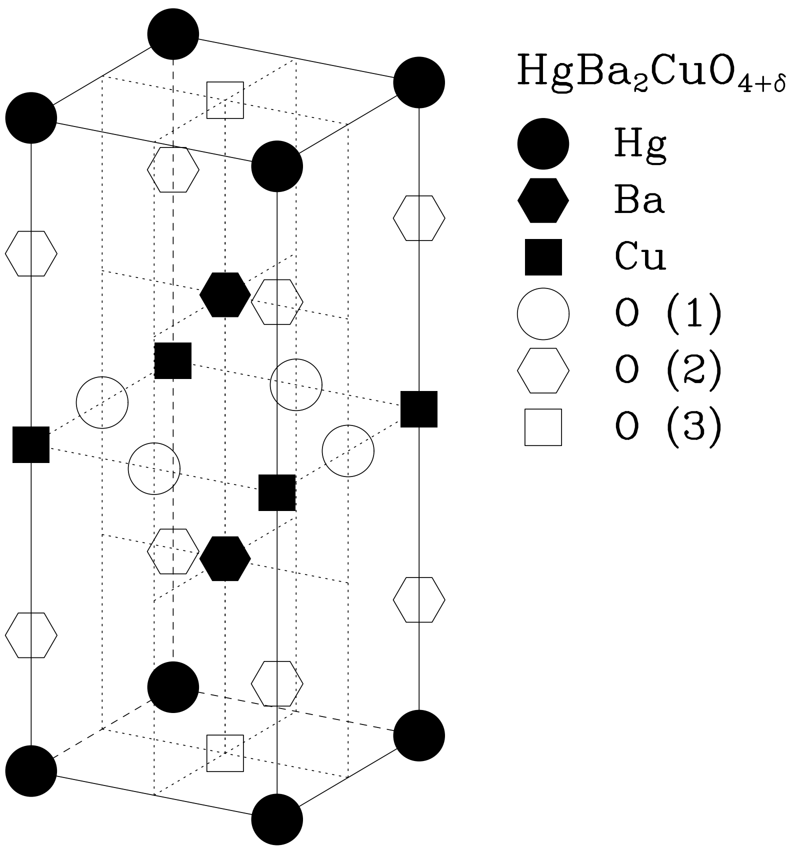

Figure 8.1: The crystal structure for $HgBa_2CuO_{4+\delta}$. The O(3) site is a defect site and has a small occupation.

collection of reports of small anomalies involving the axial oxygen[8, 12, 76, 11]. Several of these anomalies occur near or at T_c, suggesting that these anomalies arise from a lattice coupling to the superconducting pairs.

Transmission x-ray absorption data were collected at 80 K for the Cu K- and the Hg L_3-edge on Hg 1201 samples using a Si(220) monochromator and the Ba K-edge using a Si(400) monochromator at SSRL (beamlines 4-2, 4-3). Complete measurements were obtained for two powder samples: T_c's of 96 K (optimal O concentration, δ = 0.18) and 45 K (slightly O depleted, δ = 0.12). Cu and Hg edge data were also collected for a 30 K sample (O overdoped, δ = 0.23). The XAFS sample preparation, data reduction, and analysis procedures have been described in detail elsewhere[15, 16, 17]. We note that for the Ba and Hg edges, there is significant structure in the background and we have used our iterative method[16] to remove it. Neutron diffraction measurements indicate the samples were essentially single phase. Further details of the neutron diffraction study are provided in Ref. [77].

The Fourier transformed XAFS data and fits for the T_c=96 K sample are shown in Fig. 8.2. The T_c = 45 K data and fits are similar. For the Hg edge the first peak corresponds to two axial O(2) neighbors while the multi-peak in the 3-4 Å range is the sum of the Hg-Ba and Hg-Hg contributions. A comparison of a simple FEFF[19] simulation (using calculated Debye-Waller factors and assuming no distortions) to the data shows that the amplitude of the Hg-Ba/Hg-Hg peak is about a factor of two smaller than expected. This reduction in amplitude indicates that there is some disorder in one or both of these peaks. The disorder is similar for the 96 K and 45 K samples but increases for the 30 K material. The 30 K sample also has a small peak corresponding to the Hg-O(3) atom-pair

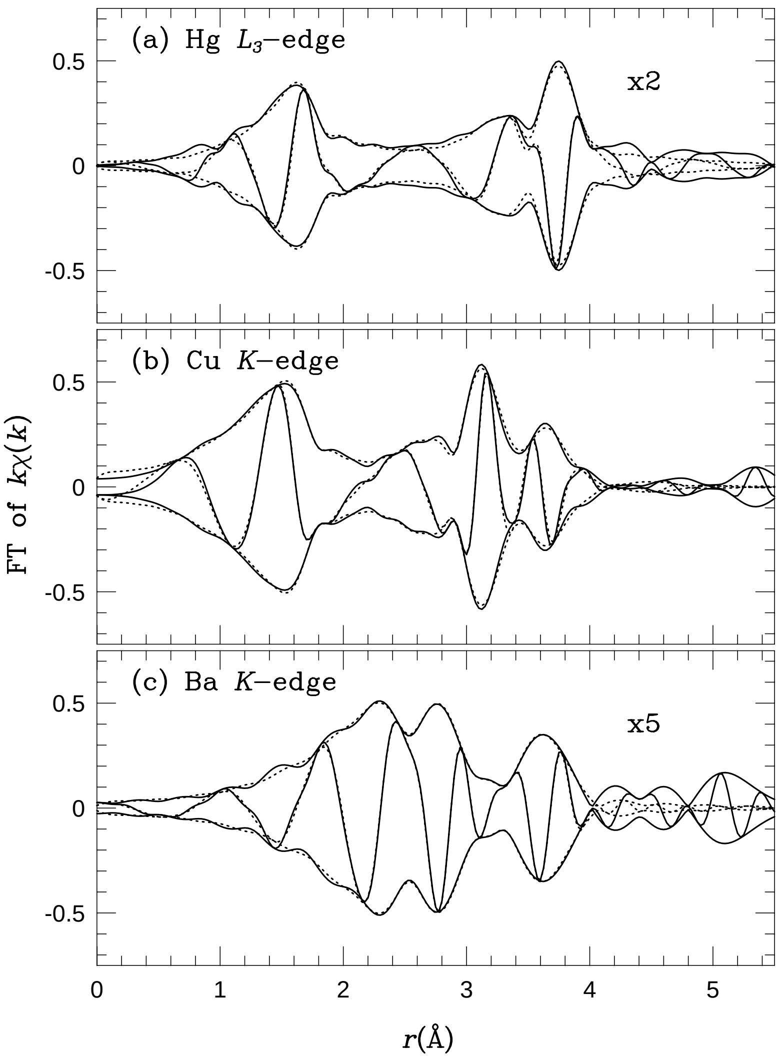

Figure 8.2: Fourier transforms (FT) of $k\chi(k)$ for Hg 1201 (T_c=96 K) at various edges. The top panel (a) is Hg L_3-edge data (solid) and fit (dotted), both transformed from 3.5 to 16.5 Å^{-1}. The middle panel (b) is Cu K-edge data (solid) and fit (dotted), both transformed from 3.0 to 16.5 Å^{-1}. The bottom panel (c) is Ba K-edge data (solid) and fit (dotted), both transformed from 3.5 to 12.5 Å^{-1}. All transform windows are Gaussian broadened by 0.3 Å^{-1}. The Hg and Ba data and fits have been multiplied by a constant factor as indicated in order to compare with the Cu data.

which is not observable for the other samples.

For the Cu edge, the first peak corresponds to the four planar O(1) atoms while the multi-peak over the 3-4 Å region arises from the eight Ba and four planar Cu neighbors. The positions and amplitudes of these peaks are consistent with the structure obtained from diffraction studies on other samples[75, 78, 79]. However there should be another O peak in the XAFS spectra, near 2.2 Å (corresponding to a distance of 2.77 Å in the crystal) from the two axial O(2) atoms. This peak is not obviously present in the spectra shown in Fig. 8.2, which can be fit reasonably well without it. To explain its low amplitude when several diffraction studies[75, 77, 78, 79] as well as our Hg L_3-edge data show this O(2) site to be fully occupied, requires a very broad Cu-O(2) peak. A constrained fit requiring two O(2) neighbors, improves the fit compared to removing the O(2), and yields a very large Debye-Waller parameter (Table 8.1).

The Ba K-edge data are similar to the Cu K-edge data in that the Ba-O(1) peak and the Ba-Cu peaks are consistent with the diffraction results while the Ba-Hg is broadened. However, the Ba-O(2) peak with four O(2) neighbors at ~2.8 Å also has a very low amplitude. Again, a constrained fit yields a large Debye-Waller factor.

As mentioned earlier, XAFS measurements of the broadening factors are fundamentally different from the corresponding diffraction measurements. Diffraction measures the mean-square deviation of a given atom from its average site in the crystal. However, in XAFS we measure the broadening of the distance between atoms a and b:

$$\sigma_{ab} = \sqrt{< (\delta r_a - \delta r_b)^2 >}, \tag{8.1}$$

where δr_a and δr_b are the instantaneous deviations from the average atomic positions for atoms a and b. XAFS therefore measures a *correlated* Debye-Waller factor. A comparison of the XAFS Debye-Waller parameters with the uncorrelated ones obtained in diffraction[77] for similar samples and measurement temperatures, allows a measure of the degree of correlation of the displacements of the neighboring atoms. If we assume that the XAFS measurements of σ_{ab} are absolute, and we define the uncorrelated widths ($\sqrt{U}$ in diffraction) to be σ_a and σ_b, then we can define a correlation parameter ϕ by

$$\sigma_{ab}^2 = \sigma_a^2 + \sigma_b^2 - 2\sigma_a\sigma_b\phi \tag{8.2}$$

If ϕ is near $+1$ we have a highly correlated width, as expected for well ordered materials at low (but not zero) temperatures; if ϕ is zero we have the uncorrelated result which often applies to more distant neighbors. However if ϕ is negative, the atom positions are anti-correlated, as found for small off-center displacements in an anti-ferroelectric system, or for an optical phonon mode (Fig. 3.1.

We expect measurements of ϕ to have fairly large systematic errors. First, the parameters σ_{ab} must be determined absolutely; the standards used to fit the data must have well known Debye-Waller factors. We have recently shown that fits to the XAFS of model compounds, using theoretical standards calculated from the FEFF code[19], give values of σ_{ab} that agree with the correlated-Debye model (the method used by the program) generally within 10%[17]. Second, the samples used in the neutron diffraction experiment are different than the ones used in the XAFS experiment. This problem is potentially much more serious, since measurements of the diffraction width parameters vary considerably from sample to sample. The best comparisons are for the 96 K sample; the diffraction and XAFS samples were both made in the same laboratory using the same technique, both have the same T_c and the measurements were made at the same temperature. However, we obtain the same qualitative results for the measurements of ϕ even when we use other published diffraction data[79]. Significant errors may also be present in the diffraction measurements of σ_a and σ_b, especially in measurements of oxygen atoms. These studies employ neutron diffraction (as opposed to x-ray diffraction) to help minimize this problem. Finally, errors may occur in the diffraction measurements if the atomic broadening is highly anisotropic. The results presented here all assume isotropic broadening factors. Some measurements of the O(2) atom (for instance, Ref. [79]) indicate that it is more disordered in the *ab*-plane than along the *c*-axis. Using such measurements does not qualitatively change the results of this study.

To check that the values of σ_a, σ_b, and σ_{ab} are reasonably consistent, we expect ϕ for well defined nearest neighbor bonds to be near unity for T = 80 K. In Table 8.1 the values of ϕ for Hg-O(2) and Cu-O(1) (the two shortest bonds in this material) are indeed close to unity within 20%. In particular, we note that the Hg-O(2) bond is exceptionally narrow (σ =0.034 Å) even though diffraction shows the Hg width to be quite broad ($\simeq$ 0.1 Å). Another simple check is that the further neighbors generally should have smaller ϕ's than the near neighbors. The most correlated atom-pairs in these fits are the nearest neighbor pairs, as expected. The more striking result of the data in Table 8.1 is that *only* the Cu-O(2) and Ba-O(2) pairs are negatively correlated - these bond distances fluctuate by roughly 0.3 Å. However, such large Debye-Waller factors also have large errors. The errors on the Ba-O(2) pair are large enough to allow for the possibility that the Ba and O(2) atom positions are merely uncorrelated. Also, the Cu and O(2) atom-pair has a value for ϕ that is larger than -1. This seemingly unphysical result can be attributed to using a single-pair gaussian distribution function in the harmonic approximation to model a more complicated pair distribution function in both the XAFS and diffraction data. In order to obtain a positive value of ϕ, σ_{ab} for this peak would have to be ≤ 0.11 Å. Such a peak would be easily observable in our fits, therefore we must conclude that the positions of the Cu and the O(2) atoms are negatively correlated at least to some degree. This together with the positive correlation for the Hg-O(2) pair suggests that the displacements of the Cu and Hg atoms may also be negatively correlated.

A natural way to explain these anti-correlations is to consider a charge redistribution of the valence electrons on the $O(2)^{2-}$ ion. The Hg-O(2) bond is short and has a narrow width, suggesting that one of the electrons on the $O(2)^{2-}$ ion is tightly bound in that bond. The second electron on the $O(2)^{2-}$ ion is weakly bound to four Ba atoms and one Cu atom. If the probability of finding this electron in an orbital linked to Ba or Cu is fluctuating (perhaps because of polaron formation), we expect the positions of the Cu-O(2) and Ba-O(2) pairs to be anti-correlated. Such fluctuation may occur if, for instance, the c-axis conductivity involves electrons hopping on and off the $O(2)^{2-}$ ion. However, XAFS is not sensitive to whether the displacements are static or dynamic, because it is a very fast probe and the lattice is essentially frozen for times as short as the fluorescence lifetime. If the distortions were static, one might expect well-defined off-center displacements as found in ferroelectrics, which would lead to a split nearest neighbor peak (eg. if the O(2) position was different depending on whether the adjacent O(3) site was occupied). In fact, recent Raman studies have shown two A_{1g} modes which involve the O(2)[80], with a dominant mode at 592 cm^{-1} and a smaller peak at 570 cm^{-1}, indicating two possible sites for the O(2) atom. The fit to the XAFS data did not improve significantly when a split peak was included; however we cannot differentiate between two broad peaks and one broad peak. Thus there is either a distribution of static displacements, or the atoms are moving, driven dynamically by some local charge redistribution as discussed above, at a rate somewhat faster than parts of the unit cell can respond.

This hopping process may produce a coupling mechanism between pairs of holes in the CuO_2 plane which is a combination of the polarization and excitonic models. A hole in the CuO_2 plane on a neighboring site to a given $O(2)^{2-}$ ion may cause a redistribution of the electron charge, resulting in increased negative charge density in the Cu-O(2) bond or induce an electron on the $O(2)^{2-}$ ion to hop into the CuO_2 layer. This negative charge will attract a second hole in much the same way as a negative polarization of the lattice would in the usual phonon coupling model, but with a higher cut-off frequency (electronic vs. ionic displacements) beneficial for a stronger pair coupling. As the electronic polarization must be coupled to (anti-correlated) movements of the atoms to explain our observations, the hopping time should not be much shorter than the period of the highest optical phonon frequency involving the Cu, Ba and O(2) atoms to allow the lattice to partially respond. If the phonon frequency and the hopping frequency are closer in this material it may enhance the pair coupling. This idea is in rough agreement with the relatively high frequency A_{1g} mode mentioned above[80] and its pressure dependence[81].

In conclusion, we have analyzed XAFS data on $HgBa_2CuO_{4+\delta}$ at the Hg, Cu, and Ba edges. The extracted pair distances agree reasonably well with diffraction studies. Most of the Debye-Waller factors obtained in XAFS at 80 K, are smaller than the corresponding factors from diffraction measurements, indicating that most near-neighbor bonds involve positively correlated motions of their atomic constituents. Exceptions are the Cu-O(2) and possibly the Ba-O(2) atom-pairs. For these pairs, anti-correlated motions of the atoms are needed to describe the data. Such anti-correlation has been observed in other systems

Table 8.1: Fit results for σ_{ab} and R from XAFS at the Hg L_3-edge, and the Cu and Ba K-edges of a T_c=96 K sample of $HgBa_2CuO_4$. All the results reported here are consistent with the measurements on the T_c=45 K sample. The values of σ_a and σ_b are from Ref. [77]. ϕ was calculated via Eq. 8.2. Both the XAFS and the diffraction data were collected at 80 K. Quoted errors do not include any possible sample differences between the XAFS and the diffraction samples. A single value of the amplitude reduction factor S_0^2 was used for the Ba and Cu edges. The Hg edge data required a separate reduction factor for the first peak. The fit to the Hg-Hg and the Hg-Ba peaks is of poor quality, indicating distortions exist which we are currently unable to model. The Ba-O(2) pair distance had to be held fixed in the fit, so no error was determined.

Bond	R(Å)	S_0^2	σ_{ab}(Å)	σ_a(Å)	σ_b(Å)	ϕ
Hg-O(2)	1.98(1)	0.83	0.034(8)	0.099(5)	0.095(7)	0.94(3)
Hg-Hg	3.83(4)	1.1	0.09(2)	0.099(5)	0.099(5)	0.6(2)
Hg-Ba	3.97(4)	1.1	0.08(1)	0.099(5)	0.073(7)	0.6(1)
Cu-O(1)	1.93(1)	0.80	0.047(10)	0.05(1)	0.081(8)	0.9(2)
Cu-O(2)	2.76(4)	0.80	0.21(4)	0.05(1)	0.095(7)	-3(2)
Cu-Ba	3.34(2)	0.80	0.064(3)	0.05(1)	0.073(7)	0.5(1)
Cu-Cu	3.88(2)	0.80	0.055(6)	0.05(1)	0.05(1)	0.4(2)
Ba-O(1)	2.77(1)	0.925	0.075(2)	0.073(7)	0.081(8)	0.53(7)
Ba-O(2)	2.87	0.925	0.17(4)	0.073(7)	0.095(7)	-1(1)
Ba-Cu	3.34(1)	0.925	0.069(5)	0.073(7)	0.05(1)	0.4(2)
Ba-Ba	3.91(4)	0.925	0.062(4)	0.073(7)	0.073(7)	0.64(7)

(notably the Tl compounds) and is further evidence of an anti-ferroelectric-like distortion occurring in a high T_c superconductor. The nature of this distortion prompted us to outline a simple electron-hopping model that might explain both the distortion and a possible pairing mechanism.

Chapter 9

Comparison of local structure between a film and a single crystal of $YBa_2Cu_3O_{7-\delta}$ as a function of temperature

 The archival version of this work was published in C. H. Booth, F. Bridges, J. B. Boyce, T. Claeson, B. M. Lairson, R. Liang and D. A. Bonn, Phys. Rev. B **54**, *9542 (1996).*

9.1 Introduction

Since the discovery of the high T_c superconductors[1] there have been several measurements of possible structural changes near the superconducting transition. Some measurements were far enough above the noise that the result was immediately convincing to the scientific community, such as Sharma *et al*'s ion channeling measurements of a sudden correlation of the alignment in the ab-plane of the Cu(1) ("chain copper"), O(4) ("axial oxygen") and Cu(2) ("plane copper") atoms in $ErBa_2Cu_3O_7$[8] and in $YBa_2Cu_3O_{7-\delta}$ (YBCO)[82]. Some have relied on relatively small changes in a relatively large signal, such as Horn *et al.*'s diffraction measurement of an anomaly in the orthorhombicity $[(b-a)/(b+a)]$ of YBCO[6], or Mustre de Leon *et al.*'s x-ray-absorption fine structure (XAFS) measurement of a split O(4) position distribution ($\delta r \simeq$0.13 Å) in YBCO that decreases somewhat or disappears ($\delta r \leq$0.11 Å) near T_c[12, 40] . Both of these measurements were initially treated with a fair amount of skepticism, because obtaining a reliable signal for measuring such small changes is difficult. Horn *et al.*'s result has since been confirmed both by diffraction[83] and by capacitive dilatometry measurements[7] and consequently must be considered real, although its relation to T_c is still unclear. On the other hand, Mustre de Leon *et al.*'s measurement has only been partially confirmed by XAFS[84] (see below), and no other experiment has been able to verify the result in YBCO.

The XAFS measurement of a split O(4) site distribution has been taken as a possible explanation for anomalous features in vibrational spectra involving the O(4)[85]. This distribution may also fit into current polaron models for electron-phonon-coupling (for instance, see Refs. [86, 87, 88, 89]). In spite of these important implications, the possibly dynamic nature of the O(4) distribution has never been verified. In fact, it has been suggested that the split distribution is actually due to ordered O(1) vacancies[90], as in the Ortho-II phase of YBCO[91, 92]. Part of the ambiguity in the interpretation lies in the difficulty of the measurement itself. The most serious problems with the XAFS measurements are pointed out by Stern *et al*[84]. In their attempt to confirm the Mustre de Leon *et al.* measurements, they tried several samples with various oxygen concentrations. The only sample that was clearly consistent with a split distribution of the O(4) position had the lowest T_c of the samples measured (89 K). Fits to a split distribution for the other samples were less convincing; both the single-site fit and the split-site fit were unsatisfactory. The sample with the highest T_c (92 K) did not show any temperature dependence near T_c, at least as far as the fits were concerned. Since the measurement relies on such a small change in the overall signal and the results were severely sample dependent, the authors concluded that an independent method is necessary to confirm the split-site character of the O(4) distribution. They also concluded that the relation between the split distribution and T_c must be weak and unimportant to superconductivity since the highest T_c sample showed the least change with temperature. This conclusion is weak, however, because the fits to this T_c=92 K sample were of poor quality.

Unfortunately, no independent experiments have been able to confirm the result in YBCO, although x-ray diffraction analysis has seen a much larger effect in single crystals of $YBa_2Cu_{2.78}O_7$[93], pulsed neutron diffraction (using a PDF analysis[76]) has seen correlated displacements of the Cu and axial oxygen in Tl-2212, and XAFS has seen axial oxygen changes near T_c in Tl-1234[39].

As Stern *et al.* have pointed out, until an independent experiment confirms or refutes the possibly split nature of the O(4) position, the split nature of the O(4) site will be questionable. However, with different samples, analysis techniques, etc. XAFS can still help clarify the issue. For instance, well oriented samples are important for these XAFS measurements because the polarization of the incoming synchrotron light can be utilized to remove the contribution to the XAFS of the in-plane oxygens. Magnetically-oriented powders were used in both the Mustre de Leon *et al.* and the Stern *et al.* studies. Each of these absorption measurements were made in the transmission mode. In the study presented here, we use a 5000 Å film on MgO, a 4000 Å film on $LaAlO_3$, and a 17 μm (1.4% Ni substitutes for Cu) single crystal of YBCO, all with a T_c of 89 K. Each of these samples is highly oriented with the c-axis perpendicular to the sample surface. All measurements were made in the fluorescence mode. Our analysis focuses on the film on MgO and uses the other two samples for comparison.

In contrast to the results of Stern *et al.* and Mustre de Leon *et al*, the film data can be well described by a single, harmonic O(4) distribution that shows only very subtle changes near T_c. These data are very reproducible over a wide range of temperatures, and thus provide a null result to compare with any other results. On the other hand, the single crystal data show a split O(4) distribution below T_c consistent with previous measurements on oriented powders. By comparing a case where the splitting is not present and one where it is, we show that previous XAFS measurements of a split O(4) distribution are not relying on an unusually small signal.

The measurements presented here also provide details of the harmonic broadening of the pair distribution of the atom pairs in the film on MgO. These measurements show interesting temperature dependences which are interpreted as changes in the correlations between the atomic positions in a given atom pair. Fluctuations in the broadening parameters of the Cu(2)-O(4) pair, and to a lesser degree in the Cu(1)-O(4) pair in the vicinity of T_c are also reported.

We begin our report by describing the experimental details in Sec. 9.2. The data analysis procedures are given in Sec. 9.3. The isolation of the O(4) contribution to the XAFS is presented in Sec. 9.4. Results of detailed fits to the film data are given in Sec. 9.5. Consequences of observed features in the data are discussed in Sec. 9.6 and the conclusions of this work are summarized in Sec. 9.7.

9.2 Experimental details

The thin film samples of YBCO were deposited by off-axis single magnetron sputtering onto a MgO and a $LaAlO_3$ substrate. The film on MgO is estimated to be 5000 Å thick, and the film on $LaAlO_3$ is approximately 4000 Å thick. On cooldown, the films are brought into equilibrium with oxygen at 700 Torr at 450°C. This condition fixes the chemical potential for oxygen. The maximum T_c occurs for the films when they are brought into equilibrium at 450°C, 200 Torr of oxygen. This maximum is about 90 K. T_c drops somewhat for more oxygen (it drops about 1 K for annealing at 700 Torr) and for less oxygen. The maximum critical current at 4.2 K increases as the oxygen anneal pressure increases. This increase in the critical current is consistent with an increasing carrier density and a decreasing correlation length. Therefore the films are "overdoped" somewhat relative to maximum T_c[94]. The actual carrier concentration, and therefore the actual oxygen concentration, is not known since doping mechanisms other than oxygen incorporation exist,such as antisite disorder and substitions on the cation sites. The oxygen content is also affected by the large strains and high density of twin boundaries found in thin films.

X-ray diffraction measurements indicate less than 1% impurity phases. The diffraction measurements also indicate that the films are oriented with their c-axes perpendicular to the plane of the film with less than 1% a- or b-axis impurities for the film on MgO, and <3% for the film on $LaAlO_3$. TEM pictures confirmed that films created in the same way are c-axis oriented, with trace impurities and that the crystals are twinned. The transition temperatures were measured with the standard four-probe technique and found to be 89 K. A more detailed description of the sample preparation can be found in Ref. [95].

For comparison, we use a fairly large single crystal of YBCO which is nominally $YBa_2Cu_{2.958}Ni_{0.042}O_{6.95\pm0.005}$, that is, about 1.4% Ni substitutes for Cu. Although the oxygen content is well determined for this sample, the presence of nickel will affect the overall hole concentration and the local oxygen stoichiometry. Unlike other transition metals, Ni substitutes onto *both* the Cu(1) and the Cu(2) sites, and causes some distortions at least around the Cu(1) site[96]. Ni K-edge data from this sample are qualitatively consistent with our previous work on powders, but we could not further elucidate the nature of the distribution or the local distortions. Therefore we cannot know the local oxygen concentration around Cu sites and cannot say whether the local oxygen vacancies around the Cu(1) are the same or different than in $YBa_2Cu_3O_{6.95}$. The sample is, however, a high quality superconductor which is c-axis oriented with a T_c= 89 K. Details of the sample preparation are described in Refs. [97] and [98]. The thickness is estimated to be $\sim$ 17 μm by looking at the Cu K-edge step in the x-ray transmission spectrum.

X-ray fluorescence measurements were made on beamline 7-3 at the Stanford Synchrotron Radiation Laboratory (SSRL). The samples were placed in an Oxford helium cryostat and oriented such that the incident x-ray beam was striking the surface of the samples between 10-12 degrees. The x-ray absorption cross section is proportional to $< \vec{\epsilon} \cdot \hat{r} >^2$, where $\vec{\epsilon}$ is the polarization vector of the incoming light, and $\hat{r}$ is the unit vector pointing along the direction of the ejected electron. The amount of signal from atoms in the ab-plane, such as the O(1) or O(2) oxygens, is small, since this plane is nearly perpendicular to $\vec{\epsilon}$; in this case, such a signal is $\sim \cos^2((79°) \cong 4\%$ of the signal from atoms along $\vec{\epsilon}$. Such a small signal cannot explain any of the effects we report in this paper.

Temperature was regulated via two sensors, one in the helium chamber and one about two inches above the sample. Because of the geometry and later calibration measurements, we estimate that the absolute temperature of the sample is probably 1-3 K higher than the sample sensor was indicating (the "nominal" temperature). Relative changes in the temperature of these data should be much better and is probably around 0.5 K. All reported temperature measurements of the XAFS data are the nominal temperature.

The fluorescence x-rays from the film sample on MgO and the single crystal were detected using a 13-element Ge detector. This detector allows for energy resolution that isolates the Cu K_α peak and eliminates any need for background fluorescences to be removed from these data. Count rates in each channel were kept well below saturation levels ($<$ 20% of saturation), but were in any case corrected for the dead-time-constant ($\sim$ 5-10 μs) introduced by the energy-resolving peak-shaping filters. Besides the ability to resolve the Cu K_α fluorescence, the main utility in using the Ge detector is to aid in the removal of Bragg peaks in the absorption spectrum. Because the Bragg spikes occur at the incident beam energy, the energy resolving power of the Ge detectors can partially discriminate against them. However, a large change in the fluorescence flux can bring the detectors much closer to saturation, and thus the dead-time correction becomes more important.

If a Bragg spike is particularly strong, the dead-time correction cannot account for the additional flux accurately enough, and the affected data must be removed. Such removal is accomplished by replacing the affected data by the normalized mean of the other channels. In this way we can usually generate a full absorption spectrum over the energies of interest with almost no experimentally induced spikes or dips. This method provides a significant advantage over more traditional single channel ionization counters when one realizes that for thin films on well-oriented substrates, or for single crystals, Bragg spikes can affect data over tens of eV.

Unfortunately, features which we call "glitches" can still arise from nonuniformities in the sample coupling to nonuniformities in the incident beam[99, 38]. Since these occur in all the channels of the Ge detector, we must remove such features by fitting a low (2nd or 3rd) order polynomial through neighboring (unaffected) data points and replacing these data with the fit. Fortunately, glitches often only affect between one and four successive data points, and so this procedure does not significantly alter the XAFS.

The fluorescence x-rays from the YBCO film on $LaAlO_3$ were collected using a gas-ionization detector with a Ni filter. This detector does not allow for easy energy discrimination, and consequently background fluorescence from atoms other than the Cu atoms in our sample contribute $\sim$1/3 of the total x-rays. This system allows us to look at some features of the XAFS spectrum from this sample, but does not allow for detailed fits to be performed with any reliability since amplitude information requires at least knowing the details of the background fluorescences, if not removing them (as with the Ge detector).

9.3 Data Analysis

Our data analysis procedures have been detailed elsewhere for standard transmission experiments. In this work, we will describe briefly the general procedure and only give details where significant differences in the procedure arise over Refs. [15, 17, 16].

9.3.1 Basic XAFS

The main features in an x-ray absorption spectrum are due to single electron excitations, namely, the photoelectric effect. These excitations appear as sudden jumps in the absorption coefficient $\mu(E)$. In a solid, the data just above these jumps exhibit oscillatory structure which has been named X-ray Absorption Fine Structure (XAFS). The XAFS are isolated by defining a function

$$\chi(E) \equiv \frac{\mu(E) - \mu_0(E)}{\mu_0(E)} \tag{9.1}$$

which is used just beyond the edge, normally > 25 eV. $\mu_0(E)$ is a normalization function which is the absorption due to all processes that do not include the photoelectron backscattering effect described presently.

The oscillations in $\mu(E)$ are primarily due to an interference effect between the outgoing photoelectron's wave function and the part of the photoelectron's wave function which has scattered off nearby neighbors and returned to the absorbing atom. As the photoelectron's wave vector is increased, the interference is modulated with a frequency given by twice the distance to the backscattering atom. There are several other factors which must be taken into account. The version of the "XAFS equation" that we use in our data analysis is

$$\chi(k) = Im \sum_i A_i \int_0^\infty \frac{g_i(r) e^{i(2r+2\delta_c(k)+\delta_i(k))}}{r^2} dr \tag{9.2}$$

where the amplitude factor A_i is given by

$$A_i = N_i S_0^2 F_i(k), \tag{9.3}$$

N_i is the number of equivalent atoms in shell i, S_0^2 is the "amplitude reduction factor" that accounts primarily for many-body effects that reduce the XAFS oscillation amplitude such as shake-up or shake-off, $F_i(k)$ is the backscattering amplitude of the photoelectron off neighbors i including a reduction due to the mean-free path of the photoelectron, $g_i(r)$ is the pair distribution function for the absorbing and backscattering atoms, and the phase shifts of the photoelectron from the central and the backscattering atom are give by $\delta_c(k)$ and $\delta_i(k)$, respectively. The distribution function $g_i(r)$ is usually taken to be harmonic:

$$g_i(r) = \frac{1}{\sqrt{2\pi}\sigma_i} e^{\frac{-(r-R_i)^2}{2\sigma_i^2}}, \tag{9.4}$$

where R_i is the average distance between the central and the backscattering atoms i, and the broadening factor σ_i (otherwise known as the Debye-Waller factor) combines the effects of thermal and static disorder. If a shell i contains atoms that are inequivalent, then σ_i may also be used as a measure of any distortion in the shell, even though such distortions are rarely harmonic.

In studies of well-ordered materials (such as YBCO) we expect there to be very little difference in the bond lengths measured by XAFS compared to diffraction. In fact, with the exception of the O(4) site, there are many XAFS studies which demonstrate the strong agreement between local structure in YBCO (and most of its relatives) and the average structure[51, 100, 101]. On the other hand, comparative measurements of the correlated

Debye-Waller factors given by XAFS and the uncorrelated ones given by diffraction have been virtually ignored by most experimenters.

Part of the reason for not making direct comparisons between XAFS and diffraction broadening factors is that getting the absolute broadening factor is not always possible. Experimental measurements of amplitude functions have their own (usually unknown) broadening, and until recently, theoretical calculations were not of high enough quality to give reliable results. FEFF6[19, 20], written by Rehr, Zabinsky and co-workers, has been shown to calculate accurate backscattering amplitudes and phase shifts, and even gives reasonable values for Debye-Waller parameters for simple materials with known Debye temperatures[17, 21]. Such calculations provide a backscattering amplitude function with a known (zero) width for absolute comparison to real atom pairs. Although only experience will allow us to determine how accurate absolute measurements of correlated broadening factors really are, our limited experience indicates that they are probably within 10% in most cases.

Another reason direct comparisons are rarely made is simply that diffraction and XAFS width parameters measure different quantities. (A useful text describing more details beyond the following discussion is Ref. [14].) Diffraction relies on coherent diffracting of x-rays off many crystal lattice planes to generate a diffraction spot, and therefore its measurements of atom positions and broadening factors gives an average over many unit cells. XAFS depends only on the instantaneous (within $\sim 10^{-15}$ sec) position of neighboring atoms with respect to the central (absorbing) atom, and therefore the broadening factors are a measure of variations in an atom-pair's distance. For example, if two neighboring atoms are vibrating with the same (spatial) amplitude W but are somehow rigidly connected, the bond length would never change, and XAFS would measure a zero width. Diffraction would measure broadening factors for the two atoms to be W. Mathematically, if δr_X is the instantaneous deviation of atom X's position from its mean position, the average deviation in the distance between atoms A and B is given by

$$\begin{aligned} \sigma_{AB} &= \sqrt{< (\delta r_A - \delta r_B)^2 >} \\ &= \sqrt{< \delta r_A^2 > + < \delta r_B^2 > -2 < \delta r_A \delta r_B >}. \end{aligned} \quad (9.5)$$

If we define $\sigma_A = \sqrt{< \delta r_A^2 >}$ (which equals $\sqrt{U}$ in conventional diffraction notation), then the last term can vary between $-2\sigma_A\sigma_B$ and $+2\sigma_A\sigma_B$, depending on the degree to which the motions of the two atoms are correlated. One can define a "correlation" parameter ϕ from

$$\sigma_{AB}^2 = \sigma_A^2 + \sigma_B^2 - 2\sigma_A\sigma_B\phi. \quad (9.6)$$

Since σ_A^2 is given by diffraction experiments, we can provide measurements of correlation factors. ϕ will vary between $+1$ for atoms vibrating in phase with each other (like in an acoustical phonon), 0 for atom-pairs that are separated by a few unit cells at temperatures well above the Debye temperature, and -1 for pairs that are moving out-of-phase with each other (like in an optical phonon). Of course since the XAFS measurements give average atom-pair distances over the crystal, static disorder can produce the same results. These concepts assume gaussian forms for the distribution functions. If anharmonic distributions exist, the interpretation of measurements of ϕ will be more ambiguous.

9.3.2 Data Reduction

An initial estimate of $\chi(k)$ is obtained by approximating $\mu_0(E)$ in Eq. 9.1 by a cubic spline though $\mu(E)$, k by $\frac{\sqrt{2m(E-E_0)}}{\hbar}$ and E_0 by the energy at the half-height of the edge. The data are fit in r-space as described in Ref. [15]. The fit is then subtracted from the data to obtain a residue which can be utilized to make a better estimate for $\mu_0(E)$, as described in Ref. [16].

The data have been corrected for the additional "self-absorption" of the fluorescing photon in the sample using a treatment which goes slightly beyond the usual correction (for instance, see Tröger *et al.*[37]) by including the finite thickness of the sample and the effect of the XAFS oscillations in the correction term. This amplitude correction for the 5000 Å film is small ($\sim$ 8% of $\chi(k)$), but for the 17 μm single crystal the correction is more significant ($\sim$ 60% of $\chi(k)$.

An example of $k^3\chi(k)$ for the film on MgO which has been obtained using the above procedures is displayed in Fig. 9.1. The Fourier transforms (FT) of $k^3\chi(k)$ for these data as well as for one temperature of the single crystal data are shown in Fig. 9.2.

9.4 Isolating the XAFS signal due to the O(4) contribution

Since the information above 2.5 Å is complicated, we had to perform fits to the data to discern any information about the Y, Ba and Cu environment. These fits are described in Sec. 9.5. However, since the Cu(1)-O(4) and Cu(2)-O(4) peaks are relatively well separated, we can isolate them and back-transform the data to k-space. Mustre de Leon *et al.* based their argument that the O(4) position was split by observing anharmonic behavior in the Fourier filtered k-space data in the form of a beat near 12 Å^{-1}. If a two-site distribution exists, we expect the contributions of the two atom-pairs to be split into four distinct distances: two corresponding to the mean Cu(1)-O(4) distance $\pm$ the splitting ($R_{Cu(1)-O(4)} \pm \frac{\Delta_r}{2}$) and two corresponding to the mean Cu(2)-O(4) distance $\pm$ the splitting

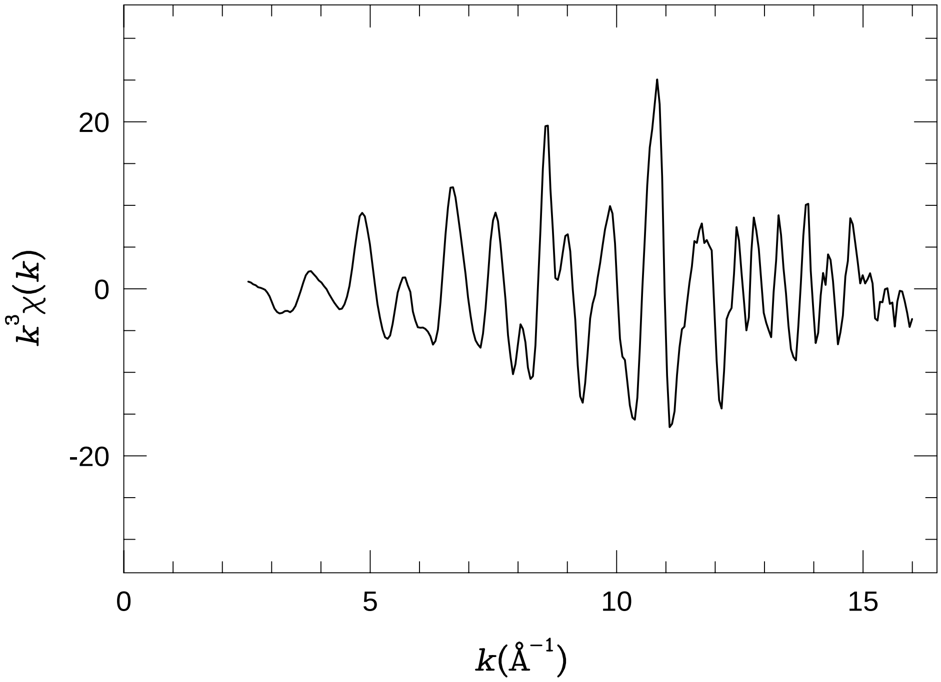

Figure 9.1: $k^3\chi(k)$ vs. k for a YBCO film on MgO at T=20 K with the x-ray polarization parallel to the c-axis of the film. These data have been dead-time corrected and had some minor glitches removed, as described in the text. Data from the single crystal are of comparable quality. Data from the film on $LaAlO_3$ have similar signal-to-noise, however, the energy range is shorter.

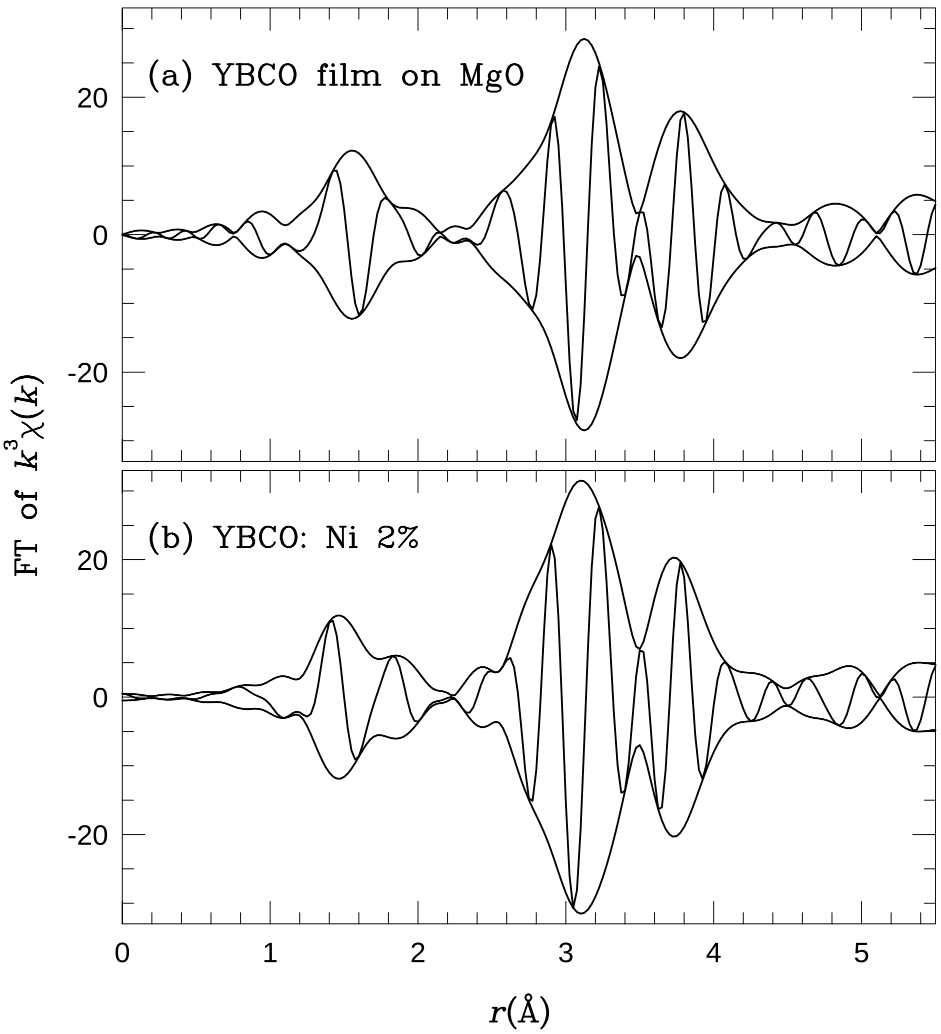

Figure 9.2: The Fourier transform (FT) of $k^3\chi(k)$ ($\equiv \tilde{\chi}^3(r)$) vs. r for (a) the same sample as in Fig. 9.1, and (b) the single crystal of YBCO: Ni 1.4%. Data are transformed with a Gaussian window between 3-15.5 Å^{-1} and broadened by an additional 0.3 Å^{-1}. The oscillating curve is the $Re(\tilde{\chi}^3)$, and the envelope of this curve is the amplitude, $[Im(\tilde{\chi}^3(r))^2 + Re(\tilde{\chi}^3(r))^2]^{\frac{1}{2}}$. The peak at 1.55 Å corresponds to the Cu(1)-O(4) atom pair, while the shoulder of this peak at 2.0 Å corresponds to the Cu(2)-O(4) atom pair. The multi-peak between 2.4 and 3.4 Å is a combination of the Cu(2)-Y, Cu(2)-Cu(2), Cu-Ba and Cu(2)-O(2,3) atom pairs. Lastly, the peak at 3.8 Å is the Cu(1)-O(4)-Cu(2) multiple scattering peak. The peak positions are shifted from the actual pair-distances because of the combined effect of δ_c, δ_i and $F_i(k)$ in Eq. 9.2.

$(R_{Cu(2)-O(4)} \pm \frac{\Delta_r}{2})$. Since the XAFS signal for each of these distances is oscillatory, a small splitting will generate a beat in the XAFS signal at a k-vector given by $2k\Delta_r = \pi$. In order to make our data directly comparable to their's, we have also isolated the O(4) contribution in this way. First, the FT of $k^3\chi(k)$ was obtained as in Fig. 9.2. We chose k^3-weighting for this transform because the O(4) peak is much better resolved than in a k-weighted transform. The Fourier transforms of the $k^3\chi(k)$ data were then back-transformed from 1.3 to 2.2 Å . The O(4) contribution from this procedure is displayed for the single crystal in Fig. 9.3 and for the film on MgO in Fig. 9.4. The sinusoidal behavior in both these figures is the sum of the Cu(1)-O(4) and the Cu(2)-O(4) components.

The O(4) contribution in the single crystal displayed in Fig. 9.3 is in rough agreement with the original work of Mustre de Leon [12]; although the data in the 11-13 $Å^{-1}$ range varies from temperature to temperature, the T=83 K and the T=86 K data show clearly anharmonic behavior near 12 $Å^{-1}$, indicating a splitting of about $\Delta_r \simeq 0.13$ Å. In fact, except for the T=100 K data, none of the single crystal data can be fit with a single, harmonic distribution for the O(4) site (Sec. 9.5.2).

The data from the film on MgO in Fig. 9.4, on the other hand, displays harmonic behavior at all temperatures and shows very little change from temperature to temperature. This harmonic behavior persists out to 16 $Å^{-1}$. Since a beat may still occur at higher wave vectors, these Fourier-filtered k-space data set an immediate upper limit of 0.10 Å. The character of the film data is distinctly different than the single crystal data, showing little if any splitting. This result also applies to the film on $LaAlO_3$ (Fig. 9.5) and therefore may be a generic result of YBCO films. However, it should be noted that this film was grown under similar conditions to the film on MgO.

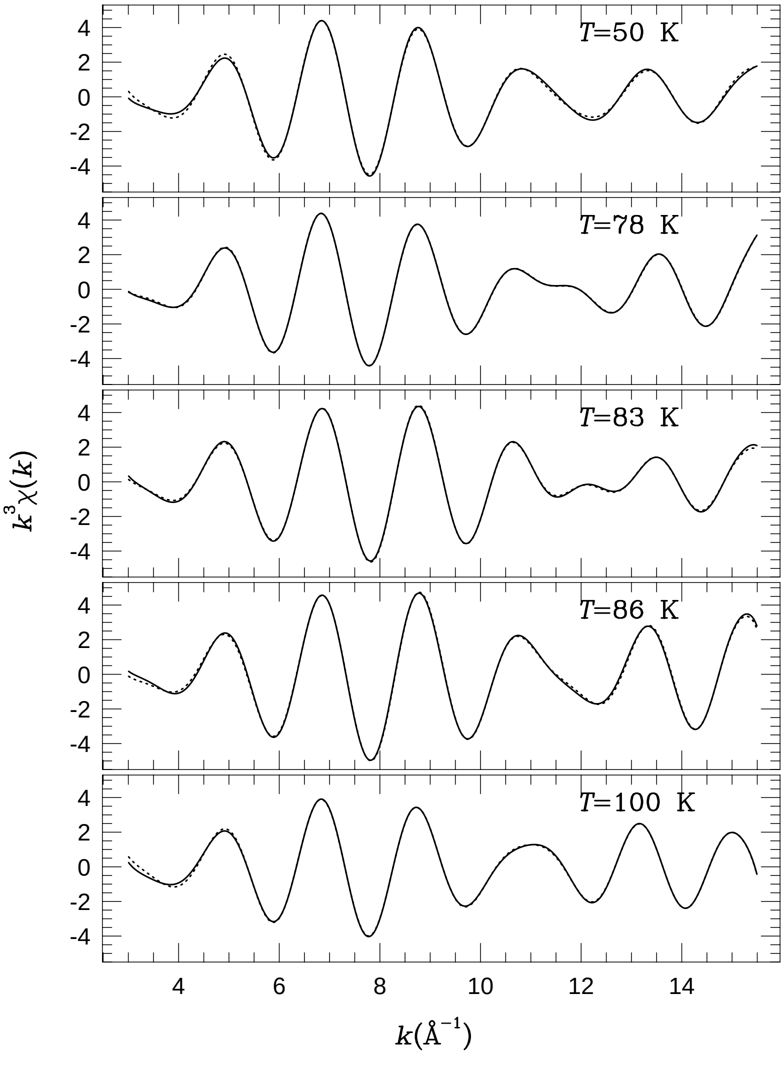

Figure 9.3: O(4) contribution to $k^3\chi(k)$ vs. k at several temperatures for the single crystal of YBCO: Ni 1.4%. The solid lines are the data and the dotted lines are the fits. Each fit assumes a split O(4) site except the T=100 K fit. The O(4) contribution was obtained by back-transforming r-space data (Fig. 9.2) between 1.3-2.2 Å. Contributions from higher shells (say, from the Cu(2)-Y peak) have been shown to be negligible[40].

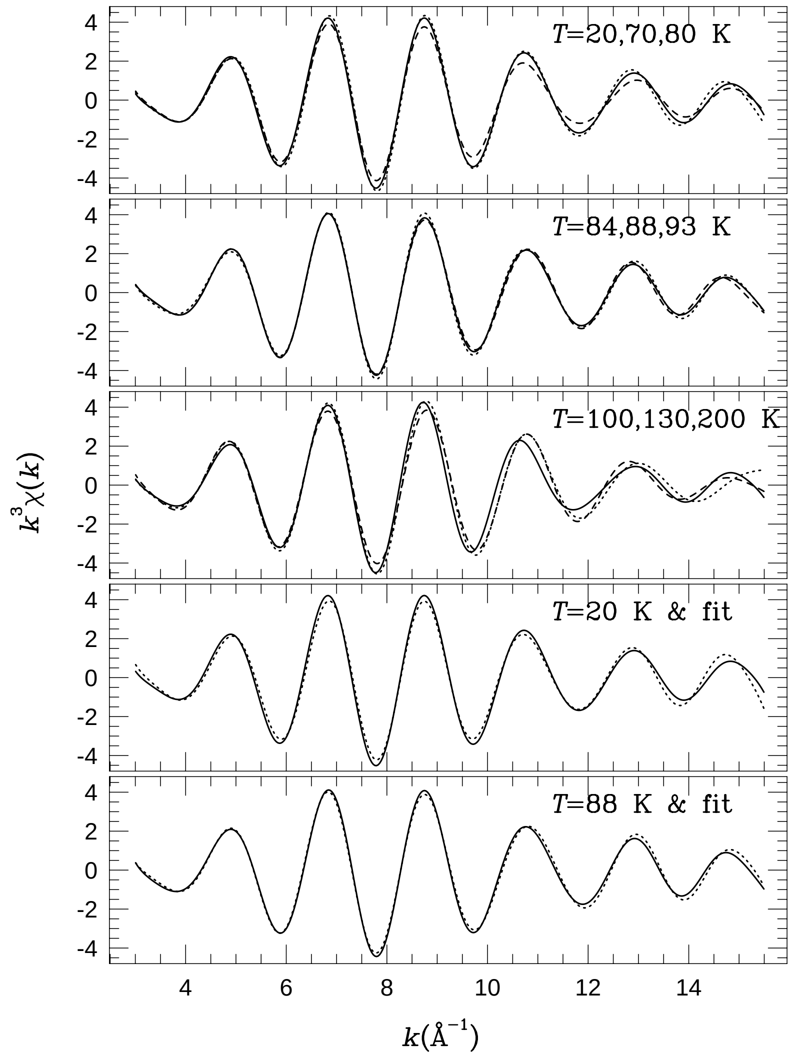

Figure 9.4: O(4) contribution to $k^3\chi(k)$ vs. k at several temperatures for the YBCO film on MgO. The O(4) contribution was obtained in an identical fashion to the data in Fig. 9.3. Only half the data are displayed for clarity; an additional scan was taken in between each of the temperatures displayed here. The bottom two panels show fits to the O(4) contribution to $k^3\chi(k)$ vs. k for the YBCO film on MgO at T=20 K and 88 K. Fits assume a single O(4) site.

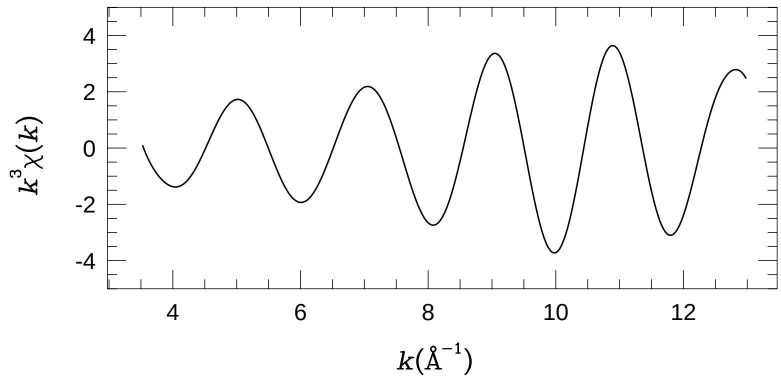

Figure 9.5: O(4) contribution to $k^3\chi(k)$ vs. k for the YBCO film on $LaAlO_3$ at T=70 K. Full spectrum $k^3\chi(k)$ data were transformed between 3.5-13 Å^{-1} (Gaussian broadened by 0.3 Å^{-1}), and then back-transformed between 1.4-2.2 Å. The range of data does not extend to as high k as the data in Fig. 9.3 and Fig. 9.4, however, there is no beat feature in the 11-12 Å^{-1} region in contrast to the data in Fig. 9.3.

9.5 Fits

Although the raw data has provided much useful information about the nature of the O(4) site distribution, we can still learn more details both about the O(4) distribution and about the further neighbors by performing fits of the spectra to the sum of theoretical standards. Such fits provide more quantitative details about the local environment around the copper atoms and allow us to deconvolve the contributions of overlapping peaks due to the Cu(2)-Y, Cu(2)-Cu(2) (between the planes), Cu(2)-Ba, Cu(1)-Ba and the Cu(1)-Cu(2) pairs. Furthermore, by fitting the data to theoretical standards calculated by FEFF6 we can obtain absolute estimates of the broadening factors σ and compare them to results from diffraction studies, thus allowing for measurements of the correlation parameter ϕ (Eq. 9.6).

We only report fit results beyond the near-neighbor Cu(1)-O(4) and the Cu(2)-O(4) atom pairs as a function of temperature for the YBCO film on MgO data.

9.5.1 Fitting procedures

Although weighting the XAFS $\chi(k)$ by a factor of k^3 enhances the high k data where the beat in the O(4) part of the spectrum is likely to occur, we have found that fits to data weighted by a single factor of k give more reliable results overall. In general, if we are not focusing on the O(4) part of the spectrum, we fit our data to the FT of $k\chi(k)$. Fitting to the FT reduces the effect of overlapping peaks[15]. Since XAFS can be thought of as a sum of the contribution to the absorption of the individual atom pairs, we calculate $F(k)$, $\lambda(k)$, $\delta_c(k)$ and $\delta_i(k)$ given an approximate atom cluster for each scattering path using FEFF6. This information for each path is called a "standard." The data are fit to a sum of theoretically calculated standards which include all single scattering paths up to the Cu(1)-Cu(2). The only multiple scattering paths that are included involve the Cu(1)-Cu(2) path and the intermediate O(4). The Cu(2)-planar oxygen path across the planes ($\sim$3.65 Å) was too low in amplitude to obtain reliable fit results, so its parameters were fixed. Other multiple scattering paths were found to be negligible, or were dominanted by the single scattering paths.

Several of the parameters were constrained in order to decrease the number of fit parameters. The Cu(2)-Y and the Cu(2)-Cu(2) distances were constrained such that the yttrium rests in the center of the eight Cu(2) neighbors given the diffraction measurements of the a and b lattice parameters of typical samples. This constraint was necessary to fit the Cu(2)-Cu(2) peak (3.38 Å), which is small compared to the nearby Cu(2)-Y (3.21 Å), Cu(2)-Ba (3.37 Å), and Cu(1)-Ba peak (3.48 Å). Also, if the Cu-Ba peaks were allowed to vary over a broad range, they would often fall into a false minimum in the fitting parameter such that they were ~ 0.04 Å too long. This behavior was noted by Stern *et al.*[84]. However, we were able to determine by fits to a CuI standard (a Cu-I standard should be very similar to a Cu-Ba one) that this error was due primarily to the overlap of several neighboring peaks in YBCO, and not to unusual errors in the FEFF6-generated backscattering amplitude. We therefore only allowed the Cu-Ba peaks to vary over a narrow range (±0.02 Å from the diffraction result). All width parameters were allowed to vary freely, except $\sigma_{Cu(2)-O(2,3)}$ (across the planes), which was held fixed. E_0's for like-atoms were held equal, but were allowed to vary between different types of atoms to help correct for minor errors in the FEFF6 phase calculations.

The aim of these fits is to identify parameters that change with temperature. Since measurements of S_0^2 and σ are correlated, we performed a fit where these parameters were allowed to vary freely, and then calculated the average for S_0^2 for each peak. A similar correlation occurs between measurements of R_i and E_0, so average E_0's for the individual peaks were also determined. The values of S_0^2 and E_0 were then fixed for each path and the fits were performed again. By holding S_0^2 and E_0 fixed for all temperatures, we ascribe all changes in the peaks' amplitude and frequency with temperature to changes in σ_i and R.

Although S_0^2 should be the same for all paths in principle, we found that if a single value of S_0^2 was used high quality fits could not be obtained for the Cu(1)-Cu(2) peak (which includes multiple scattering off the O(4) atom). The fit was improved by allowing this one peak to have an S_0^2=0.75, while all other peaks use an S_0^2=0.90.

The maximum number of parameters given our fit range using the method of Stern[102] is 29. The total number of parameters in these fits was 17, well below the maximum.

Errors in the parameter measurements are difficult to estimate reliably in XAFS fits. We estimate the errors on all the parameters from the covariance matrix generated by the fit. The variance of the data used in the covariance matrix is obtained by assuming that the residual difference between the data and the fit is normally distributed. This procedure only accounts for random errors and thus should describe relative errors between data at nearby temperatures. Systematic errors due to problems in the FEFF6 calculation, self-absorption corrections, estimates of μ_0, etc., will cause overall shifts in the best fit. Absolute errors on these measurements are roughly $\leq \pm 0.01$ Å in R and $\leq \pm 10\%$ in S_0^2 and σ for the near-neighbor oxygens[17], and $\leq \pm 0.02$ Å in R and $\leq \pm 15\%$ in S_0^2 and σ for the overlapping neighbors between 3 and 4.1 Å.

9.5.2 Fitting results

O(4)-site distribution in the single crystal

As suggested by the presence of the beats, a two O(4)-site distribution was necessary to fit the single crystal data in Fig. 9.3 for the four lowest temperatures. The fits shown in Fig. 9.3 all assume a two-site distribution for the O(4) except for the T=100 K data. For the T=100 K data, a single site for the O(4) produces a reasonable fit; the slight dip in the amplitude at ~ 11 Å^{-1} can be modeled by an interference between a single Cu(1)-O(4) path and a single Cu(2)-O(4) path. Note that the data in this region is still visibly different from the film data. The features in the T=50, 78, 83, and 86 K data between 10 and 13 Å^{-1} are modeled by two Cu(1)-O(4) paths and two Cu(2)-O(4) paths, with each path length split by 0.12 ± 0.01 Å and 0.06 ± 0.06 Å, respectively. We did not observe any obvious trend with temperature other than for the T=100 K data.

The two-site fits to the single crystal data may be deceptively good. In order to obtain these fits, unphysically small (< 0.01 Å) values for the broadening factors were needed. In addition, the sum of the amplitudes for these peaks (which should add up to the number of neighbors times S_0^2) is about 50% too high. These exceptionally narrow peaks indicate that besides the split peak distribution, further anharmonicity must exist. A common way to model anharmonicity in XAFS data analysis is to expand Eq. 9.2 about R_i for a given atom-pair in powers of $< r^n >$, otherwise known as a "cumulant expansion" ($< r^n >$ is the n^{th} moment, M_4 is the part of the 4th moment that is different from a gaussian, namely $M_4 =< r^4 > -3\sigma^4$)[103]. The 2nd cumulant is the width in the harmonic approximation, or the Debye-Waller factor. The 3^{rd} cumulant affects the phase shift. The 4^{th} cumulant multiplies the overall amplitude by a factor $e^{\frac{2}{3}k^4 M_4}$. If the exponent in this term is positive, it *increases* the amplitude of the XAFS at higher wave vectors, acting like an imaginary Debye-Waller factor, or like a distribution with a cusp which takes weight from the center of the distribution and puts it into the wings[104]. Excellent fits to the single crystal data can be obtained by allowing the four Cu-O(4) peaks to have $M_4 \cong 2.7 \times 10^{-5}$ Å^4. These fits have much more reasonable Debye-Waller factors (~0.04 Å) and S_0^2 is no longer 50% too large. With such a large value of M_4, the cumulant expansion is no longer accurate above a k of ~ 14 Å.

These fits serve to illustrate that we can model the O(4) site distribution with reasonable values for the fit parameters, but that the fits are not unique. Because S_0^2, σ and M_4 are so correlated for these slightly separated Cu-O(4) peaks, a study of the temperature dependence of any of these parameters would produce questionable results. The only firm result is that at least three, and possibly four, atom-pair distances are necessary to describe the beat structure in the k-space transforms for the single crystal. The actual O(4)-site distribution $g(r)$ may be more complicated.

Table 9.1 reports fit results to the further neighbors for the T=50 K sample.

Fits to the film on MgO

The Cu(1)-O(4) and Cu(2)-O(4) peaks are well fit by a single O(4) site in the film data (Fig. 9.4), as suggested in Sec. 9.4. Allowing for a two site distribution with a $\Delta_r \geq$ 0.09 Å did not produce reasonable fits. Fits to the film data of a similar quality as to the single crystal data are obtained without assuming any anharmonic behavior in the atom-pair distances out to $\sim$ 4.1 Å. Fig. 9.6 shows the fit to the film data over this range both in k-space and in r-space, and Table 9.1 reports the fit to all the parameters for both the single crystal and the film on MgO at T=50 K. No significant deviation between the XAFS atom-pair distance measurements and standard diffraction measurements were observed, except for the unusually short Cu(2)-O(4), Cu(2)-Cu(2) and Cu(1)-Cu(2) pairs, which are about 0.02 Å shorter than in the single crystal diffraction measurements. Although the c-axis lattice parameter was not measured from diffraction experiments on these samples, samples made under similar conditions have c-axis lattice parameters between 11.68 and 11.72 Å. Therefore, the short atom-pairs measured by XAFS indicate some systematic error, either in the model or in the standards. In particular, these differences could be related to systematic errors in FEFF6-generated standards that occur in the wings of the backscattering amplitude in r-space[17]. Both the Cu(2)-O(4) and the Cu(2)-Cu(2) signals are small compared to the other peaks in the spectrum, and therefore are more susceptable to the wings of the Cu(1)-O(4), Cu-Ba and Cu-Y signals. The Cu(1)-Cu(2) peak has a large signal; however, the standard also involves the intervening O(4) atom, in addition to

Table 9.1: Comparison between fit results to the single crystal of YBCO:Ni 1.4% (xtal) and the film of YBCO on MgO at T=50 K. *n.b.* stands for "number of bonds per unit cell." Neutron diffraction results of Sharma *et al.*[45] are also given for comparison, and measurements of ϕ are reported for the film data. Errors marked with an "x" are unreliable because the pair-distribution function deviates significantly from a gaussian. Imaginary Debye-Waller factors often accompany these distributions; such parameters cause the XAFS oscillations to *increase* with k. Some parameters were held fixed or constrained in the fits. See Sec. 9.5.2 for further discussion.

	XAFS xtal			XAFS film		
Bond	r(Å)	*n.b.*	σ(Å)	r(Å)	*n.b.*	σ(Å)
Cu(1)-O(4)	1.833(4)	1	i0.04(x)	1.861(2)	2	0.035(2)
Cu(1)-O(4)$_b$	1.941(4)	1	i0.01(x)	-	0	-
Cu(2)-O(4)	2.220(5)	1	0.04(x)	2.264(3)	2	0.059(2)
Cu(2)-O(4)$_b$	2.337(5)	1	i0.01(x)	-	0	-
Cu(2)-Y	3.182(7)	8	0.029(6)	3.191(8)	8	0.039(4)
Cu(2)-Cu(2)	3.349(8)	8	0.10(2)	3.358(8)	8	0.19(6)
Cu(2)-Ba	3.382(15)	8	0.024(8)	3.38(1)	8	0.037(8)
Cu(1)-Ba	3.475(8)	8	0.027(9)	3.472(4)	8	0.037(8)
Cu(2)-O(2,3)	3.65(2)	2	0.12(1)	3.656(3)	2	0.12(4)
Cu(1)-Cu(2)	4.102(5)	2	0.058(1)	4.106(4)	2	0.064(1)

	Neutron Diff.[45]				film
Bond	r(Å)	*n.b.*	σ_A(Å)	σ_B(Å)	ϕ
Cu(1)-O(4)	1.8588(13)	2	0.047(16)	0.064(9)	0.85(5)
Cu(1)-O(4)$_b$	-	0	-	-	-
Cu(2)-O(4)	2.2684(15)	2	0.037(14)	0.064(9)	0.6(1)
Cu(2)-O(4)$_b$	-	0	-	-	-
Cu(2)-Y	3.2041(5)	8	0.037(14)	0.034(16)	0.44(10)
Cu(2)-Cu(2)	3.386(1)	8	0.037(14)	0.037(14)	-3(2)
Cu(2)-Ba	3.367(1)	8	0.037(14)	0.046(16)	0.60(8)
Cu(1)-Ba	3.462(1)	8	0.047(16)	0.046(16)	0.55(11)
Cu(2)-O(2,3)	3.6583(5)	2	0.037(14)	0.056(17)	-2(3)
Cu(1)-Cu(2)	4.1272(1)	2	0.047(16)	0.037(14)	-0.03(10)

having significant overlap of its backscattering function with the Cu-Ba pairs.

Plots of σ vs. T are shown in Fig. 9.7. All the atom-pairs show an increase of σ with temperature, except the Cu(1)-O(4) and the Cu(2)-Cu(2) (not shown) atom pairs. The measurements of $\sigma_{Cu(2)-Cu(2)}$ are fairly large (~ 0.11 Å) with large estimated errors and are therefore unreliable. Only the Cu(1)-O(4) and the Cu(2)-O(4) pairs show any anomalies in σ near T_c. σ for both pairs increases slightly just above T_c and then returns just below T_c. The jump is larger for the Cu(2)-O(4) width (~0.008 Å) than for the Cu(1)-O(4) width (~ 0.004 Å). This behavior was noted for the Cu(1)-O(4) bond both by Stern *et al.*[84] and in Kimura *et al*[105], although the Stern result assumed a split O(4) site. None of the previous XAFS studies report a change in the Cu(2)-O(4) width.

All other atom-pair parameters show smooth behavior with temperature and are of reasonable values.

9.5.3 Correlations of the further neighbors

We have analyzed the correlations between positions of the Cu atoms and their near-neighbors by calculating ϕ for each atom pair. Diffraction measurements of broadening factors for each site are required, as indicated in Eq. 9.6. We have chosen temperature dependent neutron diffraction data given by Sharma *et al.*[45] because they include a relatively dense grid in temperature between data points ($\Delta T \cong$10 K), measurements over a similar range of temperatures (10-300 K) to this study, anisotropic thermal factors for the O(4) site, and a high sensitivity to the oxygen atoms. This diffraction study saw no anomalous features with temperature in the thermal factors for any lattice site and is consistent with a similar study by Kwei *et al*[106]. Since Sharma *et al.*'s measurements of the ther-

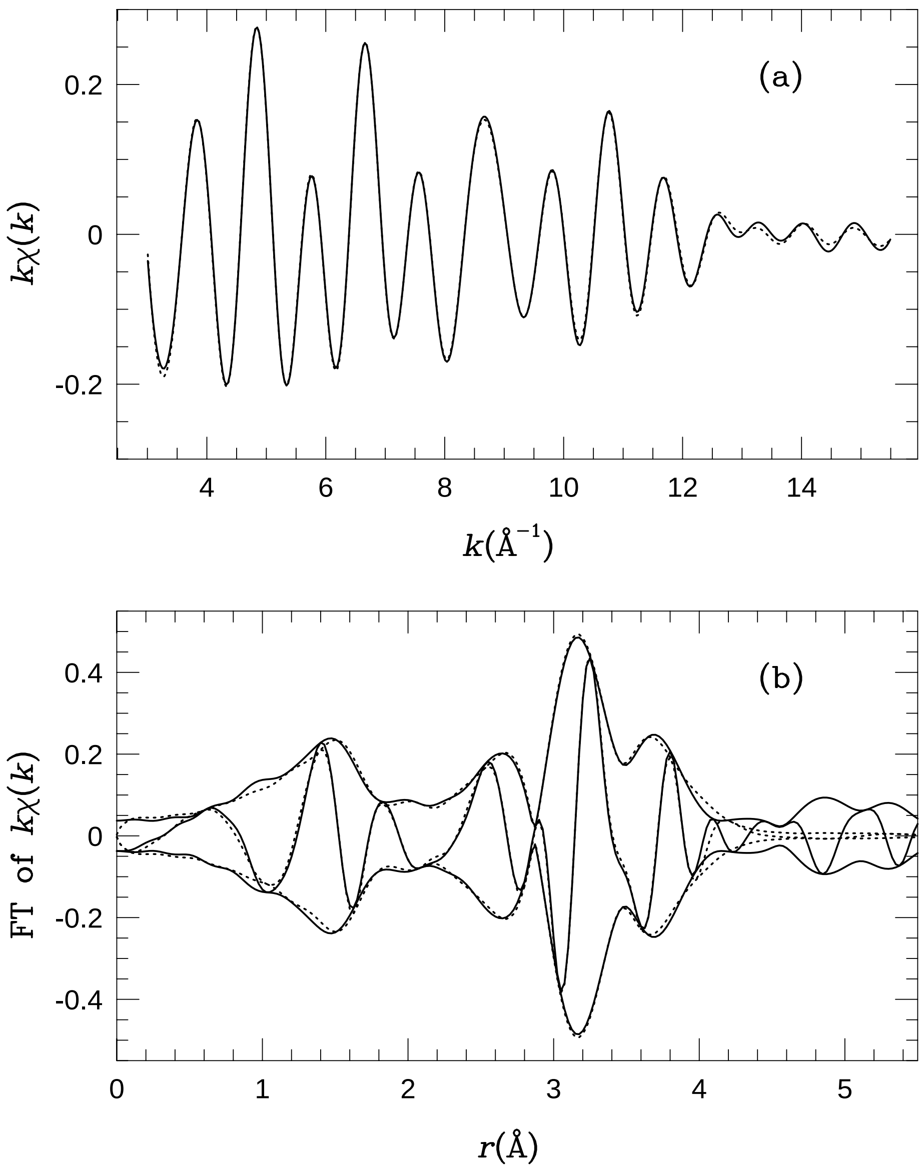

Figure 9.6: Full fit to (a) $k\chi(k)$ vs. k and (b) FT of $k\chi(k)$ vs. r for the YBCO film on MgO. Data in (a) are the back transform of the data in (b) from 1.3-4.0 Å in r-space. FT range in (b) is same as in Fig. 9.2. Notice that the quality of the fit is very good at low k and degraded somewhat at high k.

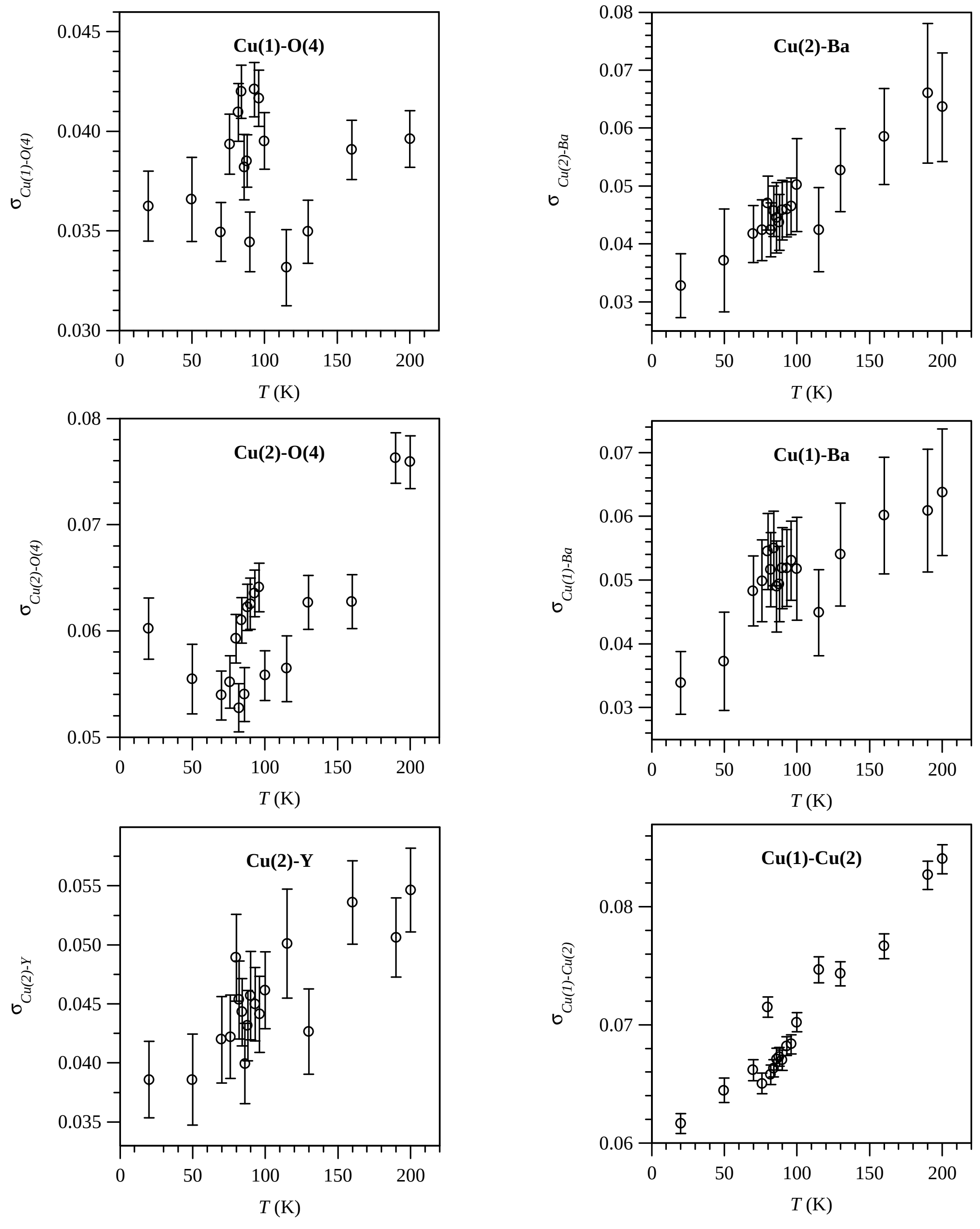

Figure 9.7: σ vs. temperature from the film of YBCO on MgO for all single scattering paths up to 4.15 Å, except the Cu(2)-Cu(2) (at $\sim$3.38 Å) and the Cu(2)-O(2,3) (at $\sim$3.66 Å) pairs. Errors are estimated from the covariance matrix, and in no way reflect any systematic errors, as discussed in Sec. 9.5.1. These errors should thus be taken as relative errors which indicate the reproducibility of the data.

mal factors were not always at the same temperatures as the measurements in this report, we fit each Debye-Waller factor from diffraction vs. temperature with a polynomial. The use of these thermal factors may introduce systematic errors into our measurements of ϕ not only because the samples are prepared with different methods in different laboratories, but also because the diffraction results were obtained from a powder of YBCO and our data is for a film. Unfortunately, we must tolerate such errors because no comprehensive, temperature-dependent study of a thin film of YBCO exists at this time. Such errors should only contribute to an overall shift of the ϕ parameter and should not greatly affect the temperature dependence unless major features in the (as yet, unmeasured) diffraction thermal factors occur in measurements on films and not on single crystals.

The correlation coefficients vs. temperature for each atom pair are displayed in Fig. 9.8. Errors are propagated from the quoted errors in Ref. [45] and the errors in Fig. 9.7 and in no way attempt to reflect any systematic errors introduced by FEFF6, differences in the samples, etc. The correlations for the Cu(2)-Cu(2) bond are not displayed because our measurements of $\sigma_{Cu(2)-Cu(2)}$ are unreliably large with large estimated errors. All the other atom-pairs are resolved in the fits well enough to give reasonable estimates of ϕ.

9.6 Discussion

9.6.1 Split O(4) site

The main result reported above is that while two O(4) sites are necessary to describe the XAFS data for a single crystal very well, a high-quality fit to XAFS data for the thin film with a single O(4) site is also possible. Although this result only puts an upper limit on the size of any site splitting at $\leq$0.09 Å, the measurements of the Debye-Waller

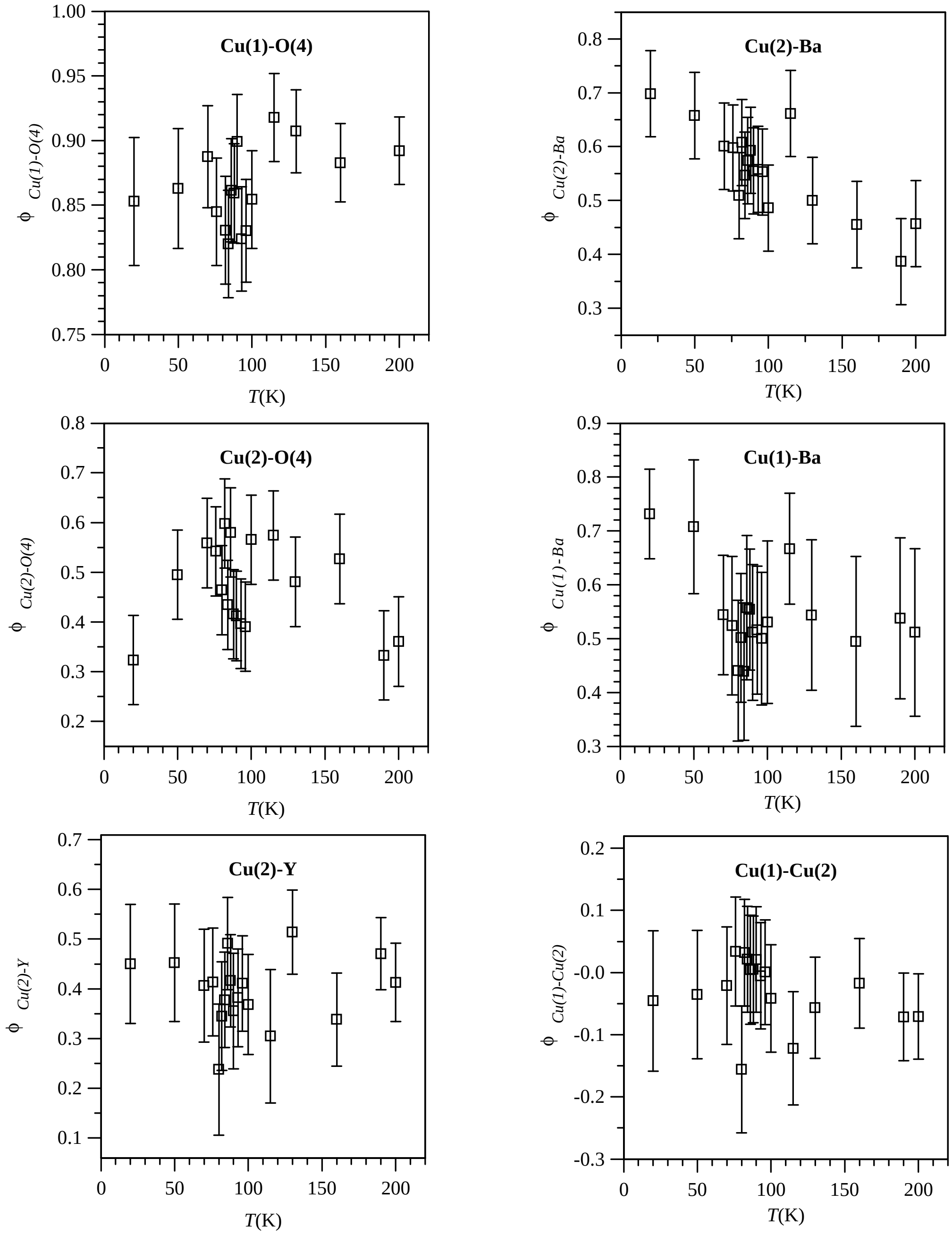

Figure 9.8: The correlation coefficient ϕ vs. temperature from the film of YBCO on MgO for the same atom pairs as in Fig. 9.7. Errors are propagated through Eq. 9.6 using the errors for the diffraction data reported in Ref. [45].

factors are small enough to indicate that any possible splitting is probably even smaller. (Any unresolved splitting should add to the thermal Debye-Waller factors in quadrature.)

Even though the existence of the splitting in some samples is now well established, the nature of the splitting is still quite unclear. The main problem is that the split sites could be due to motions of individual atoms between distinct sites, or due to two separate harmonic potentials, displaced from each other by, perhaps, a local distortion. One model[90] for static splitting relies on oxygen vacancy ordering on the O(1) site, which may shift the local position of the O(4) atom. At least one configuration of oxygen vacancies can produce a split O(4) position when half of the O(1) sites are occupied: the Ortho-II phase of $YBa_2Cu_3O_{6.5}$, which occurs when every other Cu-O(1) chain is completely vacant of oxygen. In this case, only half the O(4)'s have near O(1) neighbors. This configuration splits the O(4) site into two sites separated by ± 0.05 Å from the stoichiometric (no O(1) vacancies) site[91, 92]. Röhler[90] considers a similar situation when single O(1) vacancies cause shifts in the O(4) position both along the same chain and along neighboring chains. In this model a single O(1) vacancy affects 12 O(4) atoms. In the case of YBCO with $\delta = 6.95$ (as in our single crystal), this would mean 60% of the O(4) oxygens could be affected. This model can also explain why the effect seems to be more easily fit as a split O(4) distribution in lower T_c samples (i.e. more O(1) vacancies) as measured by Stern *et al*[84]. Any changes observed in the splitting near T_c would be considered a reordering of oxygen vacancies in this model. In order to explain the thin film results, one would have to consider that the oxygen concentration is similar in the film and the single crystal (Sec. 9.2). Instead, one might invoke the added stress on the material introduced by the substrate. This stress could perhaps be manifest as a freezing of the vacancies into a random organization that suppresses the amount of splitting. This hypothesis is not likely, however, because oxygen diffusion measurements are not drastically different in a film compared to crystals[107, 108]. Another possibility is that the films are overdoped and hence there are very few O(1) vacancies. Indeed, the films are overdoped with respect to T_c, however other factors may contribute to the actual number of oxygen vacancies, such as defects. A direct test of this argument would be to measure films that range from overdoped to very underdoped (i.e. many O(1) vacancies).

A dynamic model that would lead to either a broadening or a split O(4) position is the hopping small polaron model, with the polaron hopping on and off the Cu-O(4) bonds as discussed by Mustre de Leon *et al*[40]. Ranninger[88] has calculated the XAFS signatures for the presence of polarons and shown that as the hopping speed decreases, the pair distribution function first broadens and then splits; less than a factor of two in hopping speed is required to change from a broadened peak to a split peak. This is expected from the following simple argument. When the electron hops at a much faster rate than the lightest optical phonons, the lattice cannot respond, and there is little displacement of the individual atoms. If the hopping is slower, the lattice has time to respond, and the Cu and O(4) atoms move towards each other or apart as the polaron hops on and off the ligand. If the hopping rate falls below the optical frequency, a split Cu-O(4) distribution emerges, corresponding to the absence or presence of the polaron. This model can easily explain both the single crystal and the thin film results with a small change in the polaron hopping rate. The fact that the Cu(2)-O(4) peak is less ordered than the Cu(1)-O(4) peak and has a correlation parameter $\sim$0.5 is consistent with such a model.

Although the oxygen vacancy argument has possible merit, there is a body of literature that links dynamics of the O(4) site to anomalies in vibrational spectroscopies both in YBCO[85, 109, 110] and other materials[85, 109, 80, 111]. Since XAFS is not sensitive to static verses dynamic changes in atomic positions, there is little chance the XAFS technique can resolve this issue. However, XAFS can determine whether a pair-distribution function is harmonic or not. In our fits to the split distribution in the single crystal, we had to allow for a large fourth cumulant for both O(4) sites. This term can either have the effect of flattening out or sharpening the peak of an otherwise harmonic distribution, depending on the sign. These data required a positive 4th-cumulant, and were thus sharper than a harmonic distribution. No third cumulant was necessary to fit the data. The necessity of this extra parameter indicates that the pair-distribution function is not simply the sum of two harmonic distributions. The need for this quartic term is consistent with Raman measurements of the O(4) mode at 505 cm^{-1} which also requires a significant 4th-order term[85] . This anharmonicity has been speculated[85] to be related to the anharmonic potential implied by the split O(4)[40, 112]. The anharmonicity in the O(4) 505 cm^{-1} mode could now be directly linked to the split O(4) distribution if accurate measurements of the Raman anharmonicity can be shown to be significantly different between a film and a single crystal. This result would mean that the anharmonicity (and any polaron formation related to this anharmonicity) is not required for high-T_c superconductivity. On the other hand, if the anharmonicity in the 505 cm^{-1} peak is unchanged between the film and the crystal, then the split O(4) is not related to it. In this scenario, polaron formation may still exist and be important for high-T_c, but the split O(4) would not be the structural manifestation of it.

When trying to explain why splitting of the O(4) site may or may not be present, one should also consider the T_c dependence. Stern *et al.* reports that the changes in the splitting near T_c are more pronounced for the lower T_c samples. However, the two-site fits to the O(4) for the higher T_c samples in their work are not of the same high quality as for the lower T_c samples. In other words, the pair-distribution function for these samples appears to be more complicated than a simple two-site distribution, so the Stern fits cannot really rule out any significant temperature dependence. In any case, for some samples, they report a constant splitting at all temperatures. This result is in contrast to the work by Mustre de Leon *et al*, where they report the splitting to be constant at all temperatures, except near T_c where the splitting shrinks from 0.13 Å to < 0.11 Å. The results of our work on the single crystal also indicate that the temperature dependence may not be consistent from sample to sample: all the data at $T < T_c$ cannot be fit satisfactorily with a single O(4) site, yet the T=100 K data are well described with a single O(4) site.

9.6.2 Changes in broadening parameters

In our measurements of the broadening parameters of the film on MgO we observe some significant temperature dependencies. Almost all the measured bonds show the Debye-Waller factor increasing with temperature, as one expects if the Debye temperature is not too large (Fig. 9.7). The exception is the Cu(1)-O(4) bond which maintains a broadening of approximately 0.035-0.40 Å from T=20 to 200 K. The only significant behavior occurring near T_c involves the O(4) atom: both the Cu(1)-O(4) and the Cu(2)-O(4) pairs show an increase in their broadening parameter, with $\sigma_{Cu(1)-O(4)}$ jumping from 0.035 to 0.040 between 80 K and 100 K and back then to 0.035 Å, and $\sigma_{Cu(2)-O(4)}$ jumping from 0.060 Å to 0.068 Å between 80 K and 96 K and back to 0.060 Å. In the region between

T=80 K and 100 K, both $\sigma_{Cu(1)-O(4)}$ and $\sigma_{Cu(2)-O(4)}$ varies from temperature to temperature more than the estimated error. This fluctuation may be real or the error estimates may be too small for some reason, perhaps from inaccurate temperature measurements. However, the Cu(2)-O(4) data vary more smoothly. Stern *et al.* also measured a fluctuation in the Cu(1)-O(4) broadening near T_c, however their measurement assumed a two site distribution that had collapsed to one site in the same temperature range as the broadening fluctuation. Kimura *et al.*[105] measured a fluctuation in $\sigma_{Cu(1)-O(4)}$ in a similar temperature range using a single O(4) site fit, but reported no anomalies in $\sigma_{Cu(2)-O(4)}$ near T_c. No proven explanation of the physics behind these fluctuations exists, however, they can be interpreted in terms of changes in the correlation between the Cu and O atomic positions (see next section).

9.6.3 Correlations between atomic positions

Like the O(4)-site position, changes in ϕ with temperature can be attributed to changes in the static disorder of the individual sites, or to changes in the dynamics of the lattice displacements. As the temperature of the sample is decreased, static disorder could manifest itself as an ordering of oxygen vacancies, which would then generate a distinct set of positions for a given atom. If the site is split into two or three distinct positions, XAFS would measure an unusually broad peak for that pair and thus look like the atom-pair displacements are negatively correlated. It is therefore important to consider the absolute value of the broadening measurements from XAFS as compared to diffraction to try to help determine if the model used to fit the data is consistent, i.e. single atomic sites broadened harmonically around some average pair distance. Also, trends in the correlation with temperature should give some insight into which correlations within the unit cell are dependent on static or thermal disorder.

The most important result from the measurements of ϕ in Fig. 9.8 is that, within the estimated errors, they are all in the range from 0 to 1, indicating that the measurements of S_0^2, the calculated $F(k)$ and the model used to fit the data are all fairly accurate. More direct tests of the reliability of the absolute measurements of ϕ are provided by the nearest and the furthest bonds measured, that is, the Cu(1)-O(4) pairs and the Cu(1)-Cu(2) multiple scattering pair. Since the Cu(1)-O(4) pair is the nearest neighbor pair in YBCO, we expect at low temperatures that ϕ should be very near unity, and it is: $\phi_{Cu(1)-O(4)}$ demonstrates weak temperature dependence with a mean value of about 0.87, in approximate agreement with correlation measurements of the Hg-O(2) pair in Hg-1201[111]. The fluctuations near T_c are well within the increased errors after propagating the diffraction errors into ϕ.

The Cu(1)-Cu(2) atom pair is the furthest neighbor fit and includes multiple scattering off the intervening O(4) atom. It is therefore a good test of the FEFF multiple scattering calculations for $F(k)$[19] as well as the absolute reliability of ϕ. We expect this pair to be the least correlated, and it is; $\phi_{Cu(1)-Cu(2)}$ shows no obvious change with temperature (although both XAFS and diffraction broadening factors show a significant temperature dependence) and is consistent with $\phi_{Cu(1)-Cu(2)} \cong 0$. The absolute accuracy of this pair is worse than the other pairs measured because the FEFF calculation includes multiple scattering off the O(4). Consequently, this measurement is consistent with $\phi_{Cu(1)-Cu(2)} \cong \pm 0.2$. The Cu-Ba pairs show a strong temperature dependence in ϕ, in each case dropping from about ϕ=0.7 to 0.5 between 20 and 200 K. The Cu(2)-Y pair is partially correlated (~ 0.45

$\pm$ 0.1) and shows little temperature dependence between 20-200 K. Perhaps surprisingly, the correlation coefficient for the cold temperature Cu(2)-Y pair is lower than the Cu-Ba pairs, even though the barium has the freedom to move along the c-axis towards the chains without seriously distorting any bonds.

The most interesting correlation measurements are for the Cu(2)-O(4) pair. $\phi_{Cu(2)-O(4)}$ starts out very low ($\sim$0.4) but starts to *increase* to a maximum of $\sim$0.6 just below T_c. In the vicinity of T_c, ϕ then drops to about 0.45 and then increases again to its maximum value of 0.6. As the temperature is increased above 100 K, ϕ decreases steadily from 0.6 to 0.4. This decrease in ϕ (and hence the increase in σ mentioned in Sec. 9.6.2) may be the result of a negatively-correlated mode being excited near T_c relative to the correlated mode that is dominating away from T_c. Such a mode may be consistent with a polaronic-hopping transport mode[111].

9.7 Conclusions

We have contrasted XAFS measurements on a thin film of YBCO on MgO with measurements on a single crystal with 1.4% Ni. We have also compared the results with a film on $LaAlO_3$, which gives essentially the same results for the O(4) distribution, and with previous measurements on oriented powders. The single crystal data exhibit an anharmonic site distribution for the O(4) atom which can be described as a split position below T_c and a single position above T_c. (The temperature range measured for the single crystal is limited.) This result is consistent with previous results on oriented powders[12, 84].

The main result of this paper is that the thin film data show very different behavior. The O(4) peak can be well described by a single-site, harmonic distribution. This distribution does not show any strongly anharmonic behavior with temperature near T_c, or at any other temperature between 20-200 K.

These data refute the argument that the XAFS signal showing the split O(4) site distribution is too small to be measured reliably[84]; however, high S/N is required. The Fourier-filtered film data are very reproducible over the temperature range measured, and since only subtle changes occur in the O(4) site distribution for the film near T_c, the changes in the data with temperature are gradual and predominantly thermally driven. Because of this reproducibility, the rapidly changing XAFS from the single crystal must be taken as a legitimate signal, and not as noise.

Although we don't see any evidence of anharmonicity in the O(4) site in the film, fits show that the broadening factor for the Cu(2)-O(4) bond exhibits a local maximum above T_c followed by a drop below T_c to essentially its T=20 K value. The Cu(1)-O(4) pair demonstrates similar behavior, but the effect is smaller and is not as systematic with temperature. Since there is no such behavior in the published diffraction literature[45, 106] we have interpreted this as a change in the degree of correlation between the Cu(2) and the O(4) atoms, and possibly between the Cu(1) and the O(4) atoms. This result is in contrast to measurements by Kimura *et al.*[105] which show changes in the broadening factor for the Cu(1)-O(4) bond near T_c, but not in the Cu(2)-O(4) bond.

Finally, a better understanding of the local structure is obtained by considering the local correlations of the near-neighbors. As mentioned above, the Cu(1)-O(4) is measured to be a very tight bond, yet the Cu(2)-O(4) is "looser" and exhibits a decrease in the correlation between the atoms near T_c, indicating that the chains act as a unit that is somewhat independent of the planes. This lack of correlation is also indicated by the measurement of the correlation coefficient $\phi_{Cu(1)-Cu(2)}$ near zero (< 0.2) that also does not change with temperature. However, the atomic displacements in the metal-oxide layer do become less correlated at higher temperatures. The atomic positions in the CuO_2 planes apparently remain correlated in the temperature range measure based on the measurements on the Cu(2)-Y atom pair.

Chapter 10

Evidence of temperature-dependent polaron distortion in $\mathbf{La}_{1-x}A_x\mathbf{MnO}_3$, A=Ca, Pb

 The archival version of this work was published in C. H. Booth, F. Bridges, G. J. Snyder and T. H. Geballe, Phys. Rev. B **54**, *R13352 (1996).*

Although the basic physics behind the connection between the ferromagnetic (FM) transition, the conductivity and the "colossal" magnetoresistance (CMR) in materials such as $\mathrm{La}_{1-x}A_x\mathrm{MnO}_3$ (A= one of certain divalent metals) is described by the double-exchange mechanism of Zener[113], several features of the CMR materials are inconsistent with a model that only consists of double exchange[4]. Including spin-polarons and electron-electron interactions can help explain some features, such as the absolute value of T_c[114]. Including thermal spin fluctuations may account for the conductivity[115]. However, as pointed out by deGennes[116], calculations of the conductivity may be inaccurate unless they include lattice interactions. One possibility is that the charge-hopping in the double-exchange model induces structural-polaron formation[4, 117]. Such a formation would invalidate the assumption that the mean-free path is independent of the carrier mass, thereby enhancing the spin-spin coupling term in the double-exchange Hamiltonian[4]. If a polaron mechanism is to explain the discrepancies between the CMR effect with the double-exchange model, polarons must exist at least above T_c, and undergo a change in their dynamics below T_c with the result that the root-mean-square (rms) displacements of the atoms involved must be significantly reduced. Alternatively, if such changes are not observed, thermal spin fluctuations may be a better description.

Above T_c, the primary form of charge-transport will be hopping, while below T_c the system will be in a metallic phase. In the former case, a moving charge may carry a lattice distortion along with it (small polaron), while in the latter case the lattice will not have time to react or have a small distortion on a larger scale (large polaron).

Non-structural evidence for polaron formation above T_c is mounting[118, 119, 120]. Recent results include: activated behavior in the resistivity[118] and thermopower[119], and a large isotope shift of T_c with high O_{18} concentration[120].

There are also a growing number of structural experiments that have shown evidence for polaron distortions in these materials[3, 121, 122, 123, 124]. Neutron diffraction measurements on $La_{1-x}Ca_xMnO_3$ (x=0.12, 0.21, and 0.25) have shown Jahn-Teller distortions of the O(2) (planar) atoms, producing three Mn-O bond lengths in the planes separated by about 0.02 Å. Both the planar and axial (O(1)) oxygens have changes in the slope of the rms displacements with temperature at T_c in samples with metal-insulator (MI) transitions for the O(1), O(2) and La/Ca sites[3].

A more compelling measurement should be provided by an experiment than can act as a *local* probe, since measurements of magnetization do not depend on long-range order. Such probes give information about the correlations between atomic positions[121, 111]. A pair distribution function analysis (PDF) of the same data as the diffraction analysis described above shows an increase of 0.12 Å in the distribution width of the Mn-O and O-O pairs[121]. Interestingly, the width in temperature of the transition is much broader in the PDF analysis, suggesting that the effect is present on a local scale far away from T_c. Another neutron diffraction study claims to see an anomalously long Mn-O peak at ~2.28 Å, which shows no temperature dependence, on a sample of $La_{0.67}Sr_{0.33}MnO_3$. Previous x-ray-absorption fine-structure (XAFS) measurements are qualitatively similar with these studies, measuring a change in the shape of the Mn-O distribution across T_c[123], and a long Mn-O bond of ~2.5 Å[124].

This work reports our XAFS results for the Mn-O atom pair. The data show that the smooth and rapid change in the Debye-Waller broadening parameter σ^2 near T_c for this bond as seen in PDF experiments[121] on A=$Ca_{0.21}$ and $Ca_{0.25}$, is present in our XAFS experiments on A=$Ca_{0.25}$, $Ca_{0.33}$ and $Pb_{0.33}$. This change is shown to be inconsistent with broadening due to thermal phonons. We also measure σ^2 for the next two near-neighbors in the $Ca_{0.25}$ sample, and find the changes near T_c are smaller in the Mn-Ca/La scattering paths than in the Mn-O and the Mn-O-Mn paths, and therefore appear to mostly involve only the Mn and O atoms. Measurements of a sample which also has an antiferromagnetic transition but no metal-insulator transition (A=$Ca_{0.5}$) show no such effects, consistent with the insulating $Ca_{0.12}$ sample in the neutron scattering study.

Powder samples were made by the solid-state reaction of various proportions of the elemental oxides MnO, La_2O_3, and PbO and the carbonate $CaCO_3$. Further details can be found in Ref. [118]. Magnetization vs. T for the samples are shown in Fig. 10.1. T_c's (estimated from 1/2 saturation magnetization) are 236±5 K, 268±5 K, and 241±5 K for the A=$Ca_{0.25}$, $Ca_{0.33}$, and $Pb_{0.33}$ samples, respectively. The $Ca_{0.5}$ sample's T_c is 240±10 K; it also has a Néel temperature around 210 K.

All absorption measurements were made in the transmission mode at the Stanford Synchrotron Radiation Laboratory on beamline (BL) 2-3 with Si(220) monochromator crystals and BL 10-2 with Si(111) crystals. Samples were ground, run through a 30 μm sieve and brushed onto scotch tape. Four layers of such tape were stacked to provide samples with a Mn K-edge step of roughly 0.3. Samples were then placed in an Oxford helium-flow cryostat. Temperature was monitored via a sensor on the probe about 2-6 cm from the sample. The temperature was regulated within 0.1 K, but the sample temperature could be as much as 2 K higher than the nominal temperature, especially for the higher temperatures.

Data were reduced following standard procedures[15, 17, 16]. The XAFS were isolated by defining the parameter $\chi(k) = \mu(k)/\mu_0(k) - 1$, where k is the magnitude of the photoelectron wave vector, $\mu(k)$ is the total x-ray absorption due to the Mn K-shell excitation, and $\mu_0(k)$ is the part of $\mu(k)$ that does not include the interference of the

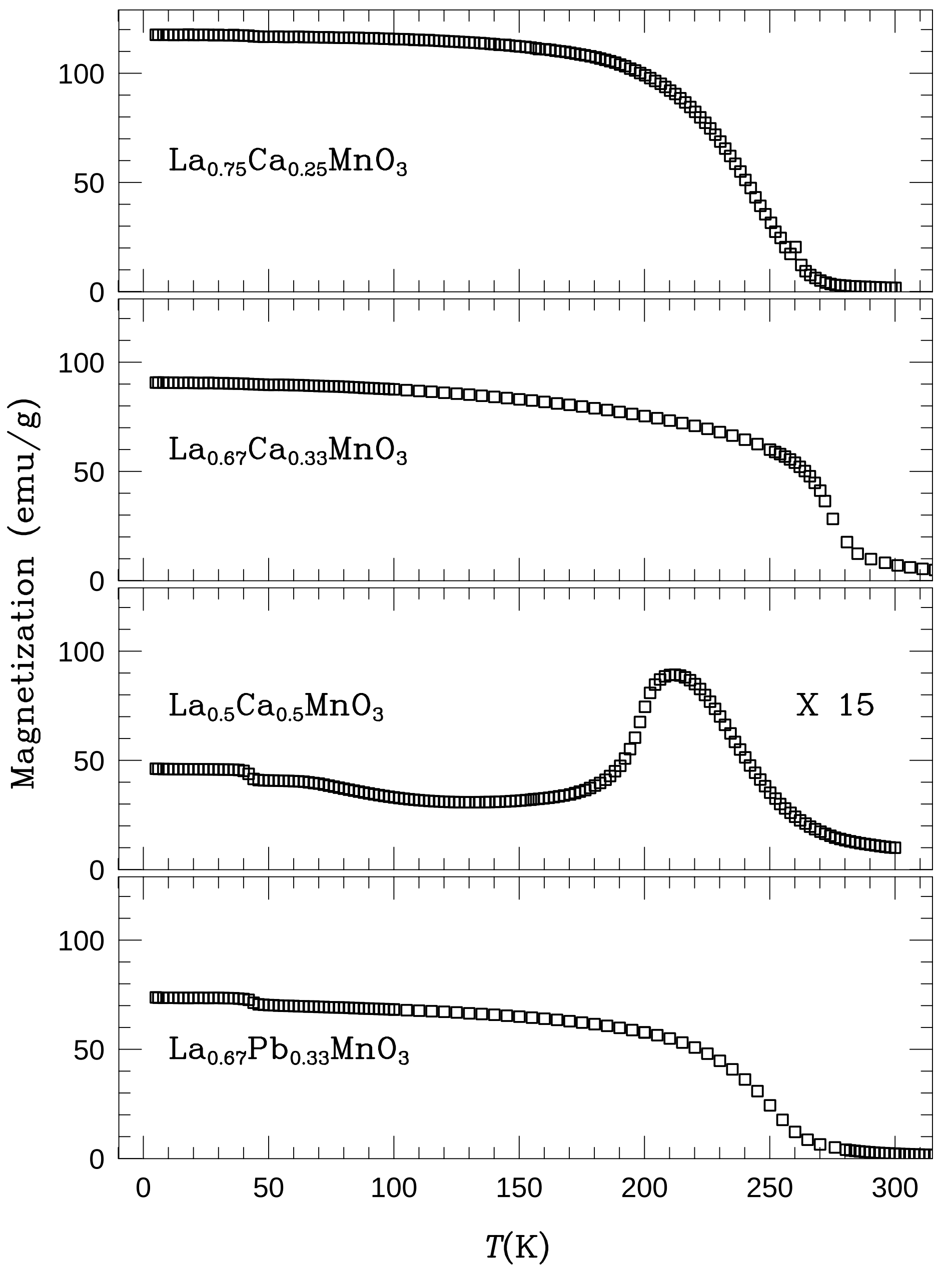

Figure 10.1: Magnetization vs. T for all samples. The applied fields were (from top to bottom) 2.5 kOe, 10 kOe, 2.5 kOe and 5 kOe. The magnetization data for the $Ca_{0.50}$ data has been multiplied by 15.

outgoing part of the photoelectron wave function and the backscattered part. Although the monochromator crystals were more than 50% detuned, measurements of $\chi(k)$ from BL 2-3 were slightly lower in amplitude (~3%) than the measurements from BL 10-2 at the same temperature, presumably from second-harmonic contamination. We therefore multiplied the data from BL 2-3 by 1.03 to allow better comparisons of the two data sets.

Fits to the data utilized theoretical standards as calculated by FEFF6[20]. Theoretical standards (as opposed to standards obtained experimentally) allow for the measurement of an absolute broadening factor in the pair-distribution function, and thus allow for a direct comparison to diffraction results.

Fig. 10.2 shows Fourier transforms (FT) of $k\chi(k)$ for each sample measured at 100 K and at 300 K. The first peak in these transforms is due to the Mn-O atom pair, while the broad peak centered near 3.2 Å is really a multipeak with contributions from Mn-A, Mn-La and the Mn-Mn pairs. The main feature to recognize in this figure is that the MI materials, all show a reduction in the Mn-O peak as T is raised from 100 K to 300 K. Such behavior may indicate a *soft* bond with a low Debye temperature, or possibly some other kind of change in the structural parameters. On the other hand, the Mn-O peak in the $La_{0.5}Ca_{0.5}MnO_3$ data is nearly unchanged (even near the FM transition), suggesting a relatively high Debye temperature and no other structural changes.

We fit each spectrum to standards of Mn-O, Mn-La, Mn-A, and the multiple scattering Mn-O-Mn path. These paths were calculated assuming the simple perovskite structure with no distortions. In particular, the Mn-O-Mn bond angle was taken to be 180°, even though for some compounds in the $LaMnO_3$ series, this angle can be as small as 160°. This angle is expected to be close to 180° for these materials[125]. The amplitude

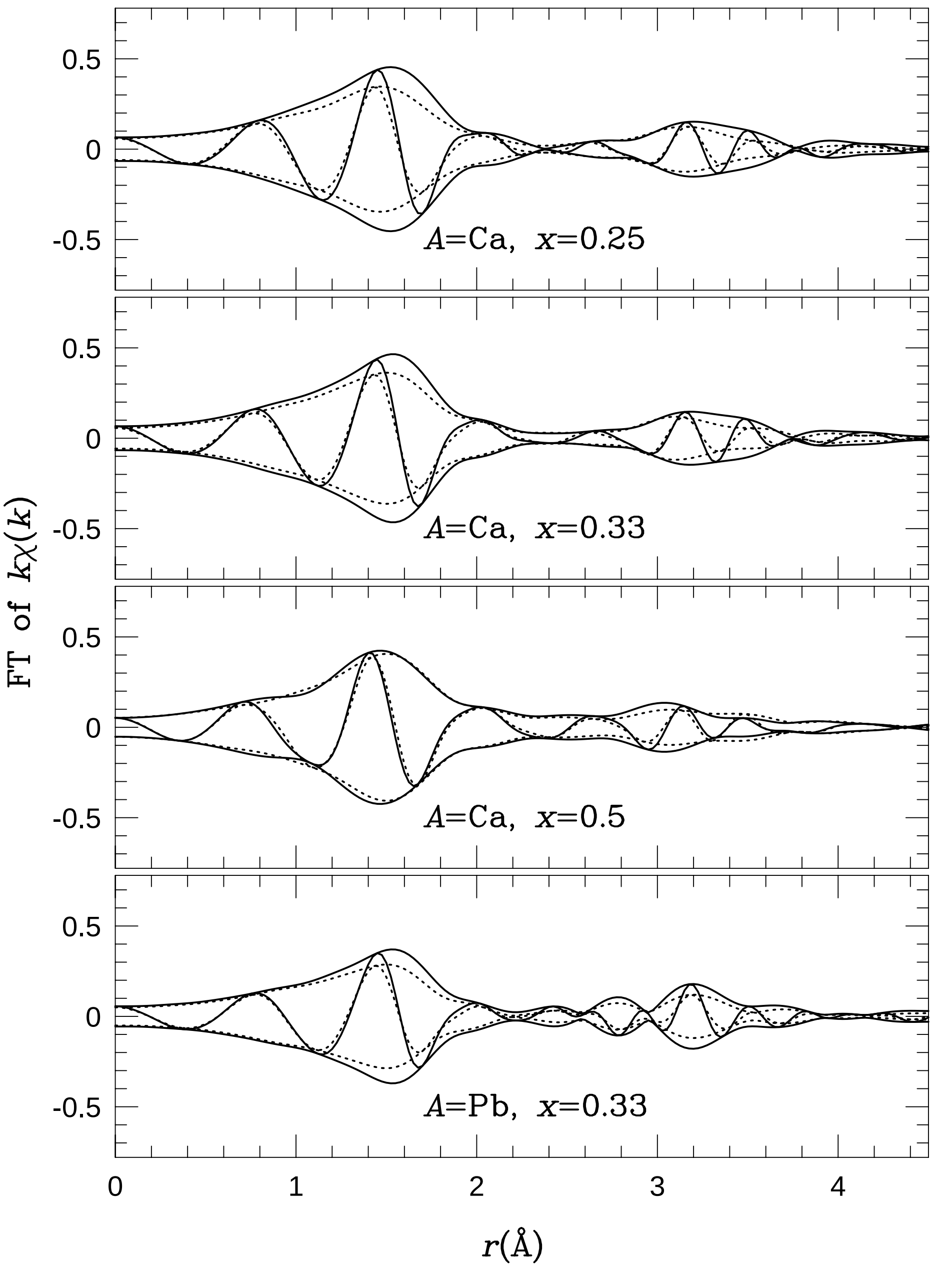

Figure 10.2: r-space data of each sample at (solid) T=100 K and (dotted) T=300 K. Data are transformed from 3.5-14.5 Å^{-1} and Gaussian broadening by 0.3 Å^{-1}.

reduction factor S_0^2 (an overall coefficient not accounted for by FEFF6) was based on the Mn-O peak for each sample and varied between 0.70 and 0.75, assuming 6 oxygens in the Mn-O peak. The Mn-O-Mn path was allowed to have its own S_0^2 of 0.55 to account for any possible change in the bond angle and for problems with FEFF6's multiple scattering calculations.

Fits to the Mn-O peak for the lowest temperature data are very similar for all samples. None of the bond lengths changed with temperature within the estimated error. The Mn-O bonds for the A=$Ca_{0.25}$, $Ca_{0.33}$, $Ca_{0.5}$, and $Pb_{0.33}$ are 1.95±0.005 Å, 1.95±0.005 Å, 1.92±0.005 Å and 1.96±0.005 Å, respectively. These results are consistent with diffraction studies[3, 125, 126]. Fits to the Mn-O broadening parameter for these data are presented in Fig. 10.3 and are consistent with the raw data in Fig. 10.2, as well as clearly showing a change in the local Mn-O environment. The σ^2 from the $La_{0.5}Ca_{0.5}MnO_3$ data is fit reasonably to a correlated-Debye model plus static disorder with $\Theta_D \cong 950$ K. Interestingly, none of the data from the MI materials fits a Debye model very well in any temperature range. Each one starts out at the lowest temperatures with a σ^2 lower than the 50% Ca material (note that the $Ca_{0.5}$ results are shifted in Fig. 10.3), suggesting a higher Debye temperature or less static disorder. However, as T is increased (but still below the Curie point) σ^2 increases too sharply to be consistent with such a high Θ_D. A lower Θ_D would be possible except that an unphysically negative amount of static disorder would be necessary to describe the data. Within ~40 K of T_c, σ^2 begins to climb even more sharply, leveling off about 40 K above T_c. This behavior is fundamentally different from the behavior expected for phonon broadening with either a Debye or Einstein model, including static disorder. For these models, the tangent line to the data always has a positive intercept. A straight line though the data in the transition region has a negative intercept.

Fits to the further neighbor Mn-La, Mn-Ca and Mn-O-Mn paths for the $La_{0.75}Ca_{0.25}MnO_3$ data are presented in Fig. 10.4. The relative intensity of the Mn-La and Mn-Ca signal could vary widely in the fits; interferences occur which make various combinations possible. Therefore, their intensities were held at a fixed 3:1 ratio, and their bond lengths were held equal in the fits. The Mn-Ca/La bond length was measured to be 3.38±0.02 Å and did not change with temperature. All bonds in Fig. 10.4 show similar increases of σ^2 near T_c. We obtain a rough measure of the size of the increase in σ^2 by extrapolating the low temperature fits to σ^2 past T_c and measuring the maximum difference between the data and this extrapolation. For the Mn-O bond in the 25% Ca sample, this increase is approximately 0.0022 Å^2, corresponding to an increase in σ of 0.047 Å through T_c. (Note that σ's add in quadrature.) If the disorder in the Mn-O pair is only along the a, b and c axes, its projection onto the Mn-Ca/La pair is $\sim \Delta\sigma^2 \times (\frac{r_{Mn-O}}{r_{Mn-La/Ca}})^2 \sim 0.0022 \times (\frac{1.93}{3.37})^2 = 0.0007$ Å^2 (ignoring any oxygen dimpling). The measured size of the anomaly for the Mn-La/Ca pair is, in fact, 0.0007 Å^2. This analysis suggests that either (a) only the Mn is distorting (unlikely, given that Mn is nearly 4 times heavier than oxygen, and there is no step in the Mn thermal parameters in Ref. [3]) or (b) the Ca does distort, but only a fraction of the amount that the oxygens distort. In either case, we conclude that the distortion involves mostly the Mn and O atoms. This conclusion is supported by the 0.0028 Å^2 jump for the Mn-O-Mn path. This path may have a larger step in σ^2 due to either a change in the correlation of the Mn positions or deviations of the bond angle from 180°; these data cannot differentiate between these two possibilities. La-edge data should help further determine the nature of this disorder.

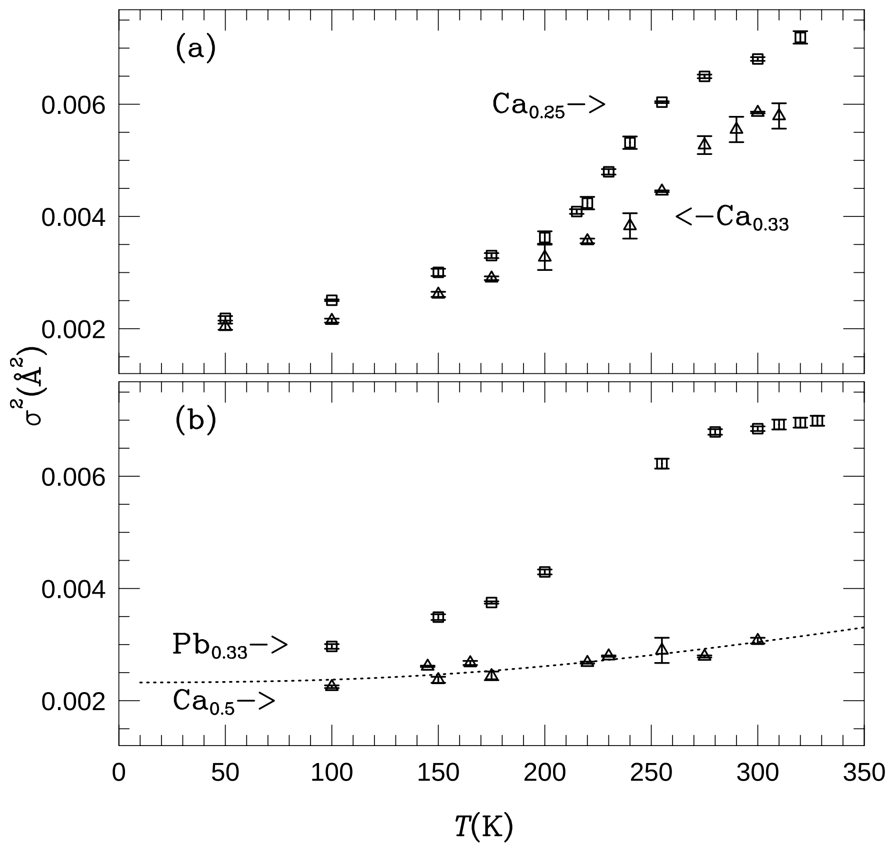

Figure 10.3: σ^2 vs. T for the Mn-O peak for all samples measured. The $Ca_{0.5}$ measurements are shifted down by 0.001 Å^2 for clarity. Error bars indicate reproducibility of the data and fit, and in no way attempt to estimate systematic errors, with may be as large as 20%. The dotted line shows a correlated-Debye model for Θ_D=950 K with 0.0011 Å^2 static broadening, also shifted down by 0.001 Å^2.

It is interesting to note the similarities between the magnetization data and the σ^2 fit results. Each distribution shows a long tail towards low temperature and approximately the same width in the transition region. Considering the magnetic data together with the high ($\sim$ 1000 K) Debye temperature necessary to describe the XAFS at the lowest temperatures, we are lead to the conclusion that virtually *all* the temperature dependence demonstrated by the MI materials is magnetic in origin and caused by the degree of localization of polarons. At low temperatures and high magnetizations, the conduction electrons

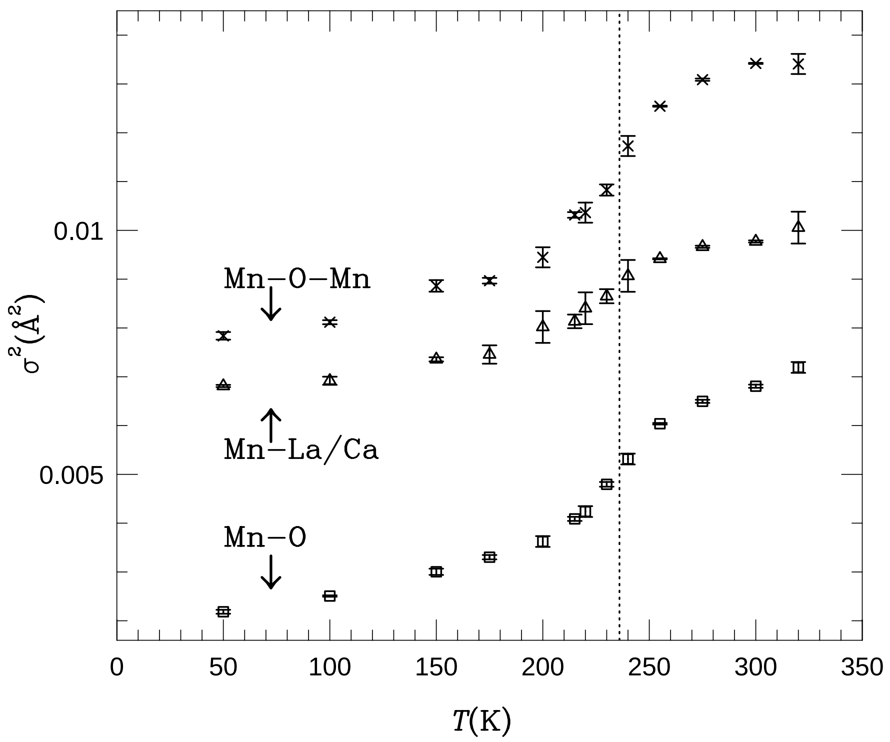

Figure 10.4: σ^2 vs. T for the $La_{0.75}Ca_{0.25}MnO_3$ Mn-O, Mn-La/Ca and Mn-O-Mn scattering paths. The vertical dotted line marks T_c.

are allowed to hop freely between spin-aligned ions, and thus the polarons are effectively delocalized. Contrary to the usual thermal activation of polaron hopping, as T is increased towards T_c and the magnetization decreases, the polarons encounter more and more resistance in the form of unaligned ion-spins and are thus more likely to become trapped, causing more localization and distortion. This trend will eventually reverse as T increases[118].

Qualitatively, this distortion is consistent with Millis' prediction that the polaron distortion should cause an increase in the width of the distribution of the oxygen atoms near T_c of order 0.1 Å[4] .

These data and this analysis are not consistent with a previous XAFS study[123]. In that study, Tyson *et al* measured a drastic change in the shape of the XAFS spectrum between T=80 K and 273 K, which they interpreted as a change in the Mn-O bond length distribution. As is clear from Fig. 10.2, we do not measure a fundamental difference between T=100 and 300 K (or anywhere in between), although there is an obvious difference in the amount of disorder. In another study, Tyson *et al* measure a long Mn-O pair at ~2.5 Å[124], which is roughly in agreement with Louca *et al*[122]. We do see some evidence for such a peak, however there are several other interpretations, including an analysis artifact arising from FEFF6, and therefore do not include it in this analysis. Including this extra peak does not affect the results of this paper.

In conclusion, this work demonstrates a clear step-like increase in the width of the Mn-O bond near T_c for samples with a MI transition and a temperature dependence below T_c that is related to the magnetization of the sample. Since diffraction measurements do not show any step in the width parameters of any sites (they do show a change in slope at T_c)[3], the steps we have measured in this work can be interpreted as arising from a more negatively-correlated character in the positions of the atoms in the Mn-O and Mn-Mn pairs. In addition, we have shown that most of these displacements only involve the Mn and O atoms, as one expects from a polaron distortion. Lastly, we should point out that since diffraction measures essentially the same distortions above and below T_c, consistent with Jahn-Teller band-splitting, the measurements reported in this work are separate and distinct from a change in the Jahn-Teller distortions.

Appendix A

publication list

REGULAR PAPERS:

[1] C. H. Booth, F. Bridges, G. Snyder, and T. B. Geballe. Structural evidence of temperature-dependent polaron formation above Tc from local structure around Mn atoms in $La_{1-x}A_xMnO_3$, A=Ca, Pb. Phys. Rev. B (Rapid Comm.), 54:R15606 (1996).

[2] C. H. Booth, F. Bridges, J. Boyce, T. Claeson, B. M. Lairson, R. Liang, and D. A. Bonn. Comparison of local structure measurements from c-axis polarized XAFS between a film and a single crystal of $\mathrm{YBa_2Cu_3O_{7-\delta}}$ as a function of temperature. Phys. Rev. B, 54:9542 (1996).

[3] C. H. Booth, F. Bridges, E. D. Bauer, G. G. Li, J. B. Boyce, T. Claeson, C. H. Chu, and Q. Xiong. XAFS measurements of negatively correlated atomic displacements in $\mathrm{HgBa_2CuO_{4+\delta}}$. Phys. Rev. B (Rapid Comm.), 52:R15745, 1995.

[4] C. H. Booth, F. Bridges, J. B. Boyce, T. Claeson, Z. X. Zhao, and P. Cervantes. Local disorder in the oxygen environment around praseodymium in $\mathrm{Y_{1-x}Pr_xBa_2Cu_3O_7}$. Phys. Rev. B, 49:3432, 1994.

[5] G. H. Kwei, C. H. Booth, F. Bridges, and M. A. Subramanian. Single valence and structural disorder in the CMR pyrochlore $Tl_2Mn_2O_7$. Phys. Rev. B (Rapid Comm.), in press.

[6] E. D. Bauer, F. Bridges, C. H. Booth, J. B. Boyce, T. Claeson, G. Brorsson and Y. Suzuki, Phys. Rev. B, 54:13352 (1996).

[7] G. J. Snyder, C. H. Booth, F. Bridges, R. Hiskes, S. DiCarolis, M. R. Beasley and T. H. Geballe. Local structure, transport and rare earth magnetism in the ferrimagnetic perovskite $Gd_{0.66}Ca_{0.33}MnO_3$. Phys. Rev. B, in press.

[8] G. G. Li, F. Bridges, and C. H. Booth. XAFS standards: a comparison of experiments and theory. Phys. Rev. B, 52:6332, 1995.

[9] J. J. Rehr, C. H. Booth, F. Bridges, and S. I. Zabinsky. X-ray-absorption fine-structure in embedded atoms. Phys. Rev. B (Rapid Comm.), 49:12347, 1994.

[10] C.-H. Park, B. O. Wells, DiCarlo, Z. X. Shen, J. R. Salem, Bethune, C. S. Yannoni, R. D. Johnson, M. S. de Vries, C. H. Booth, F. Bridges, and P. Pianetta. Structural determination on Y ions in C_{82} from EXAFS experiments. Chem. Phys. Lett., 213:196, 1993.

[11] A. Buffington, C. H. Booth, and H. S. Hudson. Using image area to control CCD systematic errors in spaceborne photometric and astrometric time-series measurements. Pub. Astr. Soc. Pac., 665:685, 1991.

[12] A. Buffington, H. S. Hudson, and C. H. Booth. A laboratory measurement of CCD photometric and dimensional stability. Pub. Astr. Soc. Pac., 652:688, 1990.

CONFERENCE PAPERS:

[13] C. H. Booth, F. Bridges, Z. Kvitky, L. Romano, F. Ponce. Environment about Indium

in $Ga_{1-x}In_xN$ from In and Ga K-edge XAFS. Physica B (Proc. from XAFS IX), in press.

[14] F. Bridges, C. H. Booth, G. G. Li, E. D. Bauer, J. B. Boyce and T. Claeson. Does the local structure play a role in high temperature superconductivity? Superlattices and Microstructures, 19:313 (1996).

[15] F. Bridges, G. G. Li, and C. H. Booth. Large local distortions introduced by defects in $YBa_2Cu_3O_7$ superconductor: an x-ray absorption study. Radiation Effects and Defects in Solids, 137:351 (1995).

[16] F. Bridges, C. H. Booth, and G. G. Li. An iterative approach to atomic background removal in XAFS data analysis. Physica B (Proc. from XAFS XIII), 208&209:121, 1995.

[17] C. H. Booth, F. Bridges, J. B. Boyce, T. Claeson, Z. X. Zhao, and P. Cervantes. Local disorder in the oxygen environment around praseodymium in $Y_{1-x}Pr_xBa_2Cu_3O_7$. Mat. Res. Soc. Symp. Proc., 307:117 (1993).

Bibliography

[1] J. G. Bednorz and K. A. Müller, Z. Phys. B **64**, 189 (1986).

[2] S. Jin, M. McCormack, T. H. Tiefel, R. M. Fleming, J. Phillips, and R. Ramesh, Science **264**, 413 (1994).

[3] G. H. Kwei, S. J. L. Billinge, J. J. Neumeier, A. C. Lawson, D. N. Argyriou, and J. D. Thompson (unpublished).

[4] A. J. Millis, P. B. Littlewood, and B. L. Shraiman, Phys. Rev. Let. **74**, 5144 (1995).

[5] R. Fehrenbacher and T. M. Rice, Phys. Rev. Lett. **70**, 3471 (1993).

[6] P. M. Horn, D. T. Keane, G. A. Held, J. L. Jordan-Sweet, D. L. Kaiser, F. Holtzberg, and T. M. Rice, Phys. Rev. Lett. **59**, 2772 (1987).

[7] C. Meingast, O. Kraut, T. Wold, H. Wühl, A. Erb, and G. Müller-Vogt, Phys. Rev. Lett. **67**, 1634 (1991).

[8] R. P. Sharma, L. E. Rehn, P. M. Baldo, and J. Z. Liu, Phys. Rev. Lett. **62**, 2869 (1989).

[9] L. Gao, Y. Y. Xue, F. Chen, Q. Xiong, R. L. Meng, D. Ramirez, C. W. Chu, J. H. Eggert, and H. K. Mao, Phys. Rev. B **50**, 4260 (1994).

[10] N. L. Saini *et al.*, Physica C **268**, 121 (1996).

[11] G. G. Li, F. Bridges, J. B. Boyce, T. Claeson, C. Ström, S.-G. Eriksson, and S. D. Conradson, Phys. Rev. B **51**, 8564 (1995).

[12] J. Mustre de Leon, S. D. Conradson, I. Batistic, and A. R. Bishop, Phys. Rev. Lett. **65**, 1675 (1990).

[13] T. Egami, Ferroelectrics **130**, 15 (1992).

[14] B. K. Teo, *EXAFS: Basic Principles and Data Analysis* (Springer-Verlag, New York, 1986).

[15] T. M. Hayes and J. B. Boyce, in *Solid State Physics*, edited by H. Ehrenreich, F. Seitz, and D. Turnbull (Academic, New York, 1982), Vol. 37, p. 173.

[16] F. Bridges, C. H. Booth, and G. G. Li, Physica B **208&209**, 121 (1995).

[17] G. G. Li, F. Bridges, and C. H. Booth, Phys. Rev. B **52**, 6332 (1995).

[18] G. G. Li, Ph.D. thesis, Univ. of California, Santa Cruz, 1994.

[19] J. J. Rehr, R. C. Albers, and S. I. Zabinsky, Phys. Rev. Lett. **69**, 3397 (1992).

[20] S. I. Zabinsky, A. Ankudinov, J. J. Rehr, and R. C. Albers, Phys. Rev. B **52**, 2995 (1995).

[21] S. I. Zabinsky, Multiple scattering theory of XAFS, Univ. of Washington, 1993.

[22] E. A. Stern and K. Kim, Phys. Rev. B **23**, 3781 (1981).

[23] J. J. C. Mikkelsen and J. B. Boyce, Phys. Rev. B **28**, 7130 (1983).

[24] E. A. Stern and Y. Yacoby, J. Phys. Chem. of Solids **57**, 1149 (1986).

[25] B. Holland, J. B. Pendry, R. S. Pettifer, and J. Bordas, J. Phys. C **11**, 633 (1978).

[26] J. J. Rehr, J. Appl. Phys. **32**, 8 (1993).

[27] G. G. Li, F. Bridges, and G. S. Brown, Phys. Rev. Lett. **68**, 1609 (1992).

[28] M. Newville, Y. Y. P.Livins, J. J. Rehr, and E. A. Stern, Phys. Rev. B **47**, 14126 (1993).

[29] A. I. Frenkel, E. A. Stern, M. Qian, and M. Newville, Phys. Rev. B **48**, 12449 (1993).

[30] J. J. Rehr, J. Mustre de Leon, S. I. Zabinsky, and R. C. Albers, J. Am. Chem. Soc. **113**, 5135 (1991).

[31] J. J. Rehr, R. C. Albers, and S. I. Zabinsky, Phys. Rev. Lett. **69**, 3397 (1992).

[32] C. H. Booth, F. Bridges, J. B. Boyce, T. Claeson, Z. X. Zhao, and P. Cervantes, Phys. Rev. B **49**, 3432 (1994).

[33] J. J. Rehr and R. C. Albers, Phys. Rev. B **41**, 8139 (1990).

[34] R. G. Newton, *Scattering Theory of Waves and Particles*, 2nd ed. (Springer-Verlag, New York, 1982).

[35] P. A. Lee and J. B. Pendry, Phys. Rev. B **11**, 2795 (1975).

[36] J. Goulon, C. Goulon-Ginet, R. Cortes, and J. M. Dubois, J. Physique **43**, 539 (1982).

[37] L. Tröger, D. Arvanitis, K. Baberschke, H. Michaelis, U. Grimm, and E. Zschech, Phys. Rev. B **46**, 3283 (1992).

[38] G. G. Li, F. Bridges, and X. Wang, Nucl. Instr. and Meth. **A340**, 420 (1994).

[39] P. G. Allen, J. Mustre de Leon, S. D. Conradson, and A. R. Bishop, Phys. Rev. B **44**, 9480 (1991).

[40] J. Mustre de Leon, S. D. Conradson, I. Batistic, A. R. Bishop, I. D. Raistrick, M. C. Aronson, and F. H. Garzon, Phys. Rev. B **45**, 2447 (1992).

[41] S. L. Cooper, M. V. Klein, B. G. Pazol, J. P. Rice, and D. M. Ginsberg, Phys. Rev. B **39**, 5920 (1988).

[42] R. S. Liu, C. Thomsen, W. Kress, M. Cardona, B. Gegenheimer, F. W. de Wette, J. Prade, A. D. Kulkarni, and V. Schroder, Phys. Rev. B **37**, 7971 (1988).

[43] D. J. Bishop, A. P. Ramirez, P. L. Gammel, B. Batlogg, E. A. Rietman, R. J. Cava, and A. J. Millis, Phys. Rev. B **36**, 2408 (1987).

[44] X. D. Schi, R. C. Yu, Z. Z. Wang, N. P. Ong, and P. M. Chaikan, Phys. Rev. B **39**, 827 (1989).

[45] R. P. Sharma, F. J. Rorella, J. D. Jorgensen, and L. E. Rehn, Physica C **174**, 409 (1991).

[46] P. H. Hor, R. L. Meng, Y. Q. Wang, L. Gao, Z. J. Huang, J. Bechtold, J. Foster, and C. W. Chu, Phys. Rev. Lett. **58**, 1891 (1987).

[47] S. E. Brown, J. D. Thompson, J. O. Willis, R. M. Aiken, E. Zirgniebl, J. L. Smith, Z. Fisk, and R. B. Scwarz, Phys. Rev. B **36**, 2298 (1987).

[48] L. Schneemeyer, J. V. Wasczak, S. M. Zahurak, R. B. V. Dover, and T. Siegrist, Mater. Res. Bull. **22**, 1467 (1987).

[49] D. W. Murphy, S. Sunshine, R. B. V. Dover, R. J. Cava, B. Batlogg, S. M. Zahurak, and L. F. Schneemeyer, Phys. Rev. Lett. **58**, 1888 (1987).

[50] L. Soderholm, K. Zhang, D. G. Hinks, M. A. Beno, J. D. Jorgensen, C. U. Segre, and I. K. Schuller, Nature **328**, 604 (1987).

[51] J. Boyce, F. Bridges, T. Claeson, R. S. Howland, and T. H. Geballe, Phys. Rev. B **36**, 5251 (1987).

[52] Y. Dalichaouch, M. S. Torikachvili, E. A. Early, B. W. Lee, C. L. Seaman, K. N. Yang, H. Zhou, and M. B. Maple, Solid State Comm. **65**, 1001 (1988).

[53] A. Kebede, C. S. Jee, J. Schwegler, J. E. Crow, T. Mihalisin, G. H. Myer, R. E. Salomon, P. Schottmann, M. V. Kuric, S. H. Bloom, and R. P. Guertin, Phys. Rev. B **40**, 4453 (1989).

[54] M. Bickel, G. L. Goodman, L. Soderholm, and B. Kanellakopulos, J. Solid State Chem **76**, 178 (1988).

[55] L. Soderholm, C. K. Loong, G. Goodman, and B. Dabrowski, Phys. Rev. B **43**, 7923 (1991).

[56] H. D. Jostarndt, U. Walter, J. Harnischmacher, J. Kalenborn, A. Severing, and E. Holland-Moritz, Phys. Rev. B **46**, 14872 (1992).

[57] E. E. Alp, G. K. Shenoy, L. Soderholm, G. L. Goodman, D. G. Hinks, and B. W. Veal, Mat. Res. Soc. Symp. Proc. **99**, 177 (1988).

[58] S. Horn, J. Cai, S. A. Shaheen, Y. Jeon, M. Croft, C. L. Chang, and M. L. denBoer, Phys. Rev. B **36**, 3895 (1987).

[59] F. W. Lytle, G. van der Laan, R. B. Greegor, E. M. Larson, C. E. Violet, and J. Wong, Phys. Rev. B **41**, 8955 (1990).

[60] N. Neukirch, C. T. Simmons, P. Sladeczek, C. Laubschat, O. Strebel, G. Kaindl, and D. D. Sarma, Europhysics Lett. **5**, 567 (1988).

[61] J. Fink, N. Ncker, H. Romberg, M. Alexander, M. B. Maple, J. J. Neumeier, and J. W. Allen, Phys. Rev. B **42**, 4823 (1990).

[62] Y. X. Jia, J. Z. Liu, A. Matsushita, M. D. Lan, P. Klavins, and R. N. Shelton, Phys. Rev. B **46**, 11745 (1992).

[63] J. S. Kang, J. W. Allen, B. W. Lee, M. B. Maple, Z. X. Shen, J. J. Yehu, W. P. Ellis, W. E. Spice, and I. Linda, in *High Temperature Superconductivity, Electronic Structure*, edited by A. Bianconi and A. Marcelli (Pergamon, Oxford, 1989), p. 225.

[64] G. Cao, J. W. O'Reilly, J. E. Crow, J. Boliva, D. Nichols, and S. T. Ting, Bull. Am. Phys. Soc. **38**, 782 (1993).

[65] M. E. López-Morales, D. Ríos-Jara, J. Tagüeña, R. Escudero, S. La Placa, A. Bezinge, V. Y. Lee, E. M. Engler, and P. M. Grant, Phys. Rev. B **41**, 6655 (1990).

[66] J. J. Neumeier, T. Bjørnholm, M. B. Maple, J. J. Rhyne, and J. A. Gotas, Physica C **166**, 191 (1990).

[67] C. K. Lowe-Ma and T. A. Vanderah, Physica C **201**, 233 (1992).

[68] M. Guillaume, P. Allenspech, J. Mesot, B. Roessli, U. Staub, P. Fischer, and A. Furrer, Z. Phys. B **90**, 13 (1993).

[69] R. W. Wyckoff, *Crystal Structures* (John Wiley & Sons, New York, 1963).

[70] C. H. Booth, F. Bridges, P. Cervantes, J. Boyce, and T. Claeson, Mat. Rec. Soc. Symp. Proc. **307**, 117 (1993).

[71] W. J. Zhu, P. Liu, and Z. X. Zhao, Physica C **199**, 285 (1992).

[72] J. Mustre de Leon, J. J. Rehr, and S. I. Zabinsky, Phys. Rev. B **44**, 4146 (1991).

[73] S. L. Lin, E. A. Stern, A. J. Kalb, and Y. Zhang, Biochem. **30**, 2323 (1991).

[74] M. Beno, L. Soderholm, D. C. II, D. Hinks, J. Jorgensen, J. Grace, I. Schuller, C. Segre, and K. Zhang, Appl. Phys. Lett. **51**, 57 (1987).

[75] S. N. Putilin, E. Antipov, O. Chmaissem, and M. Marezio, Nature **362**, 226 (1993).

[76] B. H. Toby, T. Egami, J. D. Jorgensen, and M. A. Subramanian, Phys. Rev. Lett. **64**, 2414 (1990).

[77] Q. Huang, J. W. Lynn, Q. Xiong, and C. W. Chu, Phys. Rev. B **52**, 462 (1995).

[78] O. Chmaissem, Q. Huang, S. N. Putilin, M. Marezio, and A. Santoro, Physica C **212**, 259 (1993).

[79] J. L. Wagner, P. G. Radaelli, D. G. Hinks, J. D. Jorgensen, J. F. Mitchel, B. Dabrowski, G. S. Knapp, and M. A. Beno, Physica C **210**, 447 (1993).

[80] H.-G. Lee, H.-S. Shin, I.-S. Yang, J.-J. Yu, and N. H. Hur, Physica C **233**, 35 (1994).

[81] I.-S. Yang, H.-S. Shin, H.-G. Lee, S.-J. Jeon, H.-S. Ahn, J.-J. Yu, S. Lee, S.-I. Lee, and H. H. Hur, Phys. Rev. B **51**, 644 (1995).

[82] R. P. Sharma, L. E. Rehn, P. M. Baldo, and J. Z. Liu, Phys. Rev. B **40**, 11396 (1989).

[83] H. You, U. Welp, and Y. Fang, Phys. Rev. B **43**, 3660 (1991).

[84] E. A. Stern, M. Qian, Y. Yacoby, S. M. Heald, and H. Maeda, Physica C **209**, 331 (1993).

[85] D. Mihailovic, K. F. McCarty, and D. S. Ginley, Phys. Rev. B **47**, 8910 (1993).

[86] D. Emin, in *Condensed Matter Physics: The Theodore D. Holstein Symposium*, edited by R. L. Orback (Springer-Verlag, New York, 1986), pp. 16–34.

[87] D. Emin, in *Lattice Effects in High-T_c Supercontuctors*, edited by Y. Bar-Yam, T. Egami, J. Mustre-de Leon, and A. R. Bishop (World Scientific, New Jersey, 1992), pp. 377–388.

[88] J. Ranninger and U. Thibblin, Phys. Rev. B. **45**, 7730 (1992).

[89] J. R. Hardy, J. W. Flocken, and R. A. Guenther, in *Lattice Effects in High-T_c Superconductors*, edited by Y. Bar-Yam, T. Egami, J. Mustre-de Leon, and A. R. Bishop (World Scientific, New Jersey, 1992).

[90] J. Röhler, in *Materials and Crystallographic Aspects of High-T_c Superconductivity, Proceedings of the 20th course of the International School of Crystallography*, edited by E. Kaldis (Kluwer Academic Publishers, Boston, 1994).

[91] T. Zeiske, R. S. D. Hohlwein, , N. H. Anderson, and T. Wolf, Nature **353**, 542 (1991).

[92] T. Zeiske, D. Hohlwein, R. Sonntag, F. Kubanek, and G. Collin, Z. Phys. B **86**, 11 (1992).

[93] P. Bordet, C. Chaillout, T. Fournier, M. Marezio, E. Kaldis, J. Kaldis, J. Karpinski, and E. Jilek, Phys. Rev. B **47**, 3465 (1993).

[94] B. M. Lairson, Ph.D. thesis, Stanford University, 1991.

[95] C. B. Eom, J. Z. Sun, B. M. Lairson, S. K. Streiffer, A. F. Marshal, K. Yamamoto, S. M. Anlage, J. C. Bravman, and T. H. Geballe, Physica C **171**, 354 (1990).

[96] F. Bridges, J. B. Boyce, T. Claeson, T. H. Geballe, and J. M. Tarascon, Phys. Rev. B **42**, 2137 (1990).

[97] P. Schleger, W. N. Hardy, and B. X. Yang, Physica C **176**, 261 (1991).

[98] R. Liang, P. Dosanjh, D. A. Bonn, D. J. Baar, J. F. Caolan, and W. N. Hardy, Physica C **195**, 51 (1992).

[99] F. Bridges, G. G. Li, and X. Wang, Nucl. Inst & Meth. in Phys. **A320**, 548 (1992).

[100] E. D. Crozier, N. Alberding, K. R. Bauchspiess, A. J. Seary, and S. Gygax, Phys. Rev. B **36**, 8288 (1987).

[101] J. Boyce, F. Bridges, T. Claeson, and M. Nygren, Phys. Rev. B **39**, 6555 (1989).

[102] E. A. Stern, Phys. Rev. B **48**, 9825 (1993).

[103] P. Eisenberger and G. S. Brown, Solid State Comm. **29**, 418 (1979).

[104] W. H. Press, B. P. Flannery, S. A. Teukolsky, and W. T. Vetterling, in *Numerical Recipes: The Art of Scientific Computing*, 1 ed. (Cambridge University Press, New York, 1986), pp. 457,458.

[105] H. Kimura, H. Oyanagi, T. Terashima, H. Yamaguchi, Y. Bando, and J. Mizuki, Japanese J. of Appl. Phys. **32-2**, 584 (1993).

[106] G. H. Kwei, A. C. Larson, W. L. Hults, and J. L. Smith, Physica C **169**, 217 (1990).

[107] S.-G. Lee, S. C. Bae, J. K. Ku, and H. J. Shin, Phys. Rev B **46**, 9142 (1992).

[108] B. Pashmakov, K. Zhang, H. M. Jaeger, P. Tiwari, and X. D. Wu, Physica C **249**, 289 (1995).

[109] D. Mihailovic, C. M. Foster, K. F. Voss, T. Mertelj, I. Poberaj, and N. Herron, Phys. Rev. B **44**, 237 (1991).

[110] J. H. Nickel, D. E. Morris, and J. W. Ager, Phys. Rev. Lett. **70**, 81 (1993).

[111] C. H. Booth, F. Bridges, E. D. Bauer, G. G. Li, J. B. Boyce, T. Claeson, C. H. Chu, and Q. Xiong, Phys. Rev. B **52**, R15745 (1995).

[112] J. Mustre de Leon, I. Batistic, A. R. Bishop, S. D. Conradson, and I. D. Raistrick, Phys. Rev. B **47**, 12322 (1993).

[113] C. Zener, Phys. Rev. **82**, 403 (1951).

[114] C. M. Varma (unpublished).

[115] N. Furukawa, J. Phys. Soc. Jpn. **64**, 2734 (1995).

[116] P. G. de Gennes, Phys. Rev. **118**, 141 (1960).

[117] A. J. Millis, B. I. Shraiman, and R. Mueller, Phys. Rev. Lett. **77**, 175 (1996).

[118] G. J. Snyder, R. Hiskes, S. DiCarolis, M. R. Beasley, and T. H. Geballe, Phys. Rev. B **53**, 14434 (1996).

[119] M. Jaime, M. B. Salamon, M. Rubinstein, R. E. Treece, J. S. Horwitz, and D. B. Chrisey (unpublished).

[120] G. Zhao, K. Conder, H. Keller, and K. A. Müller, Nature **381**, 676 (1996).

[121] S. J. L. Billinge, R. G. DiFrancesco, G. H. Kwei, J. J. Neumeier, and J. D. Thompson, Phys. Rev. Lett. **77**, 715 (1996).

[122] D. Louca, W. Dmowski, T. Egami, E. L. Brosha, H. Röder, and A. R. Bishop (unpublished).

[123] T. A. Tyson, J. Mustre de Leon, S. D. Conradson, A. R. Bishop, J. J. Neumeier, and J. Zhang, Phys. Rev. B **53**, 13985 (1996).

[124] T. A. Tyson *et al.*, Phys. Rev. B , in press.

[125] R. Mahendiran, S. K. Tiwary, A. K. Raychaudhuri, T. V. Ramakrishnan, R. Mahesh, N. Rangavittal, and C. N. R. Rao, Phys. Rev. B **53**, 3348 (1996).

[126] P. G. Radaelli, D. E. Cox, M. Marezio, S.-W. Cheong, P. E. Schiffer, and A. P. Ramirez, Phys. Rev. Lett. **75**, 4488 (1995).